Search for resonant τ-sneutrino production in the $e\,\tau$ final state with the CMS detector

von

Stefan Bruch

Diplomarbeit in Physik

vorgelegt der

Fakultät für Mathematik, Informatik und Naturwissenschaften
der Rheinisch-Westfälischen Technischen Hochschule Aachen

im März 2013

angefertigt im

III. Physikalischen Institut A
Prof. Dr. Thomas Hebbeker

Zusammenfassung

Es wird eine Suche nach dem leichtesten supersymmetrischem Teilchen (LSP) in einem R-Paritäts verletzendem (RPV) SUSY Szenario präsentiert. In der Rolle des LSP wird das τ-sneutrino $\tilde{\nu}_\tau$ angenommen. Dies könnte resonant in Proton-Proton Kollisionen über die Kopplung λ'_{311} im Prozess $d\bar{d} \to \tilde{\nu}_\tau$ erzeugt werden und anschließend mit einer schmalen Zerfallsbreite über die Kopplung λ_{313} in einen $e\tau$ Endzustand zerfallen. Die Analyse umfasst die Rekonstruktion des hadronisch zerfallenden τ aus den Zerfallsprodukten, datengestützte Hintergrundskalierung und Ereigniszahlbestimmung.

Die Suche wird in $1.3\,\mathrm{fb}^{-1}$ Daten aus pp Kollisionen durchgeführt, die 2012 mit dem CMS Experiment bei $\sqrt{s} = 8\,\mathrm{TeV}$ aufgezeichnet wurden. Es ist kein Überschuss an Ereignissen über der Standardmodell-Vorhersage zu beobachten. Es wird eine Massenuntergrenze von (1.20 ± 0.15) TeV bestimmt, die mit dem aktuellen Limit von 1.2 TeV vereinbar ist.

Abstract

Presented is a search for the lightest supersymmetric particle (LSP) in a R-parity violating (RPV) SUSY scenario. The role of the LSP is considered to be played by the τ-sneutrino $\tilde{\nu}_\tau$. This may be produced resonantly in proton-proton collisions via the coupling λ'_{311} in the process $d\bar{d} \to \tilde{\nu}_\tau$, followed by a decay in a narrow width to an $e\tau$ final state via the coupling λ_{313}. The analysis covers reconstruction of the hadronic τ from decay products, data driven background scaling and event yield estimation.

The search is performed on $1.3\,\mathrm{fb}^{-1}$ data from pp collisions collected 2012 with the CMS experiment at $\sqrt{s} = 8\,\mathrm{TeV}$. No excess above the background prediction is observed. A lower mass limit of (1.20 ± 0.15) TeV is determined, which is in accordance with the current limit of 1.2 TeV.

Contents

1 Introduction

The preoccupation with particle physics is intimately connected with man's pursuit of gaining best possible knowledge of the fundamental principals of nature. It's dealing with the structure of matter and the interactions affecting it. The *Standard Model of Particle Physics* (SM) is the result of a long time of mutual interplay between observation of natural phenomena, modelling them with the formalism of mathematics and testing the reproducibility of the model's predictions in experiments. It summarises today's comprehension of the microcosmic world in terms of a *Quantum Field Theory* (QFT).

It is an everyday experience that apparently massive matter can be continuously split into smaller parts. Ancient greek philosophers around Leucippus and Democritus were one of the first who formulated a doctrine that this splitting can't be continued infinitely but will lead to a set of "*átomos*" ("indivisible") constituents which differ in shape and size and form basic modules for all macroscopic bodies [1].

A first scientific approach in this meaning was done by John Dalton, who discovered that in chemical reactions the relation of masses remains constant. As an explanation he supposed every element to be made up of uniform "last particles" that can be rearranged to new elements [2].

Different experiments enhanced the atomic model. A selection of some milestone discoveries outline this development [3]: Atoms have a substructure containing protons and electrons (Thomson 1897). These form spatially separated *nuclei* and *electron shells* (Rutherford 1911). Electrons are allowed to move on particular orbits only (Bohr 1914) what implies the occurrence of discrete energy levels and moves finally on to Quantum Mechanics (Schrödinger 1926). The discovery of wave-particle dualism (Einstein 1905, de Broglie 1924) and special relativity (Einstein 1905) dissolved the differences between matter, radiation and the interaction between them.

Finally, a particle can't be regarded as corpuscle furthermore but as a spontaneous concretisation of an abstract field in space-time. Any particle is fully represented by its invariant mass and a discrete collection of parameters denoted *quantum numbers*.

Subsequently hundreds of new particles have been found in nuclear decays, cosmic rays and accelerator experiments and formed a vast "particle zoo".

Looking at nature's structure at any scales, one can find symmetries everywhere. So, it seems natural to regard *symmetry* as a fundamental principle of reality. Thus, applying principles of *symmetry relations* allowed the diversity of the particle zoo to be understood as combinations of only a couple of fundamental constituents and interactions and allowed to formulate the coherent *Standard Model*.

Although the Standard Model is the interim end of a long development and can describe all known phenomena of the microscopic world, it leaves some inconvenient issues which cherish the suspicion that the description of the world is incomplete yet. Those are namely the missing of the final unification of forces as one would expect to exist

in respect to previous findings (*electromagnetism* and later *electroweak* unification) or the necessity of *fine tuning* the natural constants whereas balances in nature seem to be rather insensitive to small variations in most other observed cases, to mention just two.

So there is a lot of motivation to deal with theories beyond the Standard Model. A famous representative is *Supersymmetry* (SUSY). It introduces a partner to any SM-field and the corresponding particles respectively. This leads to a vanishing of many inconsistencies left by the SM.

The quest for SUSY is performed by searches for the particles it predicts. As these particles are assumed to have very high masses, their discovery was not within the reach of previous experiments. With the high centre-of-mass energy of the *Large Hadron Collider* (LHC) and the large amount of luminosity recorded by the *Compact Muon Solenoid* (CMS) detector, the door to new physics may have been opened now.

A search for a particular particle, the tau-sneutrino ($\tilde{\nu}_\tau$) as member of the R-parity violating (RPV) variant of SUSY within a simplified framework is treated in this thesis.

2 The Standard Model of Particle Physics

The *Standard Model* summarises today's knowledge of elementary particles and the interactions between them. This chapter introduces it's constituents, interactions and the theoretical framework describing them using the formalism of a *Quantum Field Theory* (QFT).

2.1 The Particle Content

The standard model consists of particles of two major categories distinguished by their spin property. Particles with spin 1/2 form the family of *fermions*. Within this family, particles with integral charge (0 or ± 1) are called *leptons*. Those with fractional charge are denoted *quarks*. Each of these subcategories contain six constituents that can be grouped into three doublets named *generations*. Generations show similar physical behaviour but are different in mass. Any particle has a complementary antiparticle with identical mass and spin but opposite charge-like quantum numbers. As massive particles tend to decay to lighter ones, the long-living condensed matter forming the macroscopic world is built-up by 1st-generation particles only.

The leptons are the negative charged electron (e), muon (μ) and tauon (τ) with a corresponding neutral neutrino (ν) each. Quarks are given by the "up-like" flavours *up* (u), *charm* (c) and *top* (t) with charge of 2/3 accompanied by their "down-like" partners *down* (d), *strange* (s) and *bottom* (b) with a charge of $-1/3$. Due to *confinemnet*, a characteristic of the strong interaction between quarks, those can't exist isolated but form boundary states called *hadrons* [4]. Combinations of two quarks like the pion $\pi^- = (\bar{u}d)$ are called *mesons* whereas threesomes like the proton $p = (uud)$ form the *baryons*.

Integral spin *bosons* form the second category. The gauge bosons (spin 1) are interpreted as mediator of interactions where the photon (γ) is the carrier of the electromagnetic force, whereas the gluon (g) is associated to the strong- and the $W^{\pm}$ and Z to the weak force. The Higgs (H) (spin 0) is assumed to be an excitation of the *higgs field* [5]. Table 2.1 illustrates the standard model particle content. The H is the last member of the SM which is not yet established experimentally without last doubts. In summer 2012 a boson-like particle with a mass of 125 GeV[1] was found which is fully compatible with the H-properties [7, 8]. Although the identity of this boson is not resolved finally, signs that the H has been discovered are strong enough that it is regarded to be found within this thesis.

[1] If not stated otherwise, all data within this thesis is given in *natural units* applying $\hbar = c = 1$

Generation	I	II	III
Quarks	$\begin{pmatrix} \mathbf{u}\,^{2/3}_{2.4\text{ MeV}} \\ \mathbf{d}\,^{-1/3}_{4.8\text{ MeV}} \end{pmatrix}$	$\begin{pmatrix} \mathbf{c}\,^{2/3}_{1.27\text{ GeV}} \\ \mathbf{s}\,^{-1/3}_{104\text{ MeV}} \end{pmatrix}$	$\begin{pmatrix} \mathbf{t}\,^{2/3}_{171.2\text{ GeV}} \\ \mathbf{b}\,^{-1/3}_{4.2\text{ GeV}} \end{pmatrix}$
Leptons	$\begin{pmatrix} \boldsymbol{\nu_e}\,^{0}_{2.2\text{ eV}} \\ \boldsymbol{e}\,^{-1}_{0.511\text{ MeV}} \end{pmatrix}$	$\begin{pmatrix} \boldsymbol{\nu_\mu}\,^{0}_{0.17\text{ MeV}} \\ \boldsymbol{\mu}\,^{-1}_{105.7\text{ MeV}} \end{pmatrix}$	$\begin{pmatrix} \boldsymbol{\nu_\tau}\,^{0}_{15.5\text{ MeV}} \\ \boldsymbol{\tau}\,^{-1}_{1.777\text{ GeV}} \end{pmatrix}$
Bosons	$\left(\boldsymbol{\gamma}\,^{0}_{0} \quad \boldsymbol{g}\,^{0}_{0} \quad \boldsymbol{W}\,^{\pm1}_{80.4\text{ GeV}} \quad \boldsymbol{Z}\,^{0}_{91.2\text{ GeV}} \quad \boldsymbol{H}\,^{0}_{\approx125\text{ GeV}}\right)$		

Table 2.1: Fundamental particles included in the standard model. Notation is n^c_m, where n denotes the particle name, c the charge and m the mass. Neutrino masses are upper limits. All properties are taken from [6].

2.2 The formalism of Quantum Field Theory

In general, the dynamic of a system with kinetic energy T embedded in a potential V can be captured in a quantity called *Lagrangian*

$$L = T - V \tag{2.1}$$

where T and V depend clasically on spatial coordinates q_i and their timely rate of change $\dot{q}_i$. In *field theory* the coordinates $q_i(t)$ are replaced by fields in space-time $\phi(\vec{x}, t)$ and the classical derivation $\partial_t q$ transforms to $\partial_\mu = \partial/\partial x^\mu$, where μ stands for the component index of a four-momentum. Thus, the Lagrangian L has to be replaced by the continuous *Lagrange density* $\mathcal{L}(\phi, \partial_\mu \phi)$ fulfilling the relation

$$L = \int \mathcal{L}\, d^3x. \tag{2.2}$$

Variational calculus lead to the *Euler-Lagrange* equations of motion for fields ϕ [9]:

$$\partial_\mu \left(\frac{\partial \mathcal{L}}{\partial \left(\partial_\mu \phi\right)} \right) - \frac{\partial \mathcal{L}}{\partial \phi} = 0. \tag{2.3}$$

To construct a quantum field theory for a certain phenomenology, a Lagrange density $\mathcal{L}$ has to be formulated, so that it's Euler-Lagrange equations (2.3) reproduce all equations of motion known from classical approaches.

Additionally, fields may be required to stay invariant for local points in space-time under application of certain *symmetry transformations*. This has to be regarded by including a suitable *gauge field* in the Lagrange density leading to the category of *gauge theories* which is used to describe the Standard Model.

2.3 Quantum Electro Dynamics

Quantum Electro Dynamics (QED) is a gauge theory describing electromagnetic fields and electrically charged particles (*i.e.* fermions) [10].

The electromagnetic field is described by the homogeneous Maxwell Equations

$$\vec{E} = -\nabla\Phi - \partial_t \vec{A}, \qquad \vec{B} = \nabla \times \vec{A} \tag{2.4}$$

where Φ stands for a scalar and $\vec{A}$ for a vector potential. Introducing the *electromagnetic field tensor*

$$F^{\mu\nu} = \partial_\mu A^\nu - \partial_\nu A^\mu \quad \text{with} \quad A^\mu = \left(\Phi, \vec{A}\right) \tag{2.5}$$

a Lagrangian leading to equations (2.4) is given by:

$$\mathcal{L}_{\text{boson}} = -\frac{1}{4} F_{\mu\nu} F^{\mu\nu}. \tag{2.6}$$

Fermions are described by complex four-component spinors ψ and their adjoints $\bar{\psi} = \psi^\dagger \gamma_0$ obeying the *Dirac Equations*

$$(i\gamma^\mu \partial_\mu - m)\,\psi = 0 \quad \text{and} \quad (i\partial_\mu \gamma_\mu + m)\,\bar{\psi} = 0 \tag{2.7}$$

where γ^μ denote the Dirac matrices. A Lagrangian reproducing equations (2.7) is

$$\mathcal{L}_{\text{dirac}} = \bar{\psi}\,(i\gamma^\mu \partial_\mu - m)\,\psi. \tag{2.8}$$

This $\mathcal{L}$ satisfies a global $U(1)$ symmetry, as it is not changed by a variation of the phase factor:

$$\psi(x) \to \psi'(x) = e^{i\alpha}\psi(x), \quad \alpha = \text{const.} \tag{2.9}$$

Demanding this symmetry to be also *local*, the constant phase factor α is replaced by a space-time dependent factor $\alpha(x)$. In this case, the symmetry is only achieved by replacing the partial derivatives ∂_μ in (2.8) by the *covariant derivation*

$$D_\mu = \partial_\mu + ieqA_\mu \tag{2.10}$$

with charge q that is coupled with strength e to a gauge field A_μ with the gauge transformation

$$A_\mu(x) \to A'_\mu(x) = A_\mu(x) + \frac{1}{eq}\partial_\mu \alpha(x), \tag{2.11}$$

where it is obvious to choose A_μ to be the same as in the field tensor (2.5). This leads to the gauge invariant fermionic Lagrangian

$$\mathcal{L}_{\text{fermion}} = \bar{\psi}\,(i\gamma^\mu D_\mu - m)\,\psi \tag{2.12}$$

and finally to the QED Lagrangian

$$\begin{aligned} \mathcal{L}_{\text{QED}} &= \mathcal{L}_{\text{fermion}} + \mathcal{L}_{\text{boson}} \\ &= \bar{\psi}\,(i\gamma^\mu D_\mu - m)\,\psi - \frac{1}{4} F_{\mu\nu} F^{\mu\nu} \end{aligned} \tag{2.13}$$

Within this, the D_μ from eqn. (2.10) couples the bosonic field A_μ to the fermions ψ with charge q using a coupling constant e. A_μ is interpreted as *photon field* whose quanta γ are mediators of the electromagnetic force acting between charged fermions whereas e is identified to be the elementary charge.

2.4 Quantum Chromo Dynamics

Quantum Chromodynamics (QCD) is the gauge theory describing the *strong force* between quarks mediated by gluons [11]. It has been developed by taking over the techniques that have been successfully used to formulate QED.

Different experiments [4, 12] show, that quark fields, in difference to leptons, have an additional degree of freedom with dimension three. This is captured in a new quantum number *colour* with possible values *red* (r), *green* (g) and *blue* (b) or their antivalue ($\bar{r}, \bar{g}, \bar{b}$) respectively. Colour is the conserved charge-like property strong interaction couples to. Therefore the applicable local gauge group of QCD is $SU(3)_c$. The Lagrangian $\mathcal{L}$ is constructed similarly as in QED. The result is:

$$\mathcal{L}_{\mathrm{QCD}} = \bar{\psi}\left(i\gamma_\mu D^\mu - m\right)\psi - \frac{1}{4}G^a_{\mu\nu}G^{\mu\nu}_a \tag{2.14}$$

with ψ denoting a six-tuple of quark flavours, a matrix $m = \mathrm{diag}(m_u..m_t)$ and the field strength tensor

$$G^a_{\mu\nu} = \partial_\mu G^a_\nu - \partial_\nu G^a_\mu - g_s \epsilon^a_{bc} G^b_\mu G^c_\mu. \tag{2.15}$$

The tensor (2.15) contains an additional, nonlinear third component compared to the electromagnetic one (2.5), which implies a self-coupling of gluons among each other. As a consequence, gluons can breed by vacuum polarisation what affects the potential for two quarks q in distance r. With exceeding a maximum r, new $q\bar{q}$ pairs are created and form boundary states with the original quarks appearing as hadrons. This inability to separate quarks is called *confinement*.

2.5 Quantum Flavour Dynamics

Quantum Flavour Dynamics (QFD) is the gauge theory of *weak interaction* [10]. It affects all fermions and the H. In contrast to QED and QCD this theory has some phenomenological characteristics. First, the weak vector bosons $W^\pm$ and Z^0 are massive, what is inconsistent with gauge theory and has to be explained with the *Higgs mechanism* (see section 2.6). Second, QFD distinguishes between the *chirality* of the fermion fields. Chirality can be < 0 ("left-handed") or > 0 ("right-handed"). In the ultrarelativistic limit, it describes the spin's projection on the momentum $\vec{p}$. Chiral fermion states are created by the *chirality operator*:

$$\psi_L(x) = \frac{1}{2}\left(1 - \gamma^5\right)\psi(x), \qquad \psi_R(x) = \frac{1}{2}\left(1 + \gamma^5\right)\psi(x) \tag{2.16}$$

Fermions are grouped into left-handed doublets and right-handed singlets like

$$\begin{pmatrix}\nu_e \\ e^-\end{pmatrix}_L, \quad \begin{pmatrix}u \\ d'\end{pmatrix}_L, \quad (e^-)_R, \quad (u)_R \tag{2.17}$$

for the 1st generation constituents. Other generations apply respectively.

Within the quark doublets there is a differentiation between *mass eigenstates* (u) known from QCD and *weak eigenstates* (d') related to QFD. Latter are linear combina-

tions of u-like quarks. This *mixing* is described by the 3×3 *CKM-Matrix* (V_{CKM}):

$$\begin{pmatrix} d' \\ s' \\ b' \end{pmatrix} = V \begin{pmatrix} d \\ s \\ b \end{pmatrix} \tag{2.18}$$

where the components $|V_{ij}|^2$ are the transition probabilities between two flavours $i \leftrightarrow j$ by exchange of a $W^{\pm}$ (*charged current (CC)*). Within each generation, a CC lepton flavour transition is also possible.

All fermions are assigned a charge-like quantum property, the *weak isospin* T with $T_L = 1/2$ and $T_R = 0$ with a component $T_3 = +1/2$ for up- and $T_3 = -1/2$ for downlike particles. Additionally, the *weak hypercharge* Y, defined as

$$Y = 2(Q - T_3), \tag{2.19}$$

including the electric charge Q, is introduced. Isospin T_L and hypercharge Y are conserved quantities in QFD whose corresponding symmetry groups form the gauge group

$$SU(2)_W \otimes U(1)_Y. \tag{2.20}$$

Generators of $SU(2)_W$ are the three Pauli matrices σ^i. The corresponding gauge fields are W^i_μ. The $U(1)$ gauge field is B_μ. Using coupling constants g and g', the covariant derivatives

$$\begin{aligned} D_\mu \psi_L &= \left(\partial_\mu + i\frac{g}{2}\sigma^j W^j_\mu + ig' Y B_\mu \right) \psi_L \\ D_\mu \psi_R &= \left(\partial_\mu + ig' Y B_\mu \right) \psi_R \end{aligned} \tag{2.21}$$

lead to the Lagrangian

$$\begin{aligned} \mathcal{L}_{\text{QFD}} &= \sum_{\text{flavours}} \bar{\psi}_f i\gamma^\mu D_\mu \psi_f - \frac{1}{4} W^j_{\mu\nu} W^{\mu\nu}_j - \frac{1}{4} B_{\mu\nu} B^{\mu\nu} \\ \text{with} \quad W^j_{\mu\nu} &= \partial_\mu W^j_\nu - \partial_\nu W^j_\mu + g\epsilon^j_{kl} W^k_\mu W^l_\nu, \\ B_{\mu\nu} &= \partial_\mu B_\nu - \partial_\nu B_\mu. \end{aligned} \tag{2.22}$$

Physically observable vector bosons are mass eigenstates that can be expressed as linear combinations of the gauge fields. Bosons carrying isospin $T_3 = \pm 1$ are mixed by

$$W^{\pm} = \frac{1}{\sqrt{2}} \left(W^1 \mp iW^2 \right) \tag{2.23}$$

whereas isospinless bosons ($T_3 = 0$) are combined via the *weak mixing angle* θ_w

$$\begin{pmatrix} \gamma^0 \\ Z^0 \end{pmatrix} = \begin{pmatrix} \cos\theta_w & \sin\theta_w \\ -\sin\theta_w & \cos\theta_w \end{pmatrix} \cdot \begin{pmatrix} B^0 \\ W^0 \end{pmatrix} \tag{2.24}$$

where also the photon γ is appearing that is known to be the gauge boson of QED. This *electroweak unification* of QED and weak interaction decouples for energies below the magnitude of the Z^0 mass due to spontaneous symmetry breaking. For high energies, electromagnetic and weak interaction become indistinguishable. Similar to QCD, the gauge field $W^j_{\mu\nu}$ in (2.22) implies a self-coupling of QFD bosons.

2.6 The Higgs Mechanism

The Higgs mechanism is an attempt to explain the electroweak Bosons' mass without renouncing gauge invariance [13]. To achieve this, Bosons are assumed to interact with an additional, self-interacting *Higgs field* that owns a "hidden" symmetry.

This field is postulated as a doublet of a charged (ϕ^+) and a neutral (ϕ^0) complex component

$$\phi = \begin{pmatrix} \phi^+ \\ \phi^0 \end{pmatrix} = \begin{pmatrix} \phi_1 + i\phi_2 \\ \phi_3 + i\phi_4 \end{pmatrix} \tag{2.25}$$

The corresponding derivative

$$D_\mu = \partial_\mu + ig\sigma^j W_\mu^j + i\frac{g'}{2} Y B_\mu, \tag{2.26}$$

with W_μ and B_μ known from (2.21) leads to the Lagrangian

$$\mathcal{L}_{\text{higgs}} = (D_\mu \phi)^\dagger \, (D^\mu \phi) - V(\phi). \tag{2.27}$$

As the photon γ couples to ϕ^+, it needs to remain massless. So, the ϕ^+ vacuum expectation value has to be 0. Massive Bosons mass terms are produced by ϕ^0 by assuming a potential

$$V(\phi) = -\mu^2 \phi^\dagger \phi + \lambda \left(\phi^\dagger \phi\right)^2, \quad \lambda > 0. \tag{2.28}$$

Choosing a $\mu^2 > 0$ in (2.28) leads to a circular shaped minimum with radius $\sqrt{\mu^2/2\lambda}$ around the vacuum expectation value at $V(\phi = 0)$ (Fig. 2.1).

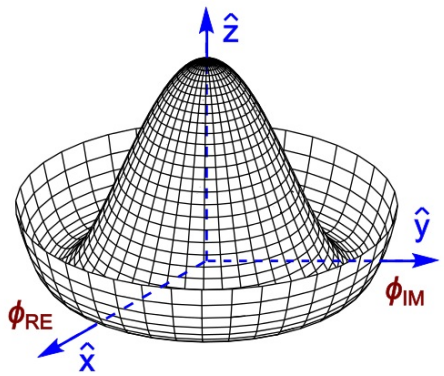

Figure 2.1: Potential of the Higgs-Field ϕ with a continuous, circular minimum around the vacuum expectation value $\phi(0)$. Image taken from [14].

With choosing an arbitrary minimal state out of the infinite possibilities, the symmetry is *spontaneously* broken. In this case, QED's symmetry appears as result of this symmetry breaking:

$$SU(2)_L \otimes U(1)_Y \to U(1)_{\text{em}} \tag{2.29}$$

In this state, the field (2.25) can be reparameterised and regauged to

$$\phi(x) = \frac{1}{\sqrt{2}} \begin{pmatrix} 0 \\ v + H(x) \end{pmatrix}, \quad v = \sqrt{\frac{\mu^2}{\lambda}} \tag{2.30}$$

with a new field H, which represents the observable *Higgs-Boson*. Inserting this modified ϕ into (2.27) allows to separate bilinear terms describing the couplings to $W^{\pm}$, Z^0 and γ and extract the resulting masses.

3 Supersymmetry

Supersymmetry (SUSY) introduces the concept of a symmetry between the groups of Bosons and Fermions by associating a superpartner of the corresponding other group to any particle. It is an extension of the Standard Model that is able to answer many open questions previous theories were not able to address. Some problems unanswered by the Standard Model are presented briefly. General concepts of SUSY, the *Minimal Supersymmetric Standard Model* (MSSM) and the role of R-Parity and it's violation (RPV SUSY) are introduced.

3.1 A glance beyond the Standard Model

The Standard Model is very well tested and was widely verified in a lot of experiments in the last decades. Although it is the most precise description of microscopic phenomenology by now, it appears as constructed artificially in parts and a bit improvised. A comprehensive theory is considered to appear more "natural" and to cover a wider range of issues. Some extensions SUSY can provide merit a closer look [15].

3.1.1 Unification of Couplings

Vacuum polarisation require renormalisation of interaction strengths. So, QFT coupling constants $\alpha_i = c_i \cdot g_i^2/4\pi$ become dependent on the energy on which they are observed (*running couplings*):

$$\alpha_i = \alpha_i \left(\frac{Q^2}{\Lambda^2} \right) \text{ with reference scale } \Lambda. \tag{3.1}$$

At low energy, the weak $SU(2)$ and electromagnetic $U(1)$ couplings have different strengths and energy dependencies. At a certain energy level, both couplings meet and share their further behaviour. The interactions combine to a single one and electroweak symmetry breaking is outgrown. However, strong interactions has to be left out by Standard Model renormalisation.

It is natural to assume a *Grand Unified Theory* (GUT) that allows unification of all three interactions at an energy level M_{GUT}. In this case, the standard model's symmetry appears as a broken, more general symmetry G_{GUT}:

$$G_{\mathrm{GUT}} \to SU(3)_C \otimes SU(2)_W \otimes U(1)_Y \tag{3.2}$$

As SUSY introduces new massive particles affecting renormalisation, such a unification can actually be reached at $M_{\mathrm{GUT}} \approx 10^{16}$ GeV if the SUSY mass scale is about 1 TeV (see fig. 3.1). Additionally, the electroweak mixing angle θ_w (2.24) can be reproduced theoretically.

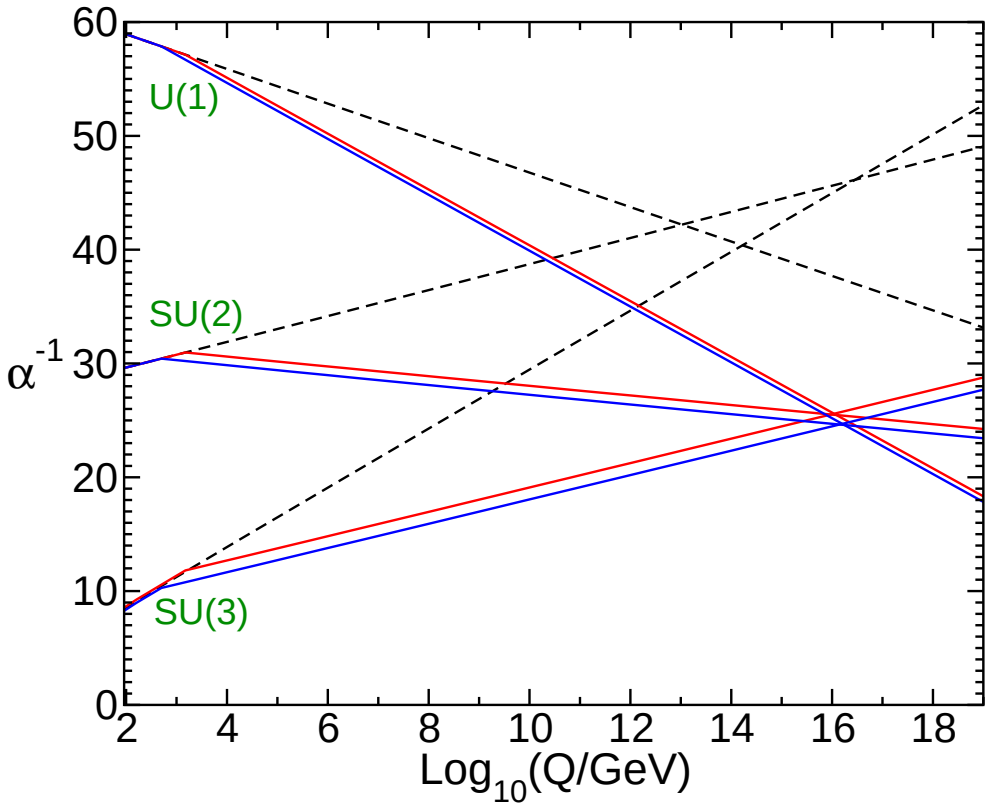

Figure 3.1: Running coupling strengths for electromagnetic $U(1)$, weak $SU(2)$ and strong $SU(3)$ interaction. The dashed lines are for SM, the solid ones for SUSY renormalisation. Taken form [16].

3.1.2 The Hierarchy Problem

The Higgs mass is the combination of the bare boson mass, given through the minimum in the Higgs potential (2.28), and quantum corrections from virtual particles coupling to the field. Latter ones are described by higher terms in perturbation theory as

$$\Delta m_H^2 = -\frac{|\lambda_f|^2}{8\pi^2}\Lambda^2 \tag{3.3}$$

for 1st-order fermion loops (fig. 3.2a) [16]. Here, λ_f is the $H\bar{f}f$ coupling and Λ is a cut-off parameter to prevent the loop integral from diverging and is normally chosen to represent the selected energy scale. Yielding a total mass of order $m_H^{\mathrm{EWK}} \approx 10^2$ GeV for

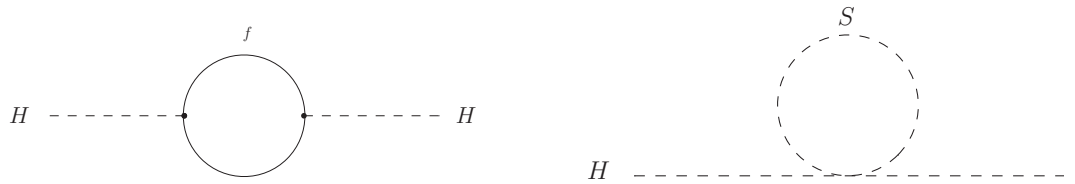

(a) fermion loop (b) scalar loop

Figure 3.2: 1st-order corrections to the Higgs mass

the electroweak- and $m_H^{\mathrm{GUT}} \approx 10^{16}$ GeV for the GUT scale leads to a proportion of

$$\frac{m_H^{\mathrm{EWK}}}{m_H^{\mathrm{GUT}}} \approx 10^{-14}. \tag{3.4}$$

This ratio can only be adjusted by extremely precise *fine tuning* of parameters in a dimension of up to some decimal powers, whose necessity in nature is implausible.

In SUSY, this problem is solved by including superpartners of fermions into correction. Those partners have the same properties like the original particles except they are scalars. Scalar corrections (fig. 3.2b) are similar to (3.3) but have opposite sign, so fermion and scalar corrections cancel each other.

3.1.3 Dark Matter

Several observations in cosmology hint at the existence of *Dark Matter* [17]. Anomalies in the rotational speed of galaxies and power fluctuations in the cosmic microwave background are explained by the presence of non-luminous sources of gravitation. Among others, these can be given by the gas clouds, black holes, remnants from supernovae or planets. A further contribution is given by *weakly interacting massive particles* (WIMPs) which may contribute to the total amount of mass in the universe significantly. They affect gravitational effects but participate hardly in other interactions and thus remain "invisible" for direct observation. Since neutrinos are proved to have mass, they are one kind of WIMP. But current mass limits show them to be far from being able to fill the gap between observed and required mass [18].

The R-parity conserving model of SUSY predicts a bosonic, *lightest supersymmetric particle* (LSP) with a mass in the order of magnitude of 1 TeV which is absolutely stable. Assuming a weakly interacting, *i.e.* neutral particle like the gluino $\tilde{g}$, sneutrino $\tilde{\nu}$ or neutralino $\tilde{\chi}^0$ as LSP, this is a hot candidate for a WIMP to explain the dark matter.

3.2 The Minimal Supersymmetric Standard Model (MSSM)

Introducing symmetries is a method that widened the understanding of correlations in nature often in history of science. For instance, the finding of the Dirac equation (2.7) and the subsequent development of QFT went hand in hand with the discovery of anti-matter.

As seen in sec. 3.1.2 there is a difference in sign between fermionic and bosonic quantum corrections what motivates scenarios assuming a symmetry between fermions and bosons, *i.e.* between matter and interactions. Finally, Supersymmetry postulates a super-symmetric partner to any particle differing only in spin using a SUSY generator $\mathbb{Q}$ [16]:

$$\mathbb{Q}\,|\text{fermion}\rangle = |\text{boson}\rangle\,, \qquad \mathbb{Q}\,|\text{boson}\rangle = |\text{fermion}\rangle\,. \tag{3.5}$$

Every appliance of $\mathbb{Q}$ changes the spin by 1/2 and converts a fermion to a boson and vice versa.

The *Minimal Supersymmetric Standard Model* (MSSM) extends the Standard Model to a supersymmetric model adding the smallest possible number of new particles. Any SM particle field has exactly one supersymmetric partner. Both are taken together to *Supermultiplets*. Adding a fermionic partner of the Higgs leads to gauge anomalies which require to add a second Higgs doublet to the model.

Chiral Supermultiplets			
Name & Symbol		**spin 0**	**spin 1/2**
squarks, quarks (3 generations)	Q	$\begin{pmatrix}\tilde{u}_L & \tilde{d}_L\end{pmatrix}$	$(u_L \quad d_L)$
	$\bar{u}$	$\tilde{u}_R$	u_R
	$\bar{d}$	$\tilde{d}_R$	d_R
sleptons, leptons (3 generations)	L	$(\tilde{\nu} \quad \tilde{e}_L)$	$(\nu \quad e_L)$
	$\bar{e}$	$\tilde{e}_R$	e_R
Higgs, higgsinos	H_u	$(H_u^+ \quad H_u^0)$	$\begin{pmatrix}\tilde{H}_u^+ & \tilde{H}_u^0\end{pmatrix}$
	H_d	$\begin{pmatrix}H_d^0 & H_d^-\end{pmatrix}$	$\begin{pmatrix}\tilde{H}_d^0 & \tilde{H}_d^-\end{pmatrix}$

Gauge Supermultiplets		
Names	**spin 1/2**	**spin 1**
gluino, gluon	$\tilde{g}$	g
winos, W boson	$\widetilde{W}^{\pm} \quad \widetilde{W}^0$	$W^{\pm} \quad W^0$
bino, B boson	$\widetilde{B}^0$	B^0

Table 3.1: Chiral- and gauge supermultiplets in the MSSM. Taken from [16].

SUSY particles are marked with a tilde over their acronym and they are named by prepending '*s*' to the name in case of fermions (slepton, sup) or appending an '*ino*' in case of bosons (wino, bino). Table 3.1 lists all members of the MSSM.

Supermultiplets contain gauge fields and their partners (*gauginos*). Similar to the SM, those mix to mass eigenstates representing observable particles. Thus, the MSSM

predicts linear combinations of neutral gauginos resulting in four *neutralinos*,

$$\widetilde{B}^0, \widetilde{W}^0, \widetilde{H}_u^0, \widetilde{H}_d^0 \rightsquigarrow \widetilde{\chi}_{1,2,3,4}^0 \tag{3.6}$$

charged gauginos mixing to four *charginos*,

$$\widetilde{W}^{\pm}, \widetilde{H}_u^+, \widetilde{H}_d^- \rightsquigarrow \widetilde{\chi}_{1,2}^{\pm} \tag{3.7}$$

and overall five higgs bosons,

$$H_u^0, H_d^0, H_u^+, H_d^- \rightsquigarrow h^0, H^0, A^0, H^{\pm}. \tag{3.8}$$

Since no sparticles in the mass range of the SM have been found yet, their mass must be considerably higher. This implies that SUSY has to be broken. To preserve the property that fermionic and bosonic loop corrections neutralise each other, it is necessary that this is a soft breaking only. A Lagrangian $\mathcal{L}_{\text{soft}}$ describing this symmetry breaking can be constructed, even without knowing the origin of this effect. Taking this into account, a Lagrangian $\mathcal{L}_{\text{MSSM}}$ can be found, whose supersymmetric components can be grouped to a *superpotential*

$$W_{\text{MSSM}} = \bar{u} y_u Q H_u - \bar{d} y_d Q H_d - \bar{e} y_e L H_d + \mu H_u H_d \tag{3.9}$$

using supermultiplets as listed in table 3.1 and 3×3 Yukawa coupling matrices y_i.

3.3 The constrained MSSM (cMSSM)

Due to the need of $\mathcal{L}_{\text{soft}}$, the MSSM contains 105 free parameters for masses, phases and mixing angles. Furthermore, soft symmetry breaking cannot be realised within the MSSM regarding the supermultiplets (3.1) only without violating gauge invariance [15]. This inconvenience is avoided by introducing a *visible sector* containing all SM fields and their superpartners and a *hidden sector* responsible for symmetry breaking. Now, submodels of the MSSM can be formulated, depending on the *mediation* between the sectors. By today, the mechanisms *gravity-*, *gauge-*, *anomaly-* and *gaugino* mediation are proposed. The cMSSM (or mSUGRA) model is a gravity mediated model containing *running masses* which unite at the GUT scale (fig. 3.3). At this scale, the MSSM parameters show mutual dependencies. Hence, they can be combined to five remaininng ones:

- m_0: The universal scalar sfermion mass at GUT scale
- $m_{1/2}$: The universal gaugino mass at GUT scale
- A_0: The universal trilinear couplings at GUT scale
- $\tan\beta$: The ratio of Higgs vacuum expectation values H_u^0/H_d^0
- $\operatorname{sgn}\mu$: The sign ($\pm$) of the Higgsino mass term.

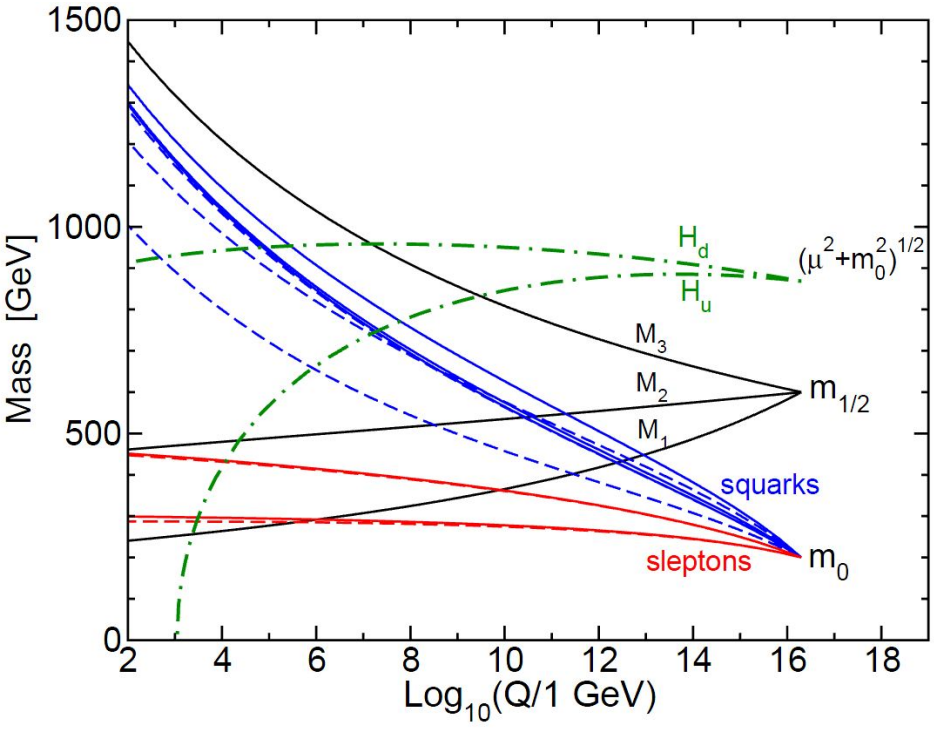

Figure 3.3: Unification of masses in the cMSSM at the GUT scale. Taken from [16].

3.4 The role of R Parity

To distinguish between SM and SUSY particles one can make use of the quantity R-parity [16] which can be constructed as

$$R_p = (-1)^{3(B-L)+2S} \tag{3.10}$$

with baryon number B, lepton number L and spin S. This new multiplicative quantum number is $+1$ for ordinary- and -1 for SUSY particles. As B, L, and S are conserved quantities within today's experimental experience, also R is assumed to be conserved in many models (*R-parity conserving* or RPC models). In this case, SUSY particles can only be produced pairwise whereas sparticles can only decay to particle-sparticle pairs. This may lead to long decay chains with very complicated signatures which are difficult to access experimentally. The chain ends when the *Lightest Supersymmetric Particle* (LSP) is reached, which is hard to detect, similar to a neutrino. Neutral RPC-SUSY LSPs are candidates for dark matter (sec. 3.1.3)

The superpotential (3.9) is the most general representation of SUSY if R is conserved. Regarding quantum numbers as conserved is convenient and is, in a kind, in accordance with tradition of physics, but it is not theoretically mandatory. Dismissing the limitation of declaring a conserved R parity allows to extend the superpotential by the term

$$W_{\text{RPV}} \supset \frac{1}{2}\lambda_{ijk}L_iL_j\bar{E}_k + \lambda'_{ijk}L_iQ_j\bar{D}_k + \kappa_iL_iH_u + \frac{1}{2}\lambda''_{ijk}\bar{U}_i\bar{D}_j\bar{D}_k \tag{3.11}$$

and still preserve gauge invariance [19]. Here, L, Q and H_u denote lepton-, quark- and Higgs-superdoublets, as $\bar{E}, \bar{U}$ and $\bar{D}$ stand for electron-like lepton-, and up/down-like

quark supersinglets, where i, j, k are generation indices. The couplings $\lambda, \lambda', \lambda''$ and κ are additional parameters in this *R-parity violating* (RPV, $\not{R}_p$) model, where R is no longer a conserved quantity. Within this, the λ, λ' and κ coupling allow a violation of the lepton number L while λ'' allows a baryon number B violation. The bilinear mass coupling term $\kappa_i L_i H_u$ mixes lepton and Higgs superfields. In the used model, this can be rotated away by choosing a suitable redefinition of L and H [20].

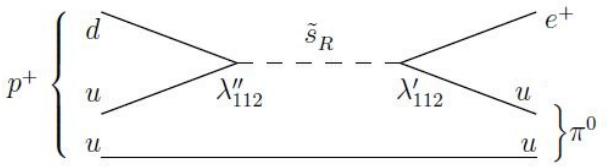

Figure 3.4: Exemplarily proton decay ($p \to e^+\pi^0$) via RPV λ' and λ'' couplings violating B and L simultaneously. Taken from [16].

As an implication, in RPV SUSY, sparticles can be produced singly, *i.e.* resonantly, and decay directly to SM particle pairs. Furthermore, the LSP is not stable anymore. That is why it can no longer hold for a dark matter candidate in this scenario.

Simultaneously B and L violation would allow rapid proton decay (Fig. 3.4), which is in contradiction to experimental observation. For the rest of this thesis only the B_3 or *baryon triality* model will be used that forbids the $\bar{U}\bar{D}\bar{D}$ coupling. Another benefit of this model is the ability to explain neutrino masses applying higher order mass corrections [21].

4 Experimental Facilities & Data Taking

The data used for this analysis is taken from the *Compact Muon Solenoid* (CMS) detector which is an experiment to examine results of particle collisions realised by the *Large Hadron Collider* (LHC) at the European Organization for Nuclear Research (CERN) near Geneva, Switzerland. The recorded raw data is stored and conditioned to analysable data structures with the *Worldwide LHC Computing Grid* (WLCG).

4.1 The Large Hadron Collider (LHC)

The LHC is a circular synchrotron particle accelerator in a tunnel 26.7 km in circumference [22]. It is designed to accelerate protons or heavy ions in counter-rotating beams which are made to collide at predefined interaction points where the interaction can be observed by experiments. The four major experiments are the multi purpose detectors ATLAS [23] and CMS [24] (sec. 4.2) who are searching for any kind of new physics in pp collisions and the specialised experiments ALICE [25], designed to study nucleus-nucleus interactions in heavy ion collisions as well as LHCb [26], looking for effects accessible via B-meson physics, like CP violation. Furthermore, only the pp mode is regarded.

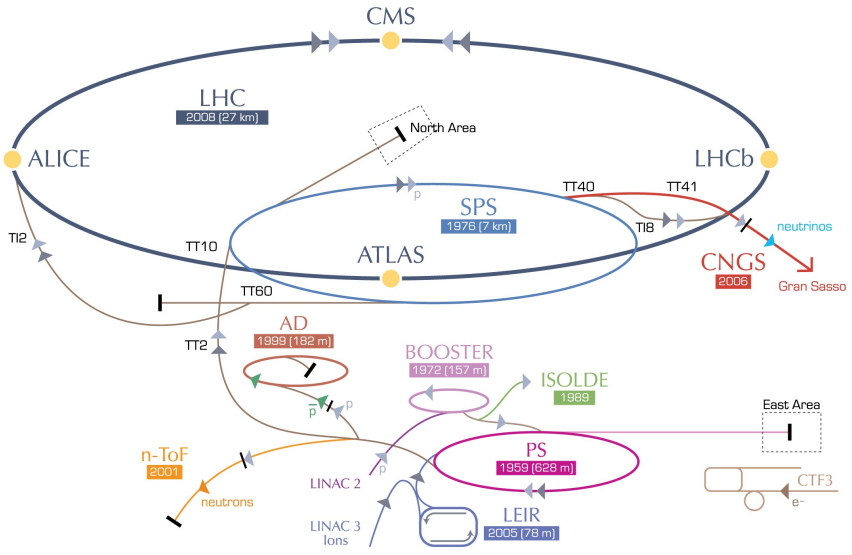

Figure 4.1: The CERN accelerator complex. Protons are preaccelerated in the LINAC 2 (50 MeV), BOOSTER (1.4 GeV), PS (25 GeV) and SPS (450 GeV) before they are injected into the LHC and accelerated to final energy (4 TeV at present). Taken from [27].

Protons are produced in gas ionisation and have to be preaccelerated gradually before they are injected into the LHC. Therefore, smaller accelerators, partly originating from

previous experiments, are used (Fig. 4.1). The linear accelerator LINAC 2 brings them up to a base level of 50 MeV before they enter the synchrotron chain of BOOSTER (1.4 GeV), PS (25 GeV) and SPS (450 GeV). Then they are injected into the two beampipes of LHC and brought to target energy. Between 2010 and 2011 this was 3.5 TeV per beam, thus the center of mass energy was $\sqrt{s}$=7 TeV. Between 5th of April and 17th of December 2012 a $\sqrt{s}$ of 8 TeV was reached. Presently (2013), the machine is upgraded to reach it's design c.m. energy of 14 TeV approximately in 2015.

The relevant quantity to measure beam intensity is the *Luminosity* $\mathscr{L}(t)$ and the integrated luminosity $L = \int \mathscr{L} dt$. These relate the interaction specific *cross section* σ to the total number of interactions in time span t:

$$N = L \cdot \sigma \tag{4.1}$$

In 2012, the LHC delivered a total integrated Luminosity of $23.27\,\mathrm{fb}^{-1}$ to the CMS experiment [28].

4.2 The Compact Muon Solenoid (CMS)

The CMS experiment is a multi purpose particle detector located at LHC's interaction point 5 on the french part of the accelerator ring [24]. It is designed to detect all measurable decay products from proton-proton, proton-Ion or Heavy Ion collisions with a combination of various subdetectors. Those are placed around the beam axis (*barrel*) in an axial symmetry. Additionally there are flat, vertical components covering the openings of the barrel (*Endcaps*) to detect particles with narrow angles in respect to the beam axis.

The central device is a solenoid magnet, whose superconducting coil divides the inner components from the outer muon system.

Within the detector, a right-handed coordinate system is used. The origin is the nominal interaction point. The z axis is chosen to point along the counter-clockwise beam axis, whereas the x axis points towards the centre of the LHC ring and the y axis is the common perpendicular. Spherical coordinates are expressed in the azimuthal angle ϕ with respect to the z axis and the pseudorapidity

$$\eta = -\ln \tan\left(\frac{\theta}{2}\right), \tag{4.2}$$

which is a representation of the polar angle θ with respect to the z axis in a kind that $\Delta\eta$ is a Lorentz invariant measure. Figure 4.2 gives an overview over the detector geometry. In the following, the subdetector components are presented in detail from inner to outer.

4.2.1 Inner Tracker

Task of the inner tracker is to measure the tracks of charged particles with highest possible precision. It's radius ranges from 4.4 to 110 cm. The whole tracker is embedded into a homogeneous magnetic field of 4 T that allows to reconstruct particle momenta from curvature radius. The very inner part of the tracker is realised as pixel detector, surrounded by outer silicon strip detector components whose strip surface orientation depend on η. Overall the tracker consists of about $200\,\mathrm{m}^2$ of active detection area covering a range $|\eta| < 2.5$.

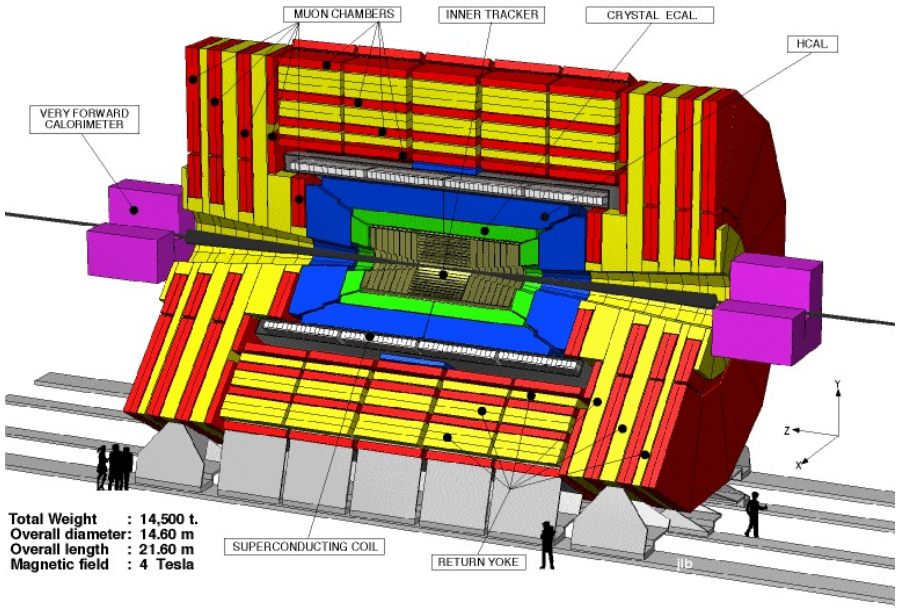

Figure 4.2: Overview of the CMS detector. Taken from [29].

The tracker is able to reconstruct p_T with a resolution of 1-2% for high momentum tracks with p_T up to 100 GeV. Primary- and secondary vertices as well as impact parameters can be reconstructed with a precision of some ten µm.

4.2.2 Electromagnetic Calorimeter

The *electromagnetic calorimeter* (ECAL) measures the energy deposit of electromagnetically interacting, *i.e.* charged, particles. It is made of 61200 lead tungstate ($PBWO_4$) crystals in the barrel plus additional 7324 ones in the endcaps. Electromagnetic showers excite the crystals and lead to scintillation light that is detected by avalanche photodiodes (APD) in the barrel and vacuum photo triodes (VPT) in the endcaps. The high density of $8.28\,\mathrm{g\,cm^{-3}}$ and short radiation length of $X_0 = 0.89\,\mathrm{cm}$ of $PBWO_4$ allow a compact size and fine granularity of the ECAL. The length of the crystals is 230 mm or $25.8\,X_0$ with their font face being in a distance of 1.29 m from the beam axis. Their regeneration time is about 25 ns and therefore short enough to recover between two bunch crossings. The energy resolution is

$$\left(\frac{\sigma(E)}{E}\right)^2 = \left(\frac{s}{\sqrt{E}}\right)^2 + \left(\frac{n}{E}\right)^2 + c^2, \qquad [E] = \mathrm{GeV} \tag{4.3}$$

with a stochastic term s typically of order 2.8%, a noise $n \approx 0.12$ and an offset $c \approx 0.3\%$.

4.2.3 Hadronic Calorimeter

Hadronic decay components are able to pass the ECAL due to their large decay length or missing charge and have to be measured in the *hadronic calorimeter* (HCAL). The barrel component (HB) covers radii from 1.77 to 2.95 m and is realised as a sampling calorimeter of repeating layers of absorber and scintillator. The 16 absorber layers are

made of steel or brass with thicknesses between 40 and 75 mm. They are intended to force hadrons into showers which then can be detected by the scintillator layers. Endcap components (HE) are designed similarly, only in transverse orientation to the beam axis. Unstopped hadrons are finally captured by the outer calorimeter (HO) located beyond the massive magnet coil which acts as final absorber layer. Finally, high η regions are covered by very forward calorimeters (HF).
Pions in the HB reach a resolution of about [30]:

$$\left(\frac{\sigma(E)}{E}\right)^2 \approx \left(\frac{115\%}{\sqrt{E}}\right)^2 + (5.5\%)^2 \,. \tag{4.4}$$

4.2.4 Muon System

Muons play a crucial role in signatures of many processes, either within or beyond the Standard Model, so they are worth to be regarded with special attention. Since they are minimal ionising particles they pass the calorimeters. As the experiment's name suggests, CMS contains a sophisticated muon detector component to measure muons precisely.

The muon system consist of 25 000 m^2 of detection planes in total. In the barrel region ($|\eta| < 1.2$) barrel drift tube (DT) chambers are used, which are arranged in four concentric cylinders around the beam axis (*stations*). Each station has 60 (inner-) or 70 (outermost layer) drift chambers. Each chamber is composed of several sublayers staggered by half a cell width. The wires of the outer sublayers are oriented parallel to the beam line to provide track measurement in the $(r - \phi)$ plane whereas the inner ones are aligned orthogonally to measure the z coordinate. On the inner- and outermost layers, an additional Resistive Plate Chamber (RPC) gaseous parallel-plate component is attached, that allows very precise time tagging of particle transitions.

In the endcaps, cathode strip chambers (CSC) are used. Each chamber is shaped trapezoidally to allow piecewise coverage of the full ϕ range. CSCs are realised as multiwire proportional chambers comprised of six anode wire planes alternating with cathode panels. The endcaps cover the range $1.2 < |\eta| < 2.4$.

All detection planes are mounted between the three layers of the iron return yoke. A 2 T magnetic field covers the whole muon system. The overall reconstruction efficiency of the entire muon system is about $95 - 99\%$ and the momentum resolution reaches 5% for high momentum muons ($p_T \approx 1\,\mathrm{TeV}$).

4.3 The Worldwide LHC Computing Grid (WLCG)

The LHC produces an amount of data of about 15 PB annually over a time period of approximately 15 years [31]. This data has to be processed, stored and made accessible to over 5000 scientists in more than 500 research institutes worldwide. The needed computing capacity is $\mathcal{O}(10^5)$ CPUs with upward tendency.

To grant minimal risk of data loss or stoppage of processing work, the needed computer power is spread globally to numerous computing centres connected through a common

topology. The grid is designed to allow maximum redundancy using a four-tiered structure:

Tier 0: Experiments deliver raw data with a rate of $\mathcal{O}(1 - 1.5\,\mathrm{GB/s})$. This data undergoes a first-pass reconstruction and is stored. A copy of this data is distributed to Tier 1 level. The Tier 0 is a single centre located at CERN.

Tier 1: Worldwide exist currently 10 Tier 1 centres. They perform further, experiment specific selection on the raw data, distribute the outputs to Tier 2 and serve as data storage for their results. Furthermore they hold a backup of raw data from Tier 0 and can be used for extensive simulation processes.

Tier 2: The roughly 150 Tier 2s are hosted at universities and institutes worldwide, including the RWTH Aachen University. Their role is to provide computing power to the end user and enable him to run individual selections, analyses and Monte Carlo event simulations. Data is cached temporarily only. For permanent storage they are connected to Tier 1s.

Tier 3: Tier 3s are mainly internal networking facilities of connected institutions. Their unused capacities can be made accessible to the grid.

4.4 Trigger System and Data Handling

Raw data from the detector has to be selected and processed to results with physical expressiveness before it is stored. Therefore, a capable trigger system and software framework is vital.

4.4.1 Trigger System

The LHC is designed for a bunch crossing interval of 25 ns or a corresponding crossing frequency of 40 MHz [24]. Since this amount of data is impossible to store and process, the number of events has to be reduced drastically. This is the task of the trigger system. CMS uses a two step trigger designed to reduce the event rate by at least 10^6.

The *Level-1 trigger* (L1) is an electronic trigger containing multiple components. *Local Triggers* are embedded logical circuits integrated in the calorimeter and muon system devices directly. They capture the energy deposit or track pattern of the single subdetector device and distribute them to *Regional Triggers*. These collect the entire data of the subdetector and do a first quality evaluation by classifying entries to *e.g.* particle candidates on the basis of ranked characteristics. All regional information is transferred to the *Global Trigger* which decides to reject or accept an event at L1 stage. L1 components, that are not an element of the detector devices, are housed in a control room just next to the experiment's cavern. This trigger reduces the event rate to $30 - 100\,\mathrm{kHz}$.

Accepted events are forwarded to the *High Level Trigger*. This is a software based trigger running on a computing farm with $\mathcal{O}(1000)$ CPUs. Here, complex algorithms run on the events and lead to further selection. The HLT reduces the output rate to $\approx 400\,\mathrm{Hz}$. Only events passing this trigger stage are stored.

4.4.2 Software Framework

Offline computing is based on the *CMS Software* package (CMSSW) [32]. This provides an object oriented C++ framework for data modelling and analysis (*Physics Analysis Toolkit*, PAT) as well as a variety of different command line tools. All event data is stored in 'PAT tuples' and can be analysed according to personal demands. For data exchange, a binary tree structure, provided and readable by the analysis framework `ROOT` [33] is used.

5 Analysis

A search for a resonant $\tilde{\nu}_\tau$, decaying into an $e\tau$ pair is performed. The underlying conditions to model this process are introduced. Parts of the analysis are event selection, signal simulation, fitting simulated distributions to data and estimation of the event yield in the search region. Finally an upper limit on the process' cross section and the $\tilde{\nu}_\tau$ mass is computed.

5.1 Event Signature

5.1.1 Object of Search

In the following, a RPV mSUGRA model is considered. Augmenting the mSUGRA model with a possible RPV scenario requires to enhance the mSUGRA parameter space by a 6th element Λ out of the Yukawa couplings from the superpotential (3.11) [34]:

$$\Lambda \in \left\{\lambda_{ijk}, \lambda'_{ijk}, \lambda''_{ijk}\right\} \quad \text{at} \quad M_{\text{GUT}} \tag{5.1}$$

The choice of Λ affects the sparticle mass spectrum. Choosing $\Lambda = \lambda'$ allows the sneutrino $\tilde{\nu}_i$ to be a candidate for the LSP. Here, the τ-sneutrino ($\tilde{\nu}_\tau$) is chosen to take up this

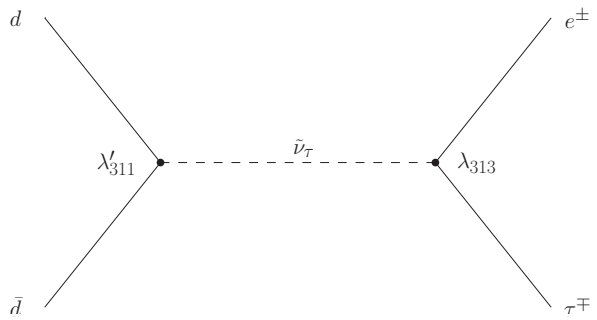

Figure 5.1: Feynman graph for the process $d\bar{d} \to \tilde{\nu}_\tau \to e\tau$.

role. This can be produced resonantly in $q\bar{q}$, $q \in \{d, s, b\}$ annihilation via the $LQ\bar{D}$ coupling λ' and decays with a very narrow width depending on λ' and the $LL\bar{E}$ coupling λ to a dileptonic final state. In the following, the process $d\bar{d} \to \tilde{\nu}_\tau \to e\tau$ via λ'_{311} and λ_{313} is regarded (Fig. 5.1). All other λ'_{ijk} and λ_{ijk} are assumed to be zero.

5.1.2 Observables

Measurands used in this analysis are the kinematic properties of the decay products p_T and E_T, which are the projection of the momentum p and energy E on the (unboosted) transverse direction, the angular quantities ϕ and η as well as the *Missing Transverse Energy* (MET, $\not{E}_T$), which is the imbalance in the p_T of all reconstructed particles originating in a common event, quantises undetected components and measures uncertainties.

Furthermore, geometric data like vertex positions and track information is available.

Additionally the *distance* in the $(\eta - \phi)$-plane or *cone size*

$$\Delta R = \sqrt{(\Delta\eta)^2 + (\Delta\phi)^2} \tag{5.2}$$

is of special interest. Besides, different properties can be encapsulated in topological variables. This analysis makes use of the *dileptonic transverse mass*

$$M_T = \sqrt{2 \cdot p_T^e \cdot p_T^\tau \cdot (1 - \cos\Delta\phi(e,\tau))} \tag{5.3}$$

and the *scalar sum*

$$S_T = p_T^e + p_T^\tau + \sum_{\text{jets}} p_T^{\text{jet}} + \not{E}_T. \tag{5.4}$$

5.1.3 Particle Reconstruction

Electrons are reconstructed with the GSF algorithm [35] by means of ECAL cluster entries and tracking information. This algorithm yields various additional quantities that can be used for isolation and quality evaluation.

Hadrons and $\not{E}_T$ are reconstructed as Particle-Flow objects [36]. For this, all information derived from all subdetector components is combined to a particle object containing all data of the involved constituents.

Jets are bundles of several particles that arise from hadronisation of showers of quarks or gluons. The trajectories are close to the original parton's momentum direction. They are reconstructed from particle flow data of its constituents by the use of the *anti-k_t* jet clustering algorithm [37]. This procedure defines *distances* d_{ij} between entities i and j:

$$d_{ij} = \min\left(p_{\mathrm{T}i}^{-2}, p_{\mathrm{T}j}^{-2}\right) \frac{\Delta y_{ij}^2 + \Delta\phi_{ij}^2}{D^2} \tag{5.5}$$

with a parameter D, chosen to be 0.5, and the rapidity

$$y = \frac{1}{2}\ln\left(\frac{E + p_L}{E - p_L}\right) \tag{5.6}$$

of a particle with Energy E and longitudinal momentum p_L. The particles i and j with smallest d_{ij} are merged to a new pseudoparticle. This recombination is reiterated until d_{ij} equals $p_{\mathrm{T}i}^{-2}$, which is a measure for the distance between entity i and the beam. The result is stored as *particle flow jet*.

τs have a very short lifetime. Due to their mass of 1.78 GeV they decay within a length of $c \cdot \tau \approx 87\,\mu\text{m}$ and therefore within the beam pipe. Possible decay channels are shown in Fig. 5.2. Leptonic final states ($e\,\nu_e\,\nu_\tau$ or $\mu\,\nu_\mu\,\nu_\tau$) are hard to distinguish from prompt leptons, so they are unsuitable for τ reconstruction. Quarks in the final state combine to hadrons, namely π^- ($\bar{u}d$) or, if the τ's mass is sufficient, to ρ^- or a_1^- resonances which decay to combinations of $\pi^\pm$ and π^0 on their part. In rare cases, a Kaon K^- ($\bar{u}s$) is produced instead of a π. This decays in $\pi^\pm\pi^0$ combinations as well, so, with a branching ratio of $\approx 65\%$, a τ decays to a hadronic final state with $n = 1$ or 3 charged π (n-prong),

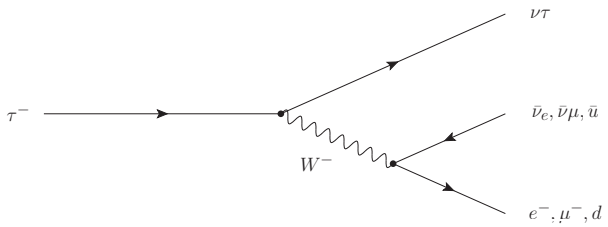

Figure 5.2: Feynman graph for the τ decay.

Decay mode	Resonance	Resonance mass	BR (%)
$\tau^- \to h^-\nu_\tau$			11.6 } 1 prong
$\tau^- \to h^-\pi^0\nu_\tau$	ρ^-	770 MeV	26.0 } 1 prong
$\tau^- \to h^-\pi^0\pi^0\nu_\tau$	a_1^-	1200 MeV	9.5 } 1 prong
$\tau^- \to h^-h^+h^-\nu_\tau$	a_1^-	1200 MeV	9.8 } 3 prong
$\tau^- \to h^-h^+h^-\pi^0\nu_\tau$			4.8 } 3 prong

Table 5.1: Hadronic decay modes of the τ^-. h can be π or K. Taken from [38].

accompanied by several π^0 as the case may be. Table 5.1 sums up all relevant hadronic τ decay modes. The very rare 5-prong mode is omitted.

The decay length of a charged π is $c \cdot \tau \approx 7.8\,\mathrm{m}$ and therefore it is stable within the scope of the detector. A π^0 decays almost instantaneously to a γ pair. To reconstruct hadronic τs (τ_h), the *Hadron Plus Strips* (HPS) algorithm is used [38]. This is a method that

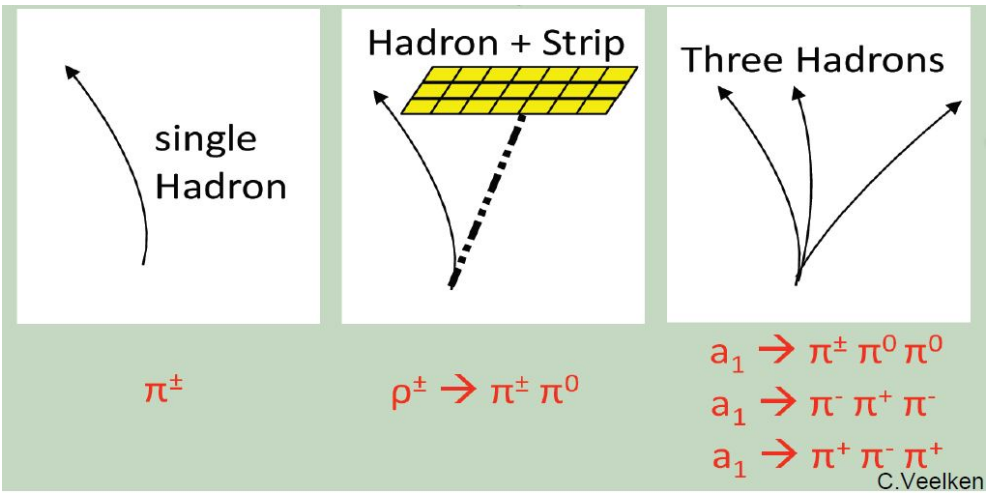

Figure 5.3: Illustration of different τ_h decay modes recognised by the HPS algorithm. Taken from [39].

identifies particular signatures of the different n-prong decay modes within a particle flow jet. These modes are illustrated in fig. 5.3.

A particle flow jet comes into consideration as τ candidate, if it contains one or three charged hadrons. As they follow a bent trajectory in the detector's magnetic field, they can be distinguished from the γs originating from π^0 decays. ECAL entries that are identified as γ are denoted 'strips'. The fine granularity of the ECAL crystals allow to

Threshold	Efficiency		
	loose	*medium*	*tight*
$p_t^\tau > 15\,\text{GeV}$	0.46	0.34	0.23
$p_t^\tau > 20\,\text{GeV}$	0.50	0.37	0.25

Table 5.2: Efficiencies of the HPS algorithm for $p_T^\tau < 150\,\text{GeV}$, determined from $Z \to \tau\tau$ MC events. For high p_T τs, the efficiencies drop significantly. Taken from [38].

separate multiple γ entries belonging to the same τ decay. Two γs are considered to be a pair, if their relative distance is within a window of size $\Delta\eta = 0.05$ and $\Delta\phi = 0.20$. In this case, their invariant mass is reconstructed and undergoes a plausibility check to verify the origin of γ pairs to be in a common π^0 decay.

The HPS algorithm classifies τ_h candidates in four categories for reconstruction:

1. *Single hadron*, which cover the $h^-\,\nu_\tau$ mode and the $h^-\,\pi^0\,\nu_\tau$ cases, where at least one γ from the π^0 decay fell short of the minimum requirement to have a $p_T > 1\,\text{GeV}$.

2. *One hadron + one strip* deals with the mode $h^-\,\pi^0\,\nu_\tau$ where the γ pair can not be separated properly.

3. *One hadron + two strips* is for the proper $h^-\,\pi^0\,\nu_\tau$ case with separated γs.

4. *Three hadrons* for the 3-prong case $h^-\,h^+\,h^-\,\nu_\tau$ where all h are required to come from the same secondary vertex.

The remaining cases $h^-\,\pi^0\,\pi^0\,\nu_\tau$ and $h^-\,h^+\,h^-\,\pi^0\,\nu_\tau$ are ascribed to one of the named topologies. To identify a τ finally, several additional criteria must be fulfilled:

- All hadrons and strips have to be within a cone of $\Delta R = 2.8\,\text{GeV}/p_T^{reco}$, where p_T^{reco} denotes the transverse momentum of the reconstructed τ candidate.
- The reconstructed momentum $\vec{p}_\tau$ has to match the direction of the original particle flow jet within a maximum distance of $\Delta R = 0.1$.
- Reconstructed π^0 have to be within a mass window of $50 - 200\,\text{MeV}$.
- Masses for ρ must be in the range $0.3 - 1.3\,\text{GeV}$.
- The a_1 mass has to be between 0.8 and 1.5 GeV.
- No other particles above a certain threshold are allowed to be in a cone of radius $\Delta R = 0.5$ around the direction of the τ.

The threshold in the isolation criteria mentioned in the last point is specified by three working points, *tight*, *medium* and *loose* where the 'strength' of a point indicates the probability of jets being misidentified as τ. The *loose* working point corresponds to a probability of $\approx 1\%$. Expected efficiencies of this algorithm are shown in table 5.2.

5.1.4 RECO samples

To probe the performance of the identification and reconstruction capabilities, simulated events are regarded before (GEN or 'truth' level) and after (RECO level) simulation of the detector response. Possible measures are the efficiency

$$\varepsilon = \frac{\text{number of RECO particles } (e/\tau) \text{ matched to a GEN one}}{\text{total number of GEN particles}}, \tag{5.7}$$

describing the fraction of identified particles within the total amount, and the fake proportion

$$p_{\text{fake}} = \frac{\text{particles mistakenly identified as } e/\tau}{\text{correctly identified particles}}, \tag{5.8}$$

describing the probability of a RECO particle to be identified wrongly is calculated as a function of p_T^{reco} and η^{reco} (Fig. 5.4). Only the high p_T region is regarded.

This calculation is based on a privately simulated signal of the process (Fig. 5.1) with $m_{\tilde{\nu}_\tau} = 1.4\,\text{TeV}$. The simulation is performed by HERWIG 6.5 [40] for the SUSY process, PYTHIA 6 [41] for particle showering and GEANT4 [42] for the detector response.

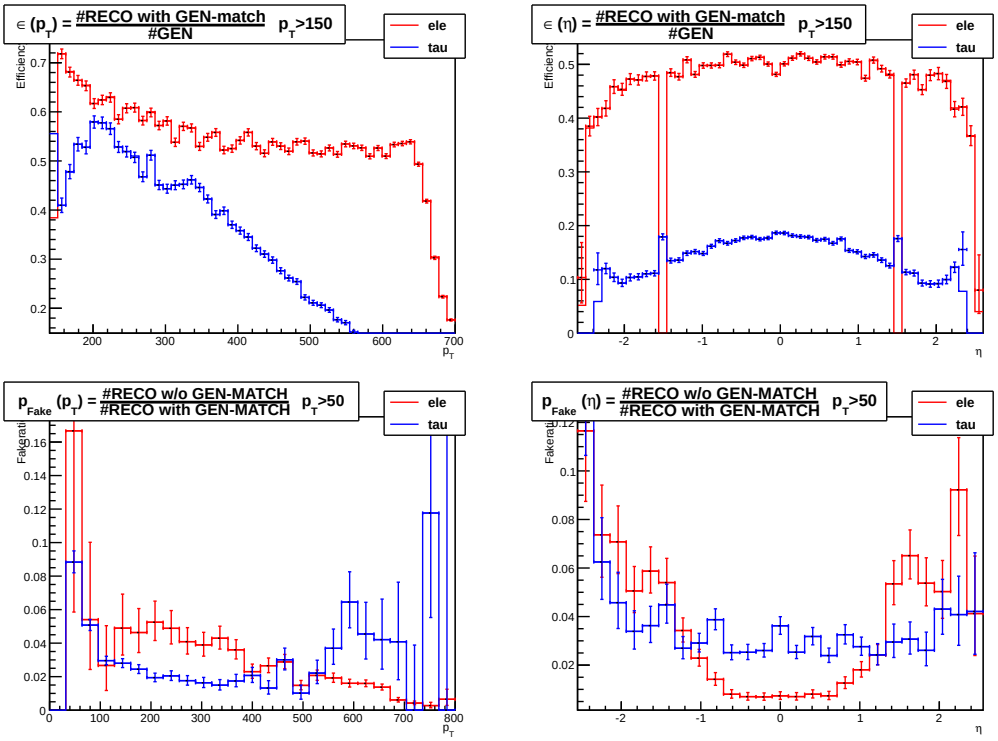

Figure 5.4: Efficiency (upper) and fake proportion (lower) of simulated MC signal as a function of p_T^{reco} (left) and η^{reco} (right).

Dataset	σ_{LO} (pb)	Events
DYJetsToLL_M-50_TuneZ2Star_8TeV-madgraph-tarball	2950.0	30 459 502
QCD_HT-100To250_TuneZ2star_8TeV-madgraph-pythia	1.04×10^7	50 129 518
QCD_HT-250To500_TuneZ2star_8TeV-madgraph-pythia6	2.76×10^5	27 062 078
QCD_HT-500To1000_TuneZ2star_8TeV-madgraph-pythia6	8426.0	30 599 292
QCD_HT-1000ToInf_TuneZ2star_8TeV-madgraph-pythia6	204.0	13 823 863
WJetsToLNu_PtW-50To70_TuneZ2star_8TeV-madgraph	811.2	48 426 609
WJetsToLNu_PtW-70To100_TuneZ2star_8TeV-madgraph	428.9	22 447 541
WJetsToLNu_PtW-100_TuneZ2star_8TeV-madgraph	228.9	12 742 382
TTJets_MassiveBinDECAY_TuneZ2star_8TeV-madgraph-tauola	136.3	6 923 750
WWJetsTo2L2Nu_TuneZ2star_8TeV-madgraph-tauola	4.7	1 933 235
WZJetsTo2L2Q_TuneZ2star_8TeV-madgraph-tauola	1.755	3 215 990
WZJetsTo3LNu_TuneZ2_8TeV-madgraph-tauola	0.8674	2 017 979
WZJetsTo2Q2Nu_TuneZ2star_8TeV-madgraph-tauloa	0.705	942 547
ZZJetsTo2L2Q_TuneZ2star_8TeV-madgraph-tauola	0.91	1 936 727
ZZJetsTo4L_TuneZ2star_8TeV-madgraph-tauola	0.1296	4 807 893
Common suffix: .../Summer12_DR53X-PU_S10_START53_V7A-v1/AODSIM		

Table 5.3: Used background Monte Carlo samples with LO cross section and number of events. All datasets belong to the official 'Summer12' CMS MC production campaign.

5.2 Used Datasets

5.2.1 Background Signals

The process $d\bar{d} \to \tilde{\nu}_\tau \to e\tau$ (Fig. 5.1) yields a clear dileptonic *opposite sign, different flavour* (OSDF) signature. However this is not a unique characteristic of this particular process. Other processes leading to the same signature form a background that has to be distinguished from the signal. Table 5.5 shows leading order Feynman graphs that contribute to the background. Dileptonic final states are generated mainly by Drell-Yan ($Z/\gamma \to l^+l^-$) (Fig. 5.5a), Di-Boson processes (Fig. 5.5b-f) and $t\bar{t}$ (Fig. 5.5g,h). Final states created in pp collisions imply a high hadronic activity resulting in the presence of collateral jets out of g radiation, $q\bar{q}$ hadronisation, hadronic decays in secondary vertices or pileup. Those jets can be misidentified as leptons, especially as τ, so that even processes with a single lepton in the final state can mimic a signal. Due to it's high cross section, single W decay (Fig. 5.5i) is one of the dominant backgrounds. Single t, like the tW process in (Fig. 5.5j) turned out to be negligible.

The background is modelled by Monte Carlo simulations provided by the CMS collaboration. Processes are calculated by use of of the MADGRAPH event generator [43] and supplemented by PYTHIA 6 shower simulation [41]. They have been proved to be the most reliable in high p_T regions. Simulation of the detector response has been performed by GEANT4 [42]. Table 5.3 lists all used MC datasets, leading order cross sections and the number of simulated events.

5.2.2 Data Samples

Data are taken with the detector and preselected by the L1 and HL triggers before they are delivered to the T0 and stored in RAW format [24]. Under high computational

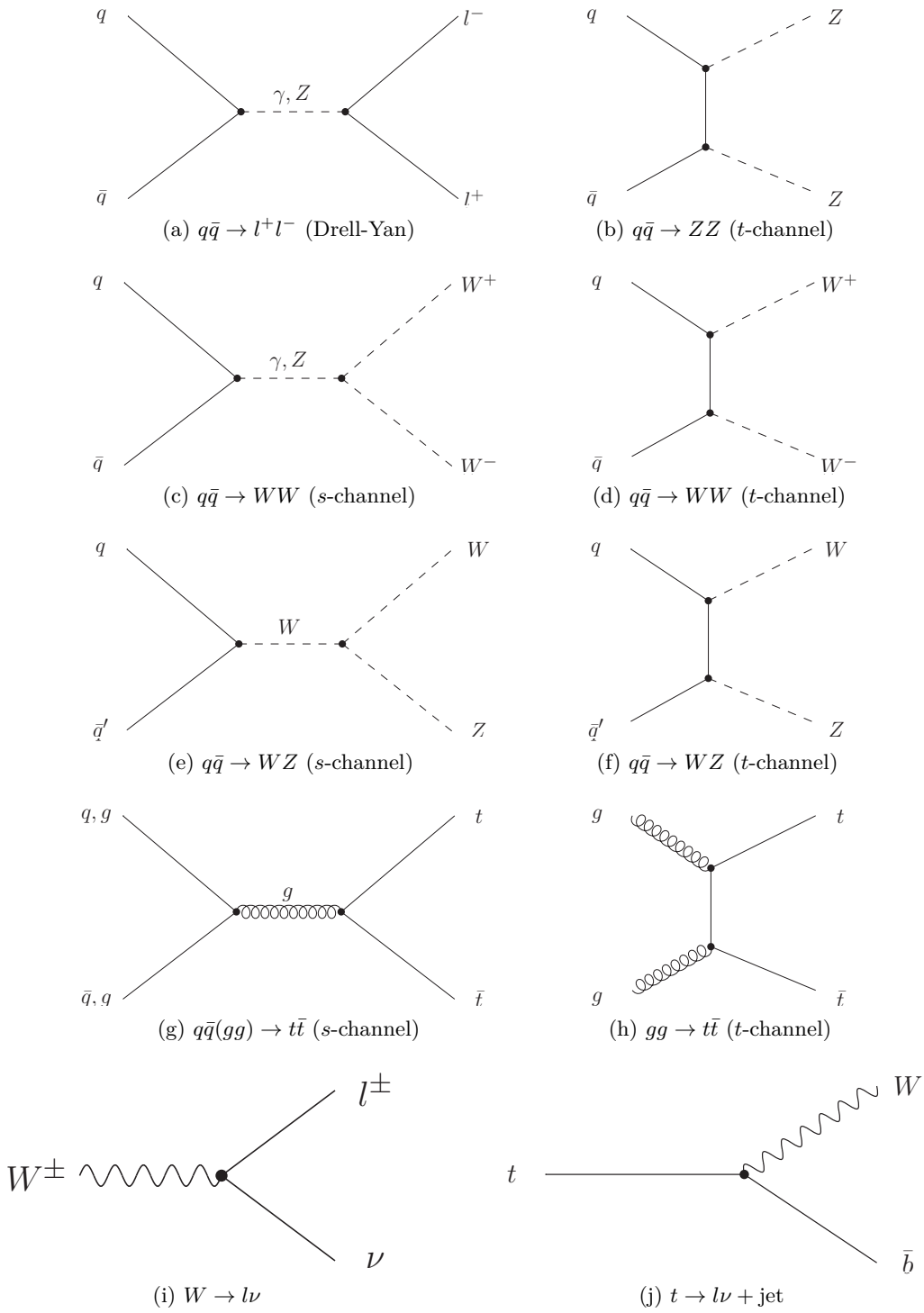

(a) $q\bar{q} \to l^+l^-$ (Drell-Yan) (b) $q\bar{q} \to ZZ$ (t-channel)

(c) $q\bar{q} \to WW$ (s-channel) (d) $q\bar{q} \to WW$ (t-channel)

(e) $q\bar{q} \to WZ$ (s-channel) (f) $q\bar{q} \to WZ$ (t-channel)

(g) $q\bar{q}(gg) \to t\bar{t}$ (s-channel) (h) $gg \to t\bar{t}$ (t-channel)

(i) $W \to l\nu$ (j) $t \to l\nu +$ jet

Figure 5.5: Leading order Feynman graphs for processes $pp \to l^+l^- + X$ contributing to an *opposite sign, different flavour* (OSDF) signature (a-h). Outgoing W and t are intermediate and decay via (i) and (j) to states containing a l.

Dataset	**Runs**	$\int L\,dt$ (fb^{-1})
SingleElectron/Run2012A-13Jul2012-v1/AOD	190645-193621	0.81
SingleElectron/Run2012B-13Jul2012-v1/AOD	193834-196531	4.25
SingleElectron/Run2012C-PromptReco-v1/AOD	198049-198522	0.49
SingleElectron/Run2012C-PromptReco-v2/AOD	198954-203002	4.90
SingleElectron/Run2012D-PromptReco-v1/AOD	203894-208357	5.11
Total		15.55

Table 5.4: Datasets from the 2012 period ($\sqrt{s} = 8\,\mathrm{TeV}$) used for the analysis.

effort, they are reconstructed to high-level *physics objects* there (RECO). Finally, it is compressed to *Analysis Object Data* (AOD) format and stored. At this stage, it is a accessible for offline analyses.

Depending on specific trigger paths released in the HLT, all datasets of the 2012 run are grouped into different categories. Along with some unlisted categories for special purposes these are:

- SingleElectron, SingleMu
- DoubleElectron, DoubleMu
- ElectronHad, MuHad, PhotonHad
- Tau
- TauPlusX
- Photon
- MET
- Jet, MultiJet, BTag

This grouping is not exclusive, so events may be contained in several categories at the same time.

As the τ trigger suffered from technical difficulties during the Summer 2012 data taking period and electron reconstruction grants a better resolution for event selection criteria, this analysis is based on the 'SingleElectron' data. Table 5.4 shows a detailed listing of the used datasets. The overall data amount treated in this analysis is $15.55\,\mathrm{fb}^{-1}$ of integrated luminosity at this stage.

5.2.3 Luminosity Check-Up

The luminosity has been calculated with certified tools, based on all recorded lumisections covered by the SingleElectron datasets [44]. It acts as reference to weight the backgrounds to match the data yield. However, a Monte Carlo weighting based on this value of luminosity leads to a considerable difference in the shapes of background events and data. Figure 5.6 shows this effect for a data sample after all event selection steps.

The reason for this mismatch could not be figured out in detail. The integrals over the M_T and S_T distribution show a good agreement of the total MC and data event

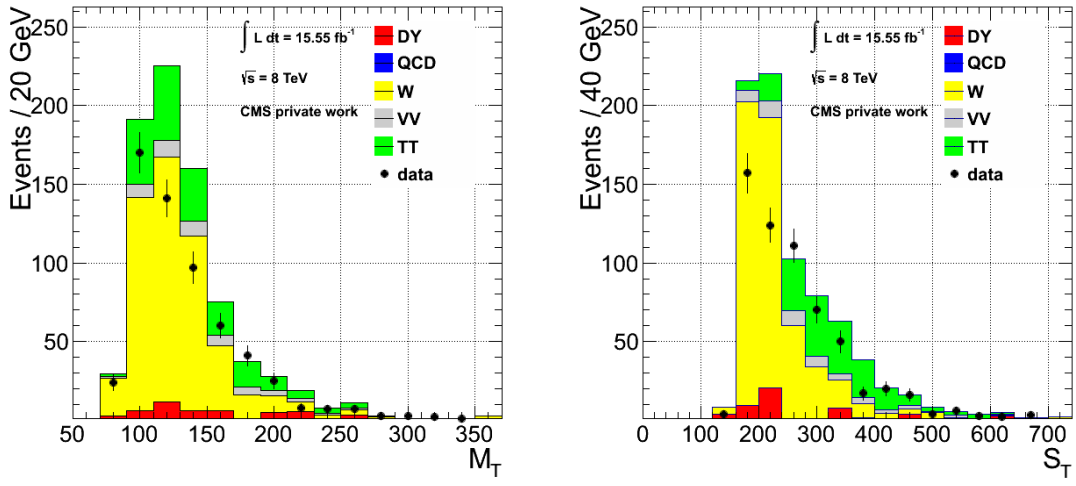

(a) (b)

Figure 5.6: Overestimation in peak regions of backgrounds in the M_T (a) and S_T (b) distribution using (N)NLO cross sections for MC and estimated luminosity.

yield. Nevertheless, there is a strong over-estimation in the peak regions and a under-estimation in the tails. This could be indicative that this concerns a systematic issue of MC event generation or an improper reconstructed pileup distribution.

To check whether this effect has its origin in a faulty analysis design, impacts of comparing the given data to a reference distribution are investigated. Therefore, a Z peak is examined. For the mass range from 60 to 120 GeV, an exact cross section $\sigma(pp \to ZX) \times \mathcal{B}(Z \to l^+l^-)$ measured in $\sqrt{s} = 8\,\text{TeV}$ data is available [45]. Events with exact 2 electrons obeying HEEP 4.1 requirements (see section 5.4 and Table 5.6) and no further GSF electron with $p_T \geq 15\,\text{GeV}$ are selected from the full SingleElectron dataset as well as from the used DY MC sample. The invariant ee mass has to be in the interval from 60 to 120 GeV. Figure 5.7 shows the result, where the MC background is weighted with the factor

$$w = \sigma \frac{L}{N} \tag{5.9}$$

with measured cross section σ, luminosity L and number of simulated events N. This sample show the same behaviour: The integrals yield consistent results, but the peak region is overestimated.

To allow a better illustration of the difference in the shapes, the MC is scaled down to match the maximum of the peak. This is done by fitting a Voigt profile

$$V(m, \sigma, \Gamma) = V_0 \cdot \int G(m', \sigma)\, L(m' - m, \Gamma)\, dm' \tag{5.10}$$

to both data and MC (Fig. 5.8). The scaling factor then is retrieved from the relation of the functions' maxima and is determined to be 0.908. This can be translated to a 'virtual' luminosity of $\int L\,dt = 14\,121.2\,\text{pb}^{-1}$, which has no physical meaning but serves as a modified parameter to be used in (5.9) for rescaling. The result in Fig. 5.9 clearly shows, that the peak's width is too narrow.

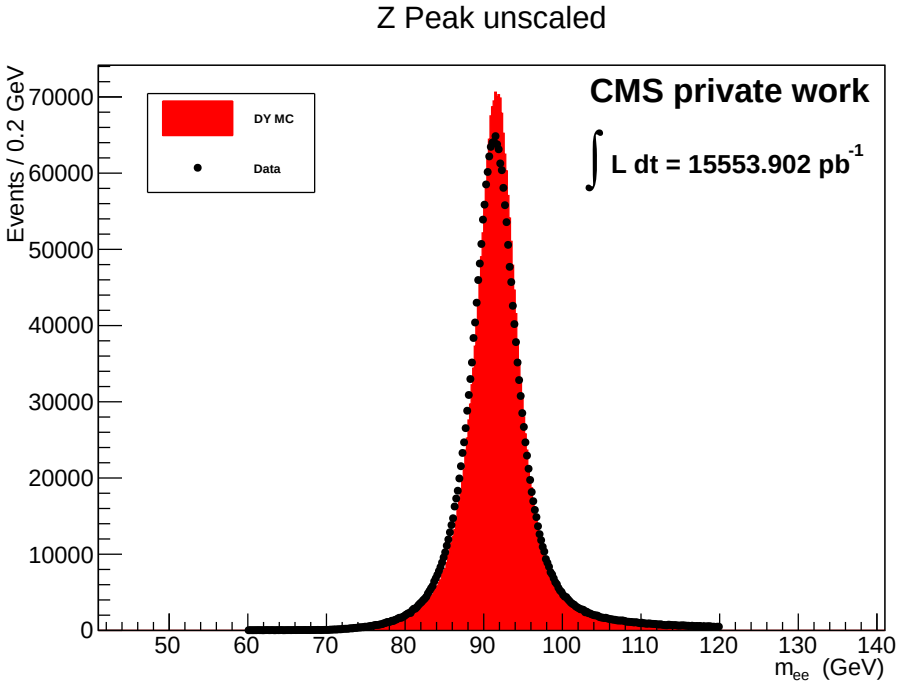

Figure 5.7: Z Peak from SingleElectron data and DY MC.

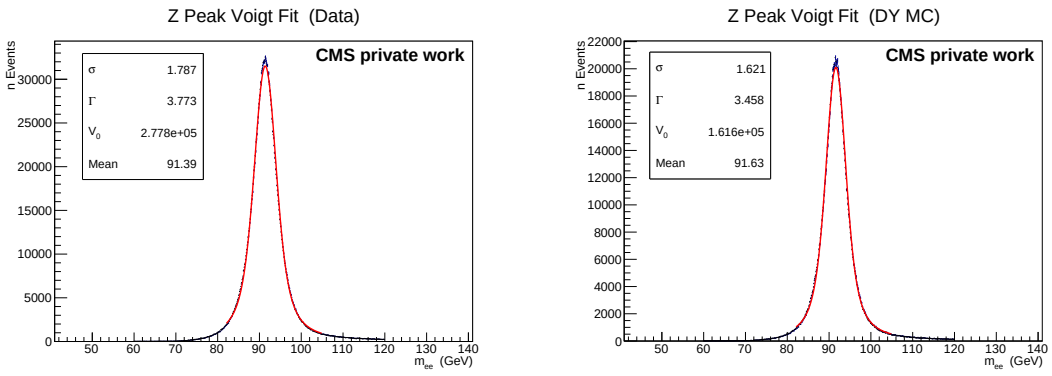

(a) (b)

Figure 5.8: Result of the Voigt fits to the Z peak in data (a) and MC (b).

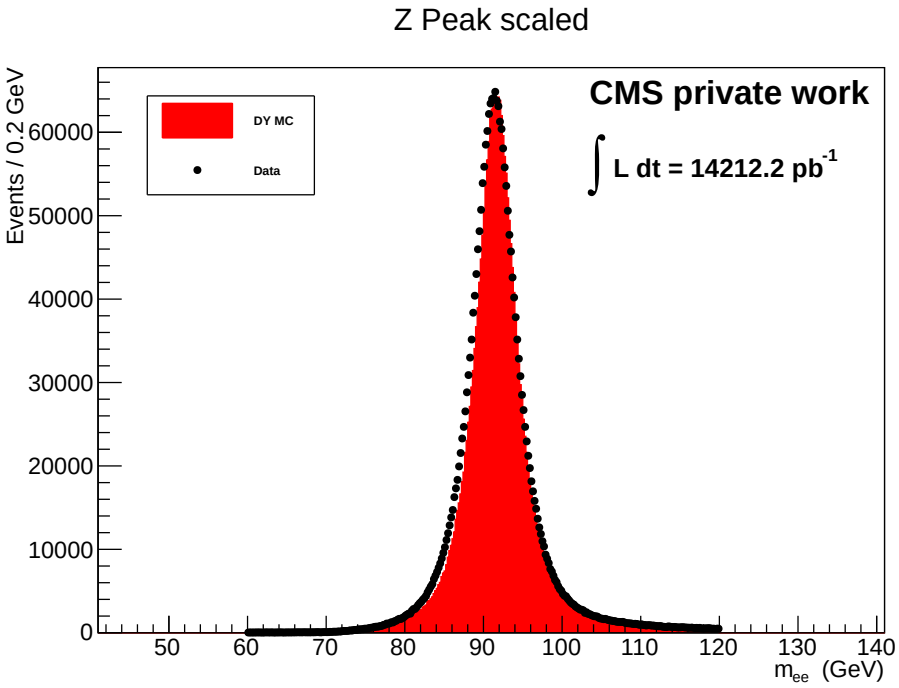

Figure 5.9: Z Peak with the MC maximum scaled down to fit data.

Further investigations show, that the intensity of this effect depend on the included dataset parts. To probe the influence of different pileup distributions on particular datasets could be worth a further effort. Unfortunately, the only way to handle this problem on a short time scale, is to take only those datasets into account, that proved to be reliable.

Hence, only the datasets A and C1 are taken into account for all further parts of the analysis. The corresponding luminosity is $1301.9\,\mathrm{pb}^{-1}$.

5.3 Background sample Preprocessing

Background samples are simulations based partly on general assumptions, which can only be estimates of real conditions since they are made a priori. These samples have to be matched to conditions encountered in a real experimental situation to achieve sufficient validity. Two of those adjustments are performed: *Pileup Reweighting* and *Jet Energy Scaling*.

5.3.1 Pileup Reweighting

In the LHC, particles are arranged in bunches, containing about 15×10^{10} protons each [6]. Two bunches meet at the interaction point, so that it is very likely that more than one proton pair is going to interact. Every bunch crossing leads to an average number of about 20 simultaneous interactions at the 2012 instantaneous luminosity of $\mathscr{L} \approx 7 \times 10^{33}\,\mathrm{cm}^{-1}\,\mathrm{s}^{-1}$. Each of these vertices is a source for decay products that are measured in the detector and pollute the signal originating in the *primary vertex*,

the source of the hardest process among all interactions. This phenomena is known as (in-time) *pile-up* (PU). The relative frequency of vertex numbers can only be estimated roughly in simulation processes since the simulation has to use a guessed vertex distribution. The distribution model used to simulate pileup in the applied Monte Carlo samples is the 'S10' scenario. To make a simulated dataset comparable to real data, it's pileup

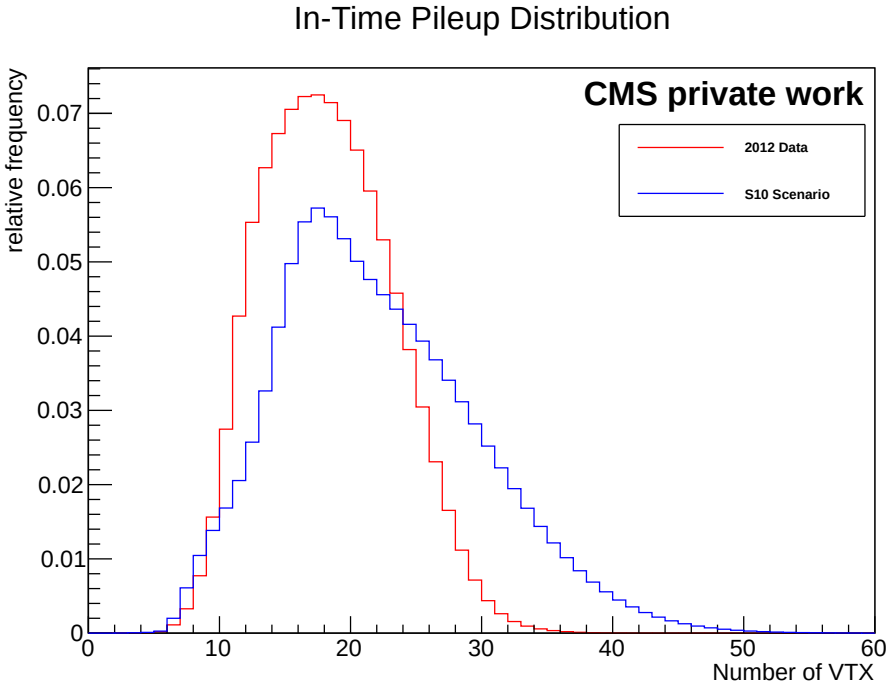

Figure 5.10: S10 pileup model compared to a measured distribution in 2012 data

distribution has to be reweighted to match the one measured in data. Fig. 5.10 shows both a measured and a modelled pileup distribution.

This correction procedure is called *pileup reweighting*. For each bin of the simulated distribution a correctional factor is calculated. This factor matches the bin content to the measured value. Now, for every MC event a *weight* can be determined by finding the factor correlating to the particular event's number of vertices. This weight has to be applied on all quantities of the MC event. Fig. 5.11 illustrates the effect of PU reweighting on the vertex distribution.

A bunch crossing happens every 50 ns. It is possible that this time is not sufficient to allow all particles to leave the detector before a subsequent event occurs. This overlap is denoted out-of-time pileup. As the time between two bunch crossings is higher than the deadtime of the inner tracker electronic devices, this effect is treated by the trigger system, which is able to correlate tracks to bunch numbers in most cases. Hence, the impact of this effect is negligibly.

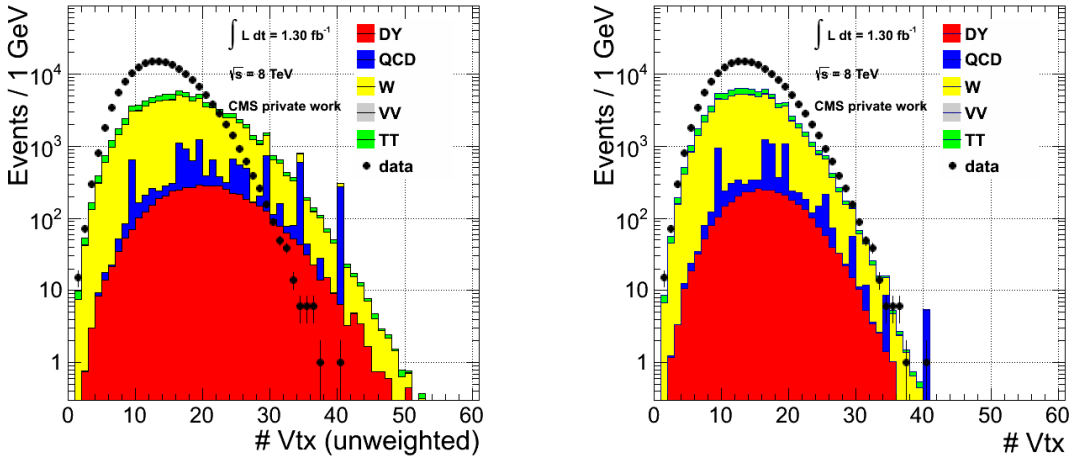

(a) (b)

Figure 5.11: Number of vertices before (a) and after (b) pileup reweighting. Since statistic is too low to illustrate shape issues after appliance of all event selection steps, the situation after electron ID (step 5) is shown.

5.3.2 Jet Energy Scaling

In Monte Carlo samples, the jet energy scale is a parameter in the detector simulation process. It is derived from the measured Jet Energy Resolution which lead to a location-dependent shift between true and measured energy scale. The resulting correction factor is implemented in the RECO stage of the simulation. However, this implementation has some systematic limitations in accuracy that lead to an improper jet energy scale and therefore to change in the width of an event's jet-p_T and $\not{E}_T$ distributions.

A correction of the energy scale can be achieved by comparing jet properties before detector simulation (GEN level) and afterwards (RECO level) [46]. Information in GEN level contain truth information. To correlate it with RECO jets, a correctional term, parametrised by a scaling factor f, can be attached to the RECO momentum:

$$\begin{aligned} p_T^{\text{truth}} &= p_T^{\text{reco}} + f \cdot p_T^{\text{reco}} \\ &= (1+f)\, p_T^{\text{reco}} \end{aligned} \tag{5.11}$$

The factor f is dependent of p_T and η. It is determined for the entire set of background datasets (Tab. 5.3). In each event, PF jets with $p_T > 15\,\text{GeV}$ are regarded. Each GEN jet is probed if a RECO jet exists within a cone of size $\Delta R = 0.5$. In this case the RECO jet is assumed to match the GEN jet. If more than one RECO jet is found in the GEN's neighbourhood, the one with the highest E_T is taken as match. Finally, the correction factor f can be calculated as:

$$f(p_T^{\text{reco}}, \eta) = \frac{p_T^{\text{truth}}(\eta)}{p_T^{\text{reco}}(\eta)} - 1. \tag{5.12}$$

Figure 5.12 shows the determined correction factor $f(p_T, \eta)$. For analysis, this factor

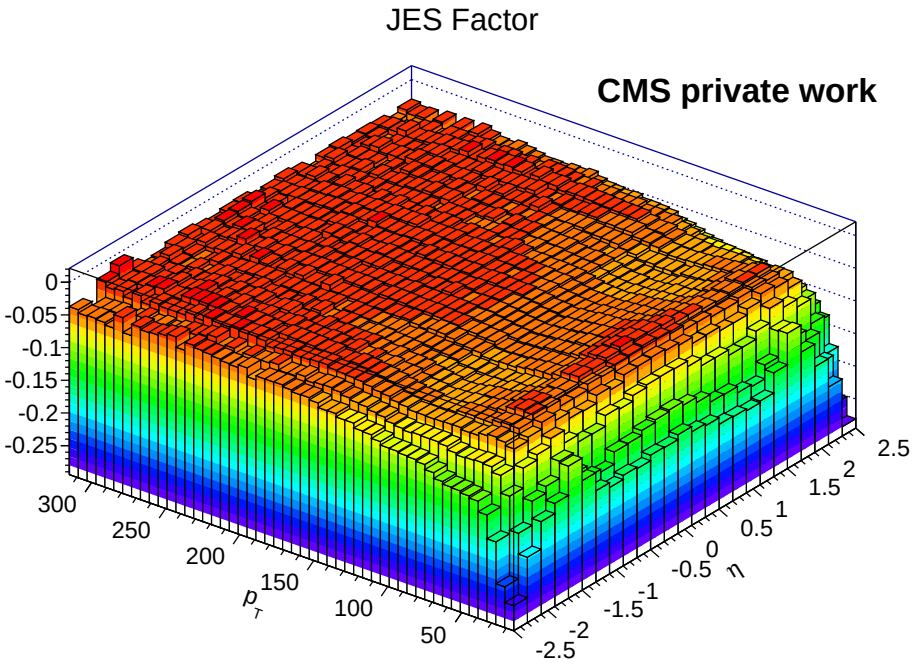

Figure 5.12: Jet energy scale correction factor $f(p_T, \eta)$ for RECO PF jets with $p_T > 15\,\text{GeV}$.

is applied on every PF jet with $p_T > 15\,\text{GeV}$ within any MC event. The particular correction (*smearing*) factor is taken from distribution (5.12) with respect to the jet's p_T and η. If the RECO jet can be successfully matched to a GEN one, this factor is used for correction:

$$\begin{aligned} p_i^{\text{PFjet}} &= (1+f)\, p_i^{\text{PFjet}}, \quad i \in \{x, y, z, T\} \\ \not{E}_T &= \not{E}_T - \sum_{\text{PFjets}} f \cdot p_T^{\text{PFJet}}. \end{aligned} \tag{5.13}$$

If no matching is possible, f has to be smeared first. Therefore, f is replaced by a random number out of a gaussian shape with mean f_{orig} (the initial value of f) and it's width $\sigma(f_{\text{orig}})$. Fig. 5.13 shows the $\not{E}_T$ distribution before and after Jet Scaling.

5.4 Event Selection

Events used for the final limit calculation need to be selected properly for several reasons. First of all, data and Monte Carlo samples must be selected by the same criteria. These must be able to ensure that all contained data arise from processes that are covered by the used Monte Carlo samples. Furthermore, the total background event yield has to be reduced to an irreducible minimum to maximise the signal yield's statistical dominance.

The selection is conducted in a cutflow of overall nine steps, containing several criteria each. Fig. 5.14 illustrates the effect on the event yield for any of those steps. A detailed listing is given in Table 5.5.

In detail, the cutstages are:

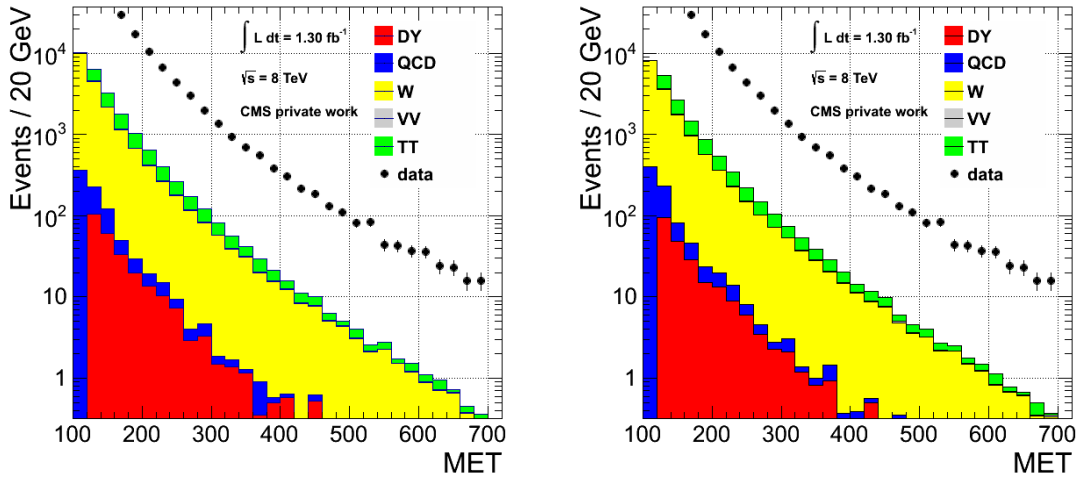

Figure 5.13: $\not{E}_T$ distribution before (a) and after (b) Jet Energy Scaling before event selection. Based on an inclusive set of background samples.

0. Noise Cleaning

   - ECAL noise
     Digitisation of ECAL entries needs a certain timespan, depending on the fraction of response times of single- to 5×5 crystal cluster entries. Simulations show, that energy deposits from prompt decays lead to a clear time signature (Fig. 5.15), as they have a straight trajectory and excite only a few crystals per cluster [47]. Therefore, they can be separated from noise by a time cut. The digitisation time $|\Delta T|$ is chosen to be to $< 3.5\,\text{ns}$.
   - MET
     The used MC datasets are selected to have a good resolution in the high energy region. For low energies, the covered regions differ from sample to sample. Including these regions into the analysis would blur all distributions. A common coverage of all datasets is achieved by claiming $\not{E}_T > 50\,\text{GeV}$.

1. Vertex Quality

   All vertices of an event are reconstructed in two steps [48]. The first step is the *vertex finding* to group all given tracks to clusters of trajectories with supposed common origin. Secondly, these tracks are analysed in the process of *vertex fitting*, where the vertex is finally reconstructed and its properties are made accessible for analysis. The number of vertices who pass a quality cut is counted. The selection criteria are:

   - The vertex has to be no fake, *i.e.* a vertex that passed the 'finding' but not the 'fitting' stage.
   - `ndof` > 4, where `ndof` indicates the track weight.
   - Distance from coordinate origin in z-direction: $|z| < 24\,\text{cm}$
   - Radial distance from z-axis: $\rho < 2\,\text{cm}$

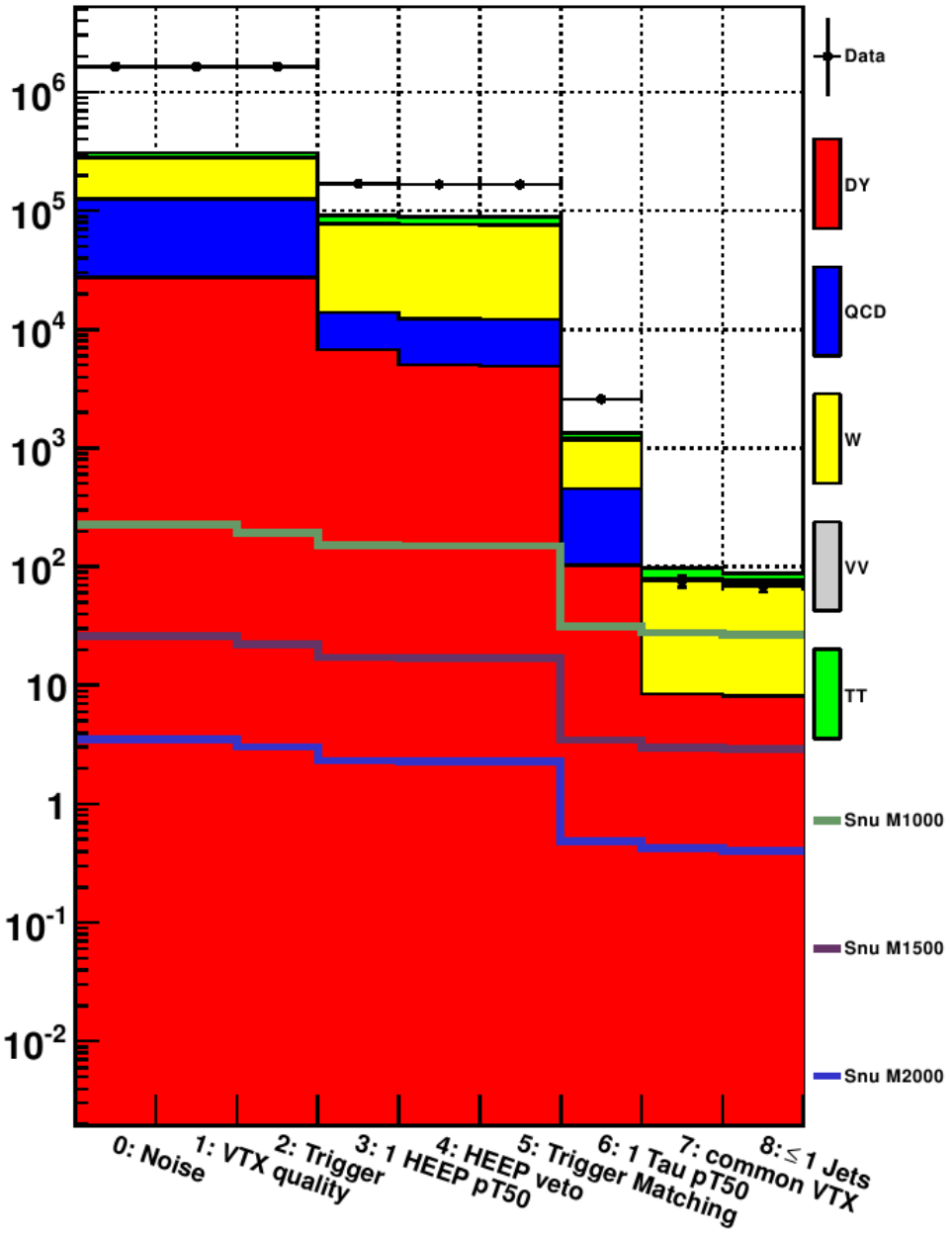

Figure 5.14: Event selection cutflow showing the number of data-, background-, and signal events after application of specific cuts denoted by the bin labels.

Cut	Data	DY	QCD	W	VV	$t\bar{t}$	$\tilde{\nu}_\tau$ 1.0 TeV	$\tilde{\nu}_\tau$ 1.5 TeV	$\tilde{\nu}_\tau$ 2.0 TeV
0: Noise	1 646 192	$17\,796.95 \pm 55.56$	$72\,441.49 \pm 4114.71$	$151\,157.95 \pm 73.34$	1220.51 ± 2.24	$24\,723.48 \pm 41.53$	226.12 ± 2.81	25.77 ± 0.31	3.53 ± 0.04
1: VTX qlty.	1 641 379	$17\,752.38 \pm 55.49$	$72\,440.18 \pm 4114.71$	$151\,127.39 \pm 73.33$	1217.64 ± 2.23	$24\,720.17 \pm 41.52$	225.44 ± 2.80	25.69 ± 0.31	3.51 ± 0.04
2: Trigger	1 641 379	$17\,752.38 \pm 55.49$	$72\,440.18 \pm 4114.71$	$151\,127.39 \pm 73.33$	1217.64 ± 2.23	$24\,720.17 \pm 41.52$	195.58 ± 2.61	22.35 ± 0.29	3.02 ± 0.04
3: Ele ID	168 922	4337.05 ± 27.52	4860.87 ± 1045.33	$59\,631.21 \pm 45.79$	601.02 ± 1.57	$12\,037.06 \pm 28.95$	152.24 ± 2.31	17.12 ± 0.25	2.31 ± 0.03
4: Ele veto	167 240	3383.27 ± 24.49	4860.87 ± 1045.33	$59\,622.63 \pm 45.79$	554.50 ± 1.52	$11\,763.05 \pm 28.62$	150.34 ± 2.29	16.88 ± 0.25	2.29 ± 0.03
5: TrigMatch	167 084	3315.34 ± 24.26	4860.29 ± 1045.33	$59\,615.15 \pm 45.79$	550.76 ± 1.52	$11\,742.63 \pm 28.59$	149.42 ± 2.29	16.87 ± 0.25	2.28 ± 0.03
6: Tau ID	2607	71.98 ± 3.61	512.32 ± 440.61	618.83 ± 4.60	12.57 ± 0.22	142.85 ± 3.14	31.47 ± 1.05	3.44 ± 0.11	0.49 ± 0.02
7: pr. VTX	76	7.19 ± 1.20	0.00 ± 0.00	64.40 ± 1.52	3.58 ± 0.12	18.82 ± 1.15	27.37 ± 0.98	2.97 ± 0.11	0.43 ± 0.01
8: ≤ 1 Jets	69	7.00 ± 1.19	0.00 ± 0.00	63.54 ± 1.51	3.37 ± 0.12	9.82 ± 0.84	26.57 ± 0.96	2.87 ± 0.10	0.40 ± 0.01

Table 5.5: Event yields after application of selection steps denoted in column 'Cut'.

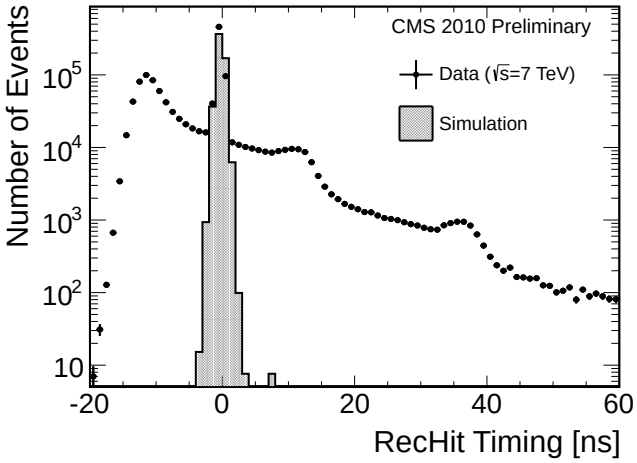

Figure 5.15: ECAL digitalisation time. T_0 is the time of final ECAL response inter-calibrated to time of bunch crossing. Taken from [47].

The event must have at least one certified vertex. In case of multiple vertices, the primary vertex, *i.e.* the vertex with the highest combined p_T of all associated particles, must have passed this certification.

2. Trigger

   Accepted events must have been selected by the high level single-electron trigger `HLT_Ele27_WP80`. For this, an electron must have a $p_T > 27\,\text{GeV}$ and satisfy the WP80 selection criteria on trigger level. WP80 denotes a working point originally developed to detect electrons from W decays with an efficiency of 80%. This trigger had no prescale.

3. Electron ID

   Exactly one electron with $p_T > 50\,\text{GeV}$ matching the HEEP 4.1 (*High Energy Electron Positron*) [49] selection is required. Table 5.6 lists all selection criteria in detail. The variables used by HEEP are:

   - `ECAL driven` indicates, that the electron fulfils the requirement to be theoretically reconstructable from ECAL seeded algorithms. Otherwise, the GSF algorithm could run without ECAL data and lead to badly reconstructed tracks.
   - $|\Delta\eta_{in}|$, $|\Delta\phi_{in}|$
     The difference between the track direction measured at the innermost tracker layer, extrapolated to the primary vertex and the position measured in the ECAL supercluster.
   - H/E
     The ratio of HCAL and ECAL energy deposits within a cone $\Delta R = 0.15$ around the electron's track.

Variable	Barrel	Endcap
	$\lvert\eta\rvert < 1.442$	$1.56 < \lvert\eta\rvert < 2.5$
E_T	$> 35\,\text{GeV}$	$> 35\,\text{GeV}$
ECAL driven	true	true
$\lvert\Delta\eta_{in}\rvert$	< 0.005	< 0.007
$\lvert\Delta\phi_{in}\rvert$	< 0.06	< 0.06
H/E	< 0.05	< 0.05
$\sigma_{i\eta i\eta}$	—	< 0.03
$E^{2\times5}/E^{5\times5}$	> 0.94	—
ECAL+HCAL Iso	$< 2\,\text{GeV} + 0.03E_T + 0.28\rho$	$< 2.5\,\text{GeV} + 0.03(E_T - 50\,\text{GeV})$ $+0.28\rho$
Track ISO	$< 5\,\text{GeV}$	$< 5\,\text{GeV}$
Lost Hits	≤ 1	≤ 1
$\lvert d_{xy}\rvert$	$< 0.02\,\text{cm}$	$< 0.05\,\text{cm}$

Table 5.6: HEEP 4.1 Electron ID criteria. For barrel and endcap regions, different thresholds are applied. ρ denotes a measure for an energy contribution induced by pileup.

- $\sigma_{i\eta i\eta}$
  A measure of the electron's energy spread in η in a 5×5 ECAL crystal block placed around the initially seeded crystal.
- $E^{2\times5}/E^{5\times5}$
  Fraction of energy deposits in different seeded ECAL clusters.
- ECAL, HCAL, track isolation
  Energy and p_T in a cone $\Delta R < 0.3$ around the track that can't be assigned to the reconstructed electron.
- $|d_{xy}|$
  The impact parameter in the xy-plane with respect to the primary vertex.

4. Electron Veto

   No other electron than the selected one may pass the standard HEEP ($p_T > 35\,\text{GeV}$) selection.

5. Trigger Object Matching

   The selected electron has to be the one that released the HLT trigger.

6. Tau ID

   At least one hadronic τ, reconstructed by the HPS algorithm, must be identified by satisfying following criteria [50]:

   - $p_T > 50\,\text{GeV}$

- $|\eta| < 2.3$
- At least 1 charged PF hadron candidate must be contained in the τ-jet
- The exact decay mode has to be reconstructed: $\tau \to n\pi^{\pm} + m\pi^0$ with $n \in \{1, 3\}$, $m \in \{0, 1, 2\}$ (compare Table 5.1).
- Need to pass `byTightCombinedIsolationDeltaBetaCorr` discriminator: The reconstructed τ has to be isolated within a cone of $\Delta R = 0.5$. Neutral components as π^0 and γ originating from pileup may have entered the HPS cone. As they cannot be rejected by tracking information, they may have mistakenly be included in the reconstruction. The number of such fake contributions is reduced by the *Delta-Beta Correction* based on the isolation

$$\mathrm{Iso}_{\Delta\beta} = \frac{p_T^{\mathrm{total}}(\pi^{\pm}) + p_T^{\mathrm{total}}(\pi^0) + p_T^{\mathrm{total}}(\gamma) - 0.5\, p_T^{\mathrm{total}}(\pi^{\pm}_{\mathrm{pileup}})}{p_T^{\tau}}. \tag{5.14}$$

  For working point 'tight', this has to be < 0.8.
- Need to pass `againstElectronTight` discriminator: This is based on an electron-pion MVA discriminator, which has to be < -0.1. The track has to be outside of the transition zone $1.4442 < |\eta| < 1.566$ from barrel to endcap (compare Table 5.6).
- Need to pass `againstMuonLoose` discriminator: The extrapolation of the τ track must not match measured μ-chamber entries.

If more than one τ is found, the one with the highest p_T is selected.

7. Origin in primary vertex

   The electron is matched to the vertex using the impact parameters in xy- and z dimension. As τ track reconstruction is too unprecise to allow matching to a certain vertex, the τ and e are tested to be paired with the help of angular and momentum correlations. The $\tilde{\nu}_{\tau}$ decay is assumed to produce this pair as final particles only. Ideally, both have the same p_T and $\Delta\phi$ is π. To make both e- and τ p_T comparable, all $\not{E}_T$ is assumed to belong to the τ-decay. The relevant p_T^{τ} is the one, that results from summing the Lorentz vectors $\vec{p}_T$ and $\vec{\not{E}}_T$. This leads to the ratio

$$R_{e\tau} = \frac{(\vec{p}_T^{\,\tau} + \vec{\not{E}}_T)_T}{p_T^e} \tag{5.15}$$

   as shown in (Fig. 5.16).

   The applied requirements are:

   - $|d_z| < 0.2\,\mathrm{cm}$
   - $|d_{xy}| < 0.02\,\mathrm{cm}$
   - $\Delta\phi > 2$
   - $0.6 < R_{e\tau} < 1.2$

8. Maximally 1 PF jet

   Jets have to be isolated by $\Delta R = 0.4$ from the selected e and τ and have furthermore to match the recommendation for 'loose' jet selection criteria to reject fake jets [51]:

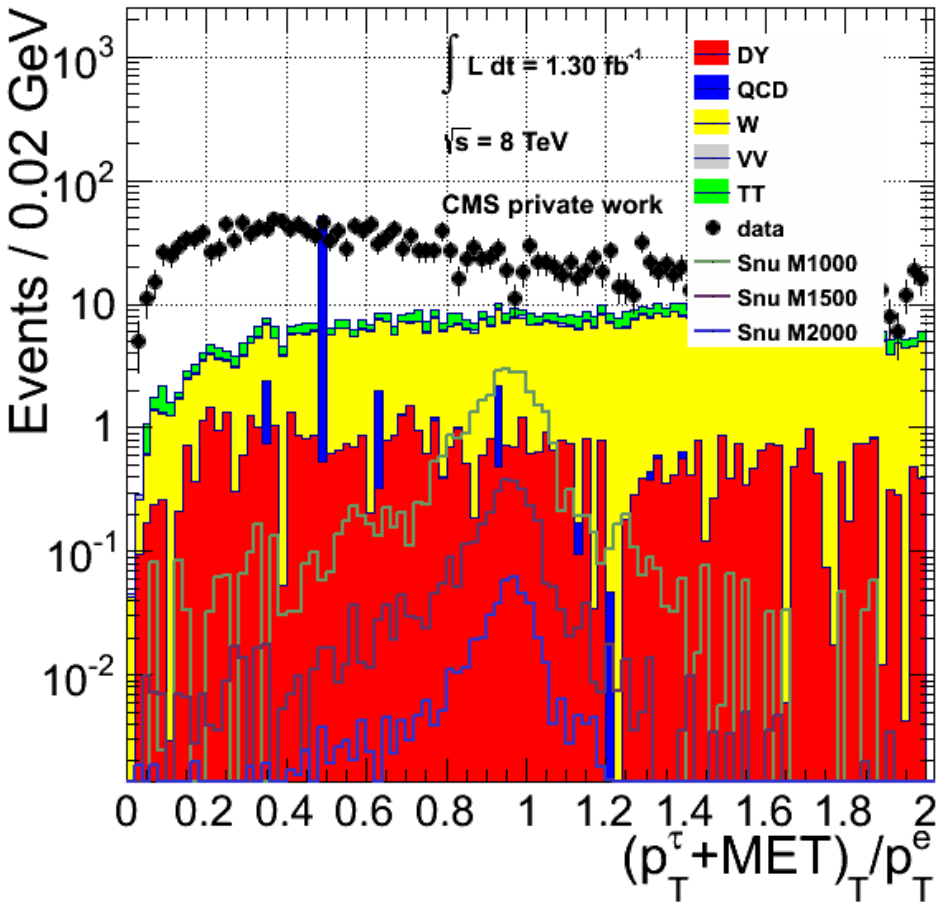

Figure 5.16: Ratio $(\vec{p}_T^{\,\tau} + \vec{\not{E}}_T)_T/p_T^e$ after selection step 6 (particle ID). The discrepancy between data and MC disappears in the following 'common vertex' stage, which include a cut on the present ratio.

$\lambda_{313}, \lambda'_{311}$	0.05	0.1	0.5
mass points	20	7	3
mass range (TeV)	0.1..2.0	0.5..2.6	2.6..3.0

Table 5.7: Overview of simulated signal points and ranges

- $p_T > 40\,\text{GeV}$
- $|\eta| < 2.4$
- Neutral hadron fraction < 0.99
- Neutral EM fraction < 0.99
- Charged EM fraction < 0.99
- Number of constituents > 1
- Charged hadron fraction > 0
- Charged multiplicity > 0

5.5 Signal Samples

The signal samples have been produced with the help of the HEPMDB framework [52]. This provides a huge database of models for different SM and BSM scenarios and the corresponding signatures. It combines a large collection of tools, including Matrix Element generators, to a highly customisable event generator. All calculations can run on a high performance HEPMDB computing infrastructure.

The first production step is the generation of the SUSY mass spectrum, performed by the SoftSusy package [53]. Based on this, the participating processes, decay widths and LO cross sections of the hard interaction are calculated by the generator CalcHEP [54]. Finally, the event is produced, and all relevant information is stored in the exchangeable *Les Houches Event* (LHE) data format [55] and provided for download.

These LHE events are used as input file for further official CMS Monte Carlo production with Pythia6 [41] shower generation embedded in the CMSSW framework. The final signal sample is stored in AODSIM format at a T2 node within the LHCG.

The used sample contains a complete mass scan covering events for multiple $\tilde{\nu}_\tau$ mass points, produced under assumption of several different λ and λ' values. Within this inclusive sample, only events with $\lambda_{313} = \lambda'_{311} = 0.05, 0.1$ or 0.5 are selected.

Fig. 5.17 shows an overview over mass ranges and number of generated signal events for selected coupling constants. The $\tilde{\nu}_\tau$-mass is constructed from the invariant mass of the initial $d\bar{d}$-pair at GEN level. Table 5.7 shows a numerical synopsis.

Some of the most relevant properties of the signal are depicted in (Fig. 5.18). All distributions are created at RECO level after the Object ID step in the event selection chain (stage 6 in the analysis cutflow, compare section 5.4). To grant comparability, only samples with $\lambda = \lambda' = 0.1$ are used and all plots are displayed normalised.

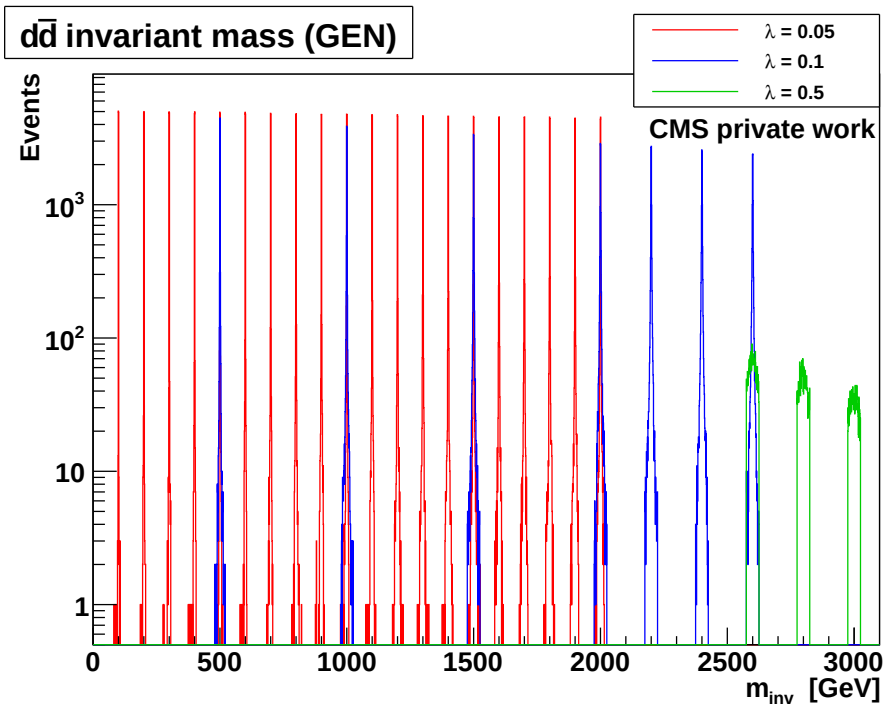

Figure 5.17: The inclusive signal sample covering several λ, λ' and $m_{\tilde{\nu}_\tau}$ values.

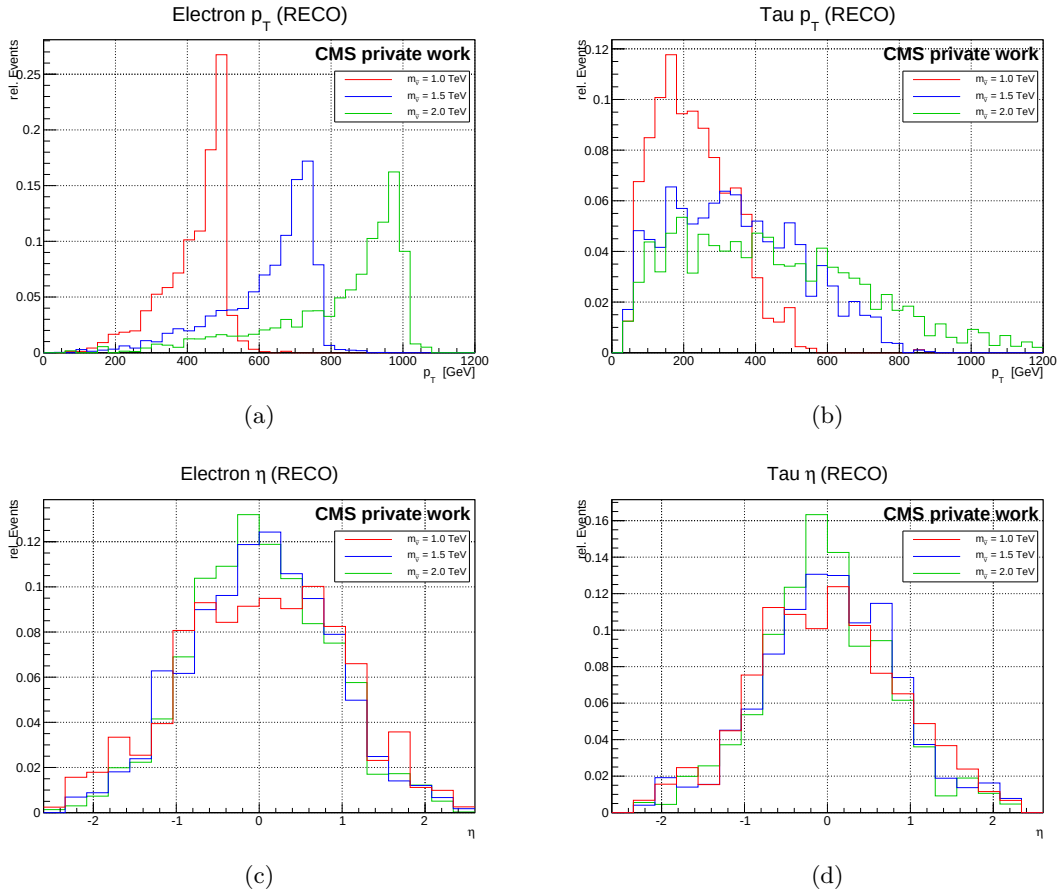

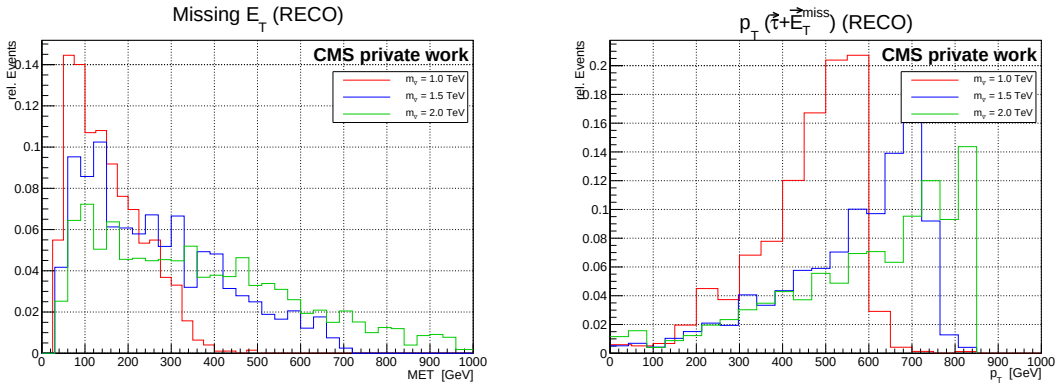

(e)

(f)

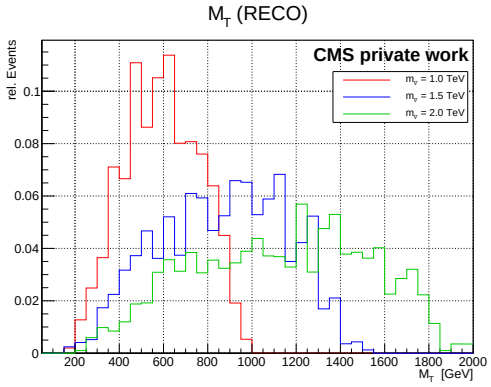

(g)

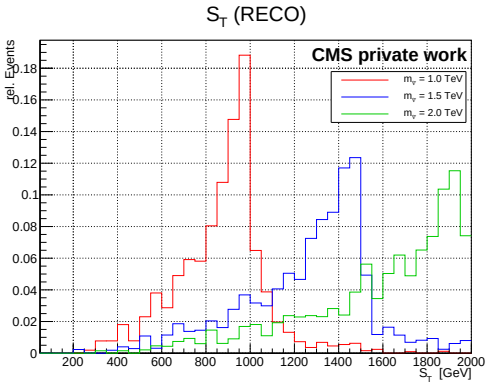

(h)

Figure 5.18: Relevant distributions of signal samples with $\lambda = \lambda' = 0.1$ for $m_{\tilde{\nu}_\tau} = 1.0\,\text{TeV}$, $1.5\,\text{TeV}$ and $2\,\text{TeV}$.

Resonant production of the $\tilde{\nu}_\tau$ and the quasi instantaneous decay take place within a small width around the resonance mean. The decay widths depend on the coupling and the $\tilde{\nu}_\tau$-mass only [20]:

$$\begin{aligned} \Gamma_{\mathrm{p}}(\tilde{\nu}_\tau \to d\bar{d}) &= 3\,(\lambda')^2\,\frac{m_{\tilde{\nu}_\tau}}{16\pi} \\ \Gamma_{\mathrm{d}}(\tilde{\nu}_\tau \to e\tau) &= 2\lambda^2\frac{m_{\tilde{\nu}_\tau}}{16\pi} \\ \Gamma_{\mathrm{tot}} = \Gamma_{\mathrm{p}} + \Gamma_{\mathrm{d}} &= \left(3\lambda'^2 + 2\lambda^2\right)\frac{m_{\tilde{\nu}_\tau}}{16\pi} \end{aligned} \tag{5.16}$$

For an energy exchange via the s-channel in a narrow environment around the particle mass, the process' cross section is well approximated by the Breit-Wigner formula [56]:

$$\sigma(d\bar{d} \to \tilde{\nu}_\tau \to e\tau) = \frac{4\pi s}{m^2_{\tilde{\nu}_\tau}}\,\frac{\Gamma(\tilde{\nu}_\tau \to d\bar{d})\cdot\Gamma(\tilde{\nu}_\tau \to e\tau)}{(s - m^2_{\tilde{\nu}_\tau})^2 + m^2_{\tilde{\nu}_\tau}\Gamma^2_{\mathrm{tot}}} \tag{5.17}$$

The cross section depends strongly on the couplings, as shown in (Fig. 5.19) exemplarily for a 1.5 TeV $\tilde{\nu}_\tau$.

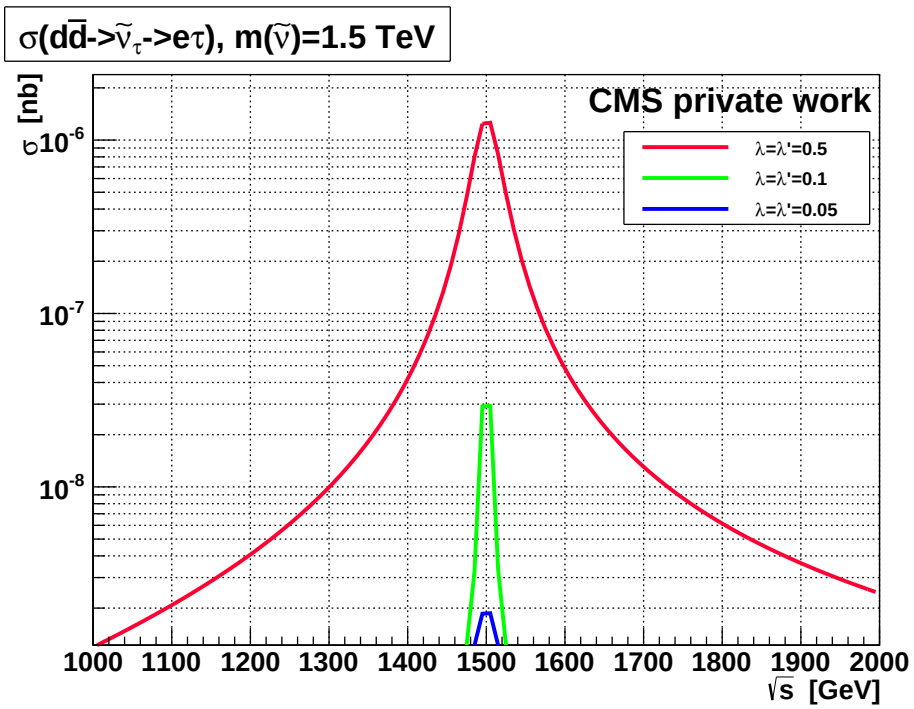

Figure 5.19: Cross section for the resonant process $d\bar{d} \to \tilde{\nu}_\tau \to e\tau$ with $m_{\tilde{\nu}_\tau} = 1.5\,\mathrm{TeV}$ and $\lambda = \lambda' = 0.05, 0.1$ and 0.5.

For further analysis, it is essential to use a cross section that is in accordance with the actual initial state given by the experiment. Hence, such a one is calculated for LHC conditions with pp collisions at $\sqrt{s} = 8\,\mathrm{TeV}$ up to NLO precision, along with the corresponding k factor for signal scaling [57]. The calculation includes higher order SUSY- and SM QCD corrections including vertex enhancements, radiative corrections and quark self energy contributions arising from correlations between q- and $\tilde{q}$-fields.

Fig. 5.20 shows the resulting cross section as a function of the $\tilde{\nu}_\tau$-mass for $\lambda = \lambda' = 0.05, 0.1$ and 0.5.

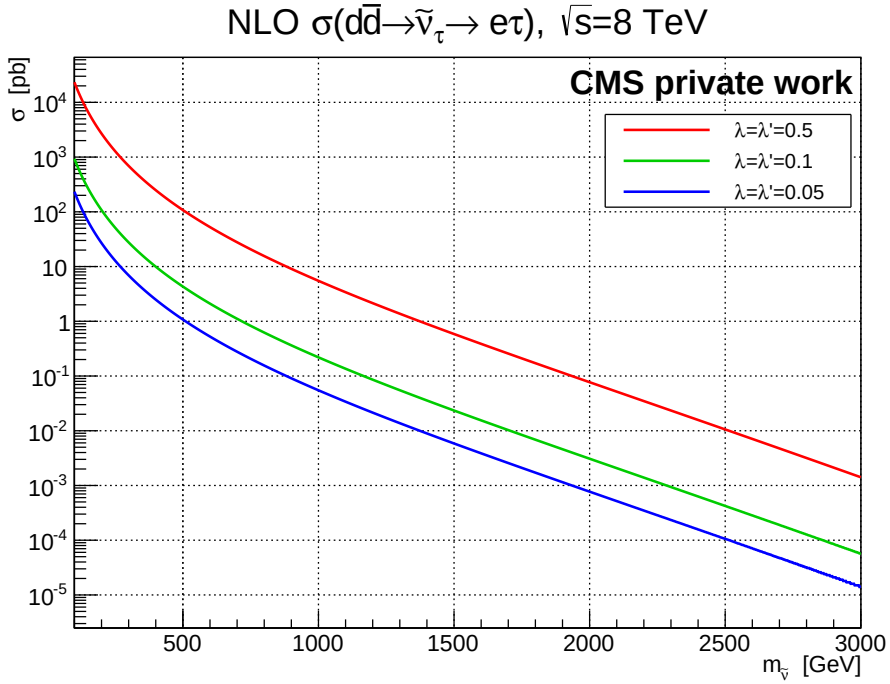

Figure 5.20: Theoretical NLO cross section for the process $d\bar{d} \to \tilde{\nu}_\tau \to e\tau$ for pp collisions at $\sqrt{s} = 8\,\text{TeV}$.

5.6 Background Scaling

The methodology of searching new phenomena in experimental data is to compare measurements with predictions of established theories. In particle physics, both are given in shapes that indicate the event numbers for concrete values of a certain characteristic. Practically this means, that event yields of observables are histogrammed in intervals of values of this observable (*bins*).

For data, the bin contents are given by counting experiments. Backgrounds are modelled by a certain number of simulated events. Hence, this sample reproduces the correct shape of the considered background process but not the total event yield as expected from measured data. To match the Monte Carlo to the data yield, each MC bin has to be normalized to the event number and scaled to the expected luminosity by introducing a weight factor

$$w = f \cdot \frac{\sigma \cdot L}{N} \tag{5.18}$$

where σ denotes the simulated process' cross section, N the number of the simulated events and L the integrated luminosity. The factor f is an optional correctional factor to implement additional scaling requirements. Often Monte Carlo generators calculate leading order (LO) cross sections for the the signal only. So, the k-factor is usually used to scale the weight to higher order cross sections as second- (NLO) or third order

Drell-Yan	W	$t\bar{t}$
Max. 1 Jet	Exactly 1 Jet	Min. 1 Jet
$d_z(e_1) < 0.2\,\text{cm}$	$\sum p_t^{\text{jet}} > 110\,\text{GeV}$	$\sum p_t^{\text{jet}} > 90\,\text{GeV}$
$d_z(e_2) < 0.2\,\text{cm}$	$\Delta\phi < 1.9$	$\Delta\phi > 1$
$\not{E}_T < 75\,\text{GeV}$	$\not{E}_T > 80\,\text{GeV}$	$\not{E}_T > 80\,\text{GeV}$

Table 5.8: Cutflows to isolate Drell-Yan, W and $t\bar{t}$ events. For an explanation of the variables see section 5.4.

(NNLO) in perturbation theory.

Since they can be as large as 2,the determination of k-factors is mandatory. Calculation of NLO or NNLO cross sections is a sophisticated process, that has been performed by the CMS collaboration for a set of different processes [58]. To calculate the k-factor, the calculated $\sigma_{(\text{N})\text{NLO}}$ have to compared to a σ_{LO} from a simulation, that used exactly the same frontier conditions.

However, the conditions of the simulations used for k-factor estimation differ from them applied at the generation of the datasets used in the analysis. Thus, the k-factors for several samples are estimated very inaccurately and do not lead to a suitable scaling of the MC background.

For the main backgrounds Drell-Yan, W and $t\bar{t}$, the k-factor is estimated with a data driven method. For this, special cutflows are applied, that isolate events from the studied process. The isolation is based on the the two highest p_T standard GSF electrons. All selection criteria are listed in detail in Table 5.8. For the WW background, a conventionally estimated k is used. Contributions from WZ and ZZ are negligible and no k factor is applied.

The numerical estimation is performed by iterating k from 0.8 to 2.4 with a step size of 0.001. For each k, the background is scaled and the event yield is counted binwise. The k leading to the smallest χ^2, with

$$\chi^2 = \sum_{\text{bins}} \frac{(N_{\text{MC}} - N_{\text{data}})^2}{N_{\text{MC}}} \tag{5.19}$$

is taken. This is done for either the M_T and S_T distribution (Fig. 5.21). The final k factor is chosen as the average of these both.

Figures (5.22) show the DY, W, and $t\bar{t}$ distributions after scaling. The estimated k factors are listed in Table 5.9. Figure 5.23 shows the M_T and S_T distributions after all event selection steps scaled with initial LO cross sections and after applying the k-factors.

5.7 Data Driven Background Estimation

The expected background is modelled by simulations as precisely as possible. Nevertheless, in high energy signal regions, the statistics is insufficient to grant a reliable event

	DY	W	$t\bar{t}$	WW	WZ	ZZ	QCD
k (conventional)	1.188	1.321	1.717	1.151	—	—	—
k (M_T)	1.197	1.147	2.073	—	—	—	—
k (S_T)	1.195	1.144	2.018	—	—	—	—
k (average)	1.196 $\pm$ 0.001	1.146 $\pm$ 0.002	2.046 $\pm$ 0.028	—	—	—	—
k (applied)	1.196	1.146	2.046	1.151	1.0	1.0	1.0

Table 5.9: Applied k factors for all background scenarios. Rows M_T, S_T and 'average' show the results of the numerical estimation.

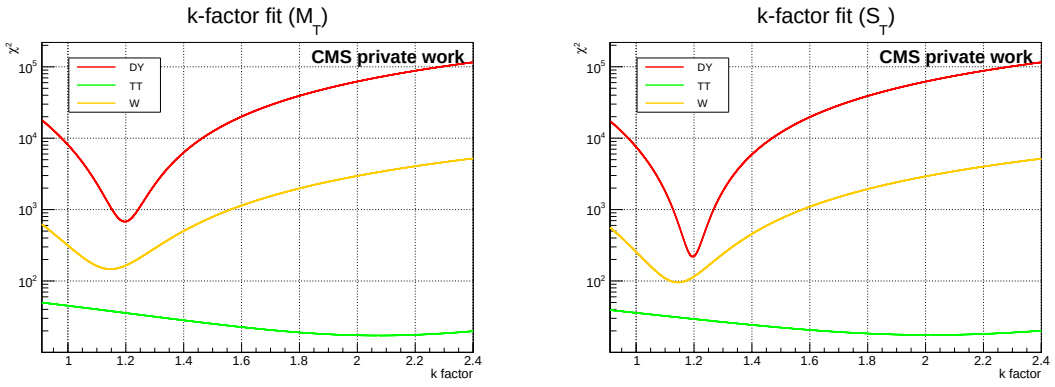

(a) (b)

Figure 5.21: Result of k-factor χ^2 fits to scale the M_T (a) and S_T (b) distributions of DY, W and $t\bar{t}$ MCs to data.

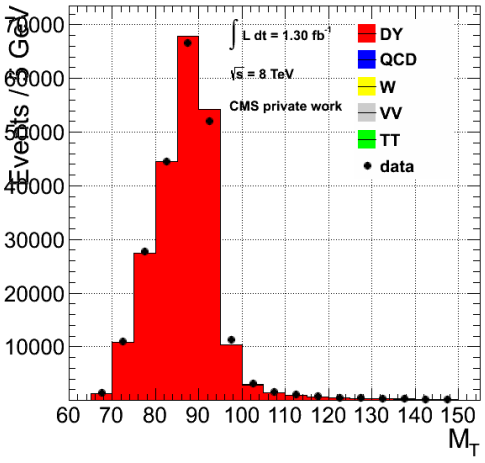

(a) Drell Yan (M_T)

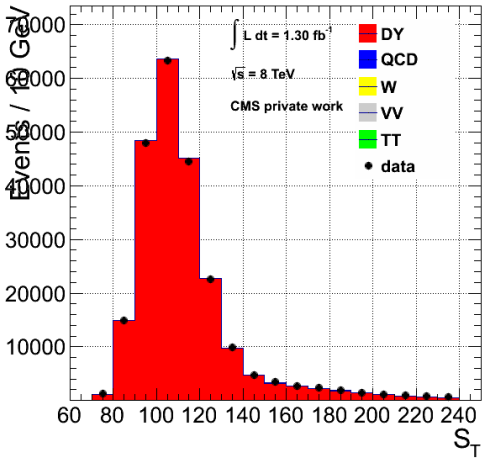

(b) Drell Yan (S_T)

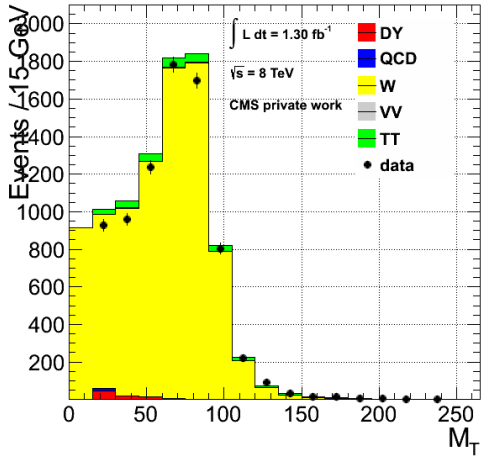

(c) W (M_T)

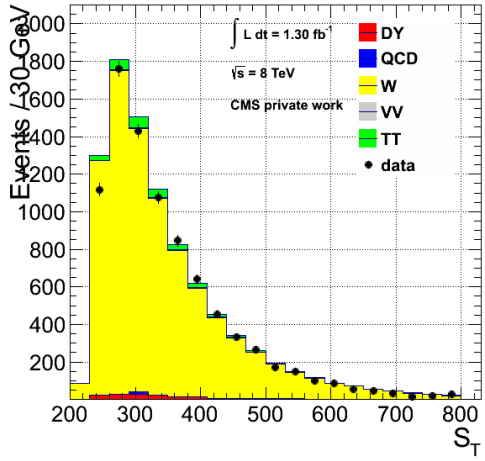

(d) W (S_T)

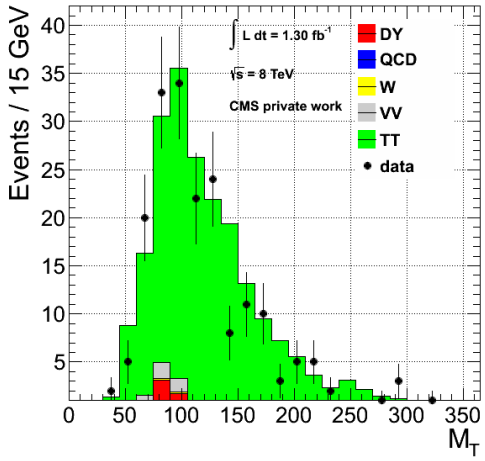

(e) $t\bar{t}$ (M_T)

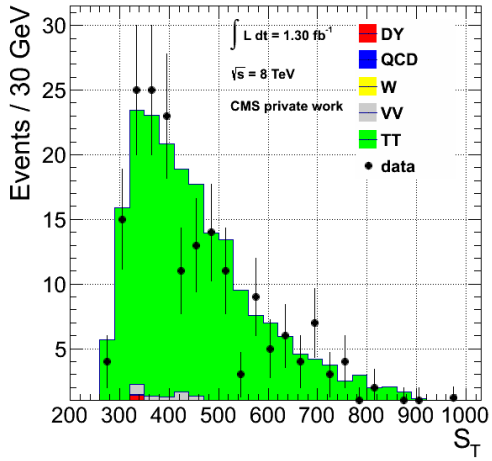

(f) $t\bar{t}$ (S_T)

Figure 5.22: Isolated main background samples after scaling.

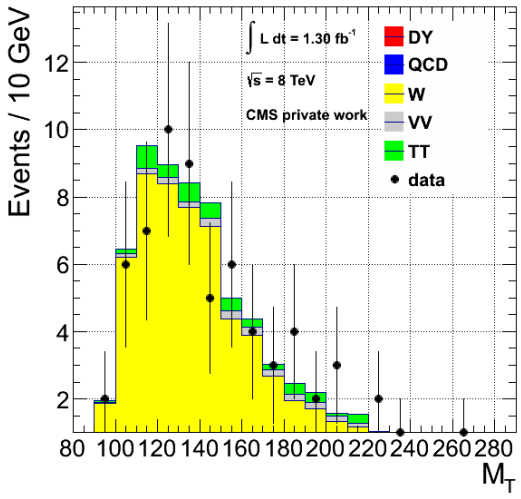

(a) M_T LO

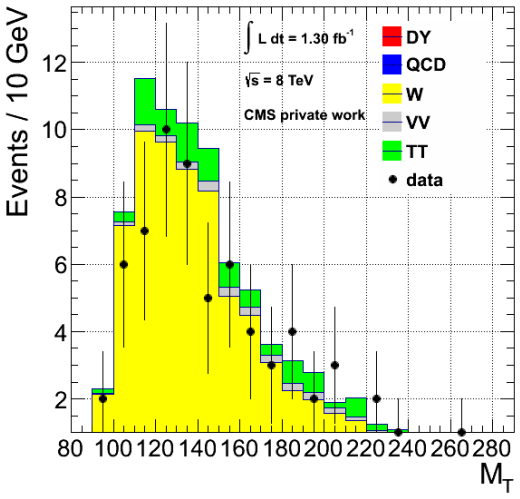

(b) M_T weighted

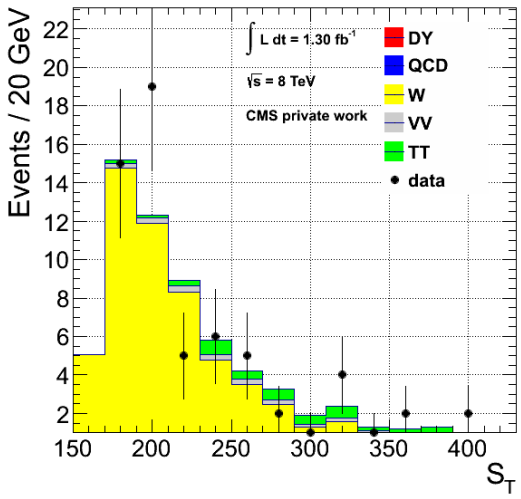

(c) S_T LO

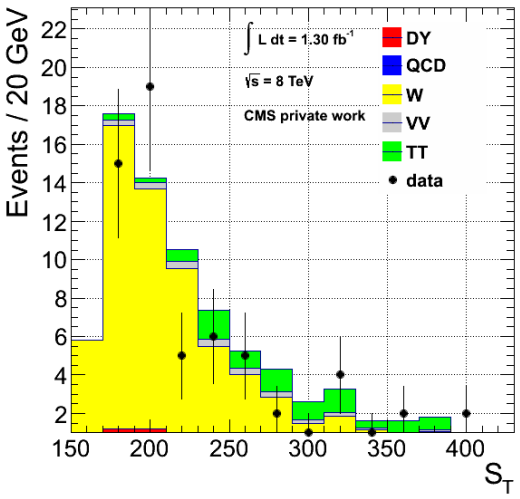

(d) S_T weighted

Figure 5.23: M_T and S_T distributions after all event selection steps with LO (a,c) and scaled (b,d) cross sections.

yield. Therefore, the background is estimated with the help of the *Tiles Method*, an inclusive data driven approach.

5.7.1 The Tiles Method

To be as independent from particular MC samples as possible, the Standard Model background estimation is determined using the 2×2 *Tiles Method* [59]. This technique has been originally developed for SUSY analyses with leptons and $\not{E}_T$ in the final state and thus, it can be applied to the signature present in this analysis.

The method derives the inclusive SM background and the number of signal events from data by exploiting various dependencies in MC data.

All data is processed on the basis of a set of two discriminating variables with good separation power. These variables should be as mutually independent as possible. The 2-dimensional variable space is segmented into four quadrants (*tiles*) A,B,C and D. For any of these segments, an equation balancing the numbers of data, background and signal can be set up. In general, this segmentation is arbitrary. The only requirement is to have sufficient statistics of both data and MC in each tile. This leads to a system of four independent linear equations:

$$\begin{aligned} N_A &= f_A^{\mathrm{SM}} N^{\mathrm{SM}} + f_A^{\mathrm{S}} N^{\mathrm{S}} & N_B &= f_B^{\mathrm{SM}} N^{\mathrm{SM}} + f_B^{\mathrm{S}} N^{\mathrm{S}} \\ N_C &= f_C^{\mathrm{SM}} N^{\mathrm{SM}} + f_C^{\mathrm{S}} N^{\mathrm{S}} & N_D &= f_D^{\mathrm{SM}} N^{\mathrm{SM}} + f_D^{\mathrm{S}} N^{\mathrm{S}} \end{aligned} \tag{5.20}$$

with N_i denoting the number of data events in tile i, N^{SM}, N^{S} the overall SM background- and signal event number and the fractions f_i^{SM}, f_i^{S} of SM and signal events in the corresponding quadrant. The fractions f^{SM} can be derived from the Monte Carlo samples. Assuming the independence of the signal variables, the signal fractions can be written as

$$\begin{aligned} f_A^{\mathrm{S}} &= \left(1 - f_x^{\mathrm{S}}\right)\left(1 - f_y^{\mathrm{S}}\right) & f_B^{\mathrm{S}} &= \left(1 - f_x^{\mathrm{S}}\right) f_y^{\mathrm{S}} \\ f_C^{\mathrm{S}} &= f_x^{\mathrm{S}}\left(1 - f_y^{\mathrm{S}}\right) & f_D^{\mathrm{S}} &= f_x^{\mathrm{S}} f_y^{\mathrm{S}} \end{aligned} \tag{5.21}$$

with parameters $f_{x,y}^{\mathrm{S}}$ of the selected discriminating variables x and y. These can be expressed as a function $f_{(x,y)}^{\mathrm{S}}(N_i, f_i^{\mathrm{SM}})$ of the known quantities N_i and f_i^{SM}. Thus, (5.20) becomes an equation system with four remaining unknowns N^{SM}, N^{S}, f_x^{S} and f_y^{S} which can be solved.

Abbreviating f^{SM} to f, the yield of background events then reads

$$\begin{aligned} N^{\mathrm{SM}} = \tfrac{1}{2(f_A f_D - f_B f_C)} \Big\{ & f_D N_A - f_C N_B - f_B N_C + f_A N_D \\ & - \Big[\Big(- (f_C N_B) - f_D(N_A + 2N_B) + f_B N_C + f_A N_D + 2 f_B N_D \Big)^2 \\ & - 4(f_D N_B - f_B N_D)\Big((f_C + f_D)(N_A + N_B) - (f_A + f_B)(N_C + N_D) \Big) \Big]^{1/2} \Big\} \end{aligned} \tag{5.22}$$

and the number of signal events becomes

$$N^{\mathrm{S}} = N_A + N_B + N_C + N_D - N^{\mathrm{SM}}. \tag{5.23}$$

5.7.2 Determination of Event Yields

For this analysis, the variables $\not\!\!E_T$ and M_T are selected for background estimation. Figure 5.24 shows a plot of the 2D parameter space both for the full data and MC sets. The four tiles can be reasonably defined by separating the $\not\!\!E_T$-dimension at a value of 60 GeV and the M_T dimension at 130 GeV. This setting is used to compute a realistic background- and signal event yield for the complete range of data. Since the statistic

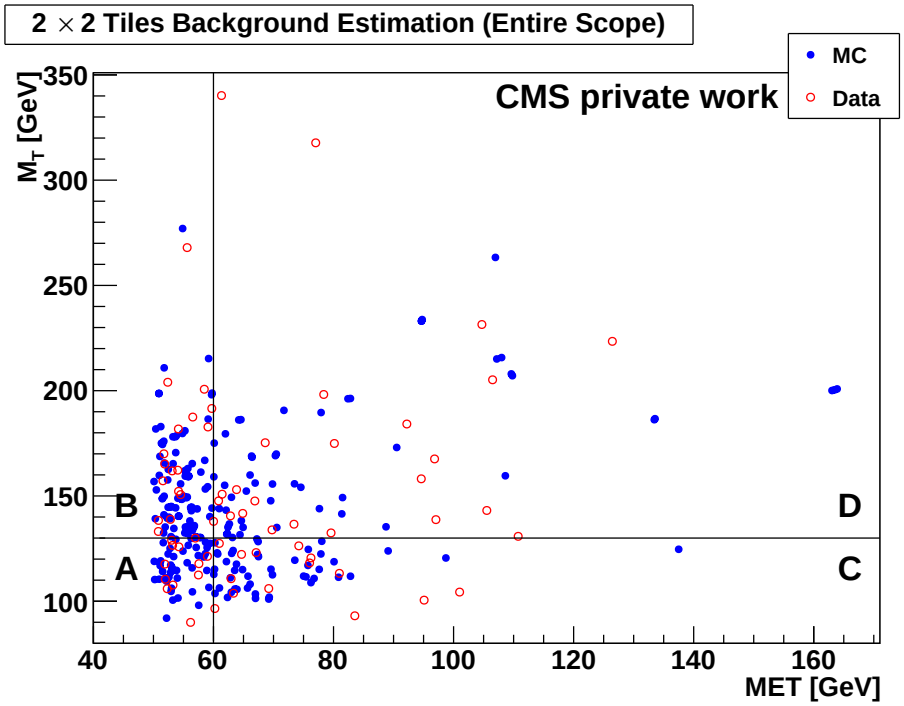

Figure 5.24: Event distribution and 'Tile' segmentation of the complete data set.

is dominated by background events in a region of low $\not\!\!E_T$ and M_T, a *control region* is defined, whose yield is not taken into account for limit calculation. Figure 5.25 shows the $\not\!\!E_T$ and M_T distributions with the chosen frontier of this region. This covers all events with

$$\not\!\!E_T < 220\,\text{GeV} \qquad \text{or} \qquad M_T < 310\,\text{GeV}. \tag{5.24}$$

The parameter space of the control region is plotted in Fig. 5.26. As expected, no significant difference to Fig. 5.24 is visible. Hence, the same segmentation as for the full dataset can be used.

Finally, the number of data events in each tile is counted and the MC fractions f_i^{SM} are determined for both the complete- and the control region. With those, the background and signal yields are computed. The yield in the *search region* is estimated by subtracting the control yield from the total one. All results are listed in Table 5.10.

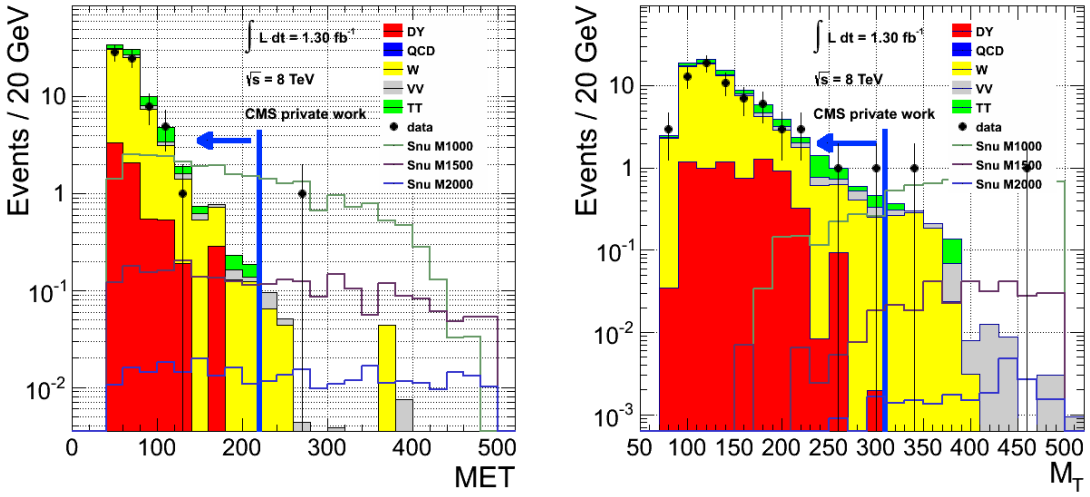

(a) (b)

Figure 5.25: Selection cuts for $\not{E}_T$ (a) and M_T (b) to define the control region.

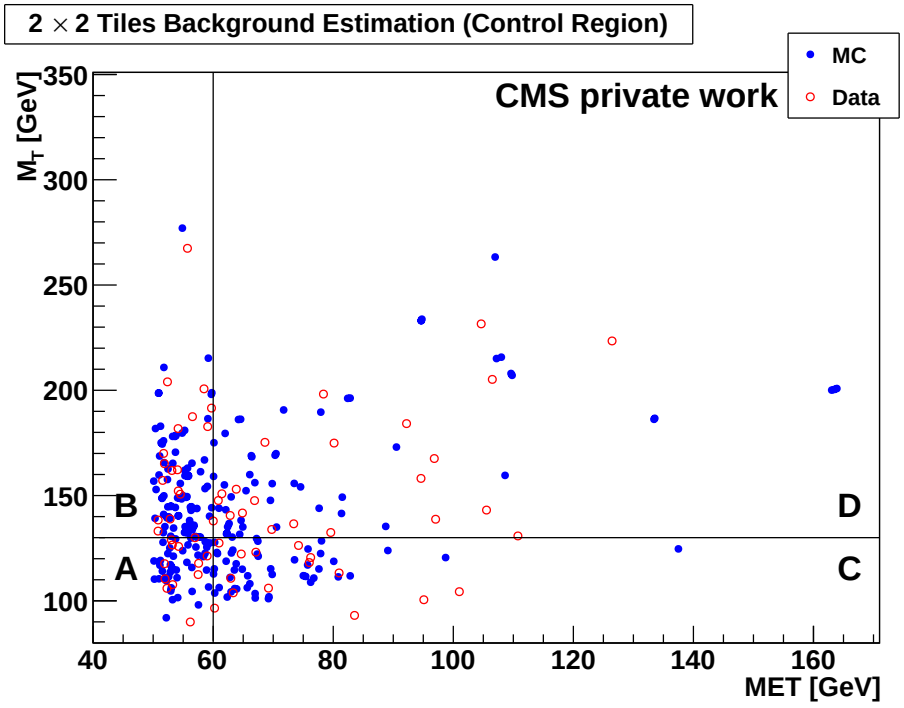

Figure 5.26: Event distribution and 'Tile' segmentation of the control region.

	Full Range	Control Region	Search Region
Data	69	67	2
BG	63.69 ± 7.98	59.73 ± 7.73	3.96 ± 1.98
Signal	0.00 ± 0.00	0.00 ± 0.00	0.00 ± 0.00
DY	4.75 ± 2.18	3.72 ± 1.93	1.03 ± 1.01
TT	18.00 ± 4.24	16.87 ± 4.11	1.13 ± 1.04
W	36.67 ± 6.06	35.35 ± 5.95	1.32 ± 1.15
WW	2.68 ± 1.64	2.37 ± 1.54	0.31 ± 0.56
WZ	1.24 ± 1.11	1.10 ± 1.05	0.14 ± 0.36
ZZ	0.35 ± 0.60	0.31 ± 0.55	0.04 ± 0.24
QCD	0.00 ± 0.00	0.00 ± 0.00	0.00 ± 0.00

Table 5.10: Results of the Tiles Background Estimation over the full range and the control region. The search region yields are the difference of both. Signal yields are practically nil within the computation accuracy. The total background yield is itemised for the different processes according to their fractions in MC.

5.8 Systematic Uncertainties

5.8.1 Parton Distribution Functions

The source of experimental data are proton-proton collisions realised by the LHC. So, the production of particles arising from interactions of proton constituents depends on the nucleon structure. This is specified by QCD and can not be calculated perturbatively but have to be modelled by *Parton Distribution Functions* (PDF) that can be determined experimentally only.

As a characteristic property of QCD, gluons underlie a self interaction. Thus, they are able to reproduce themselves in gg interactions or undergo a $q\bar{q}$ pair production, if the available energy is sufficient. Hence, the quark and gluon content of a proton depends on the scale Q^2 of energy present in the interaction and the interacting parton's momentum fraction x of the proton's momentum [60]. Now, a PDF

$$f_i(x, Q^2) \tag{5.25}$$

describes the probability to find a parton with fraction x at an energy scale Q^2 within the proton. Then the cross section for a hadronic interaction reads

$$\sigma = \sum_{i,j} \int_0^1 \int_0^1 f_i(x_1, Q^2) \cdot f_j(x_2, Q^2) \cdot \sigma_{ij}(Q^2) \cdot dx_1 dx_2 \tag{5.26}$$

with initial parton flavours i and j and a cross section for parton interaction σ_{ij} at a given centre of mass energy. The indices 1 and 2 denote the interacting partons.

Several groups determined PDFs from experimental data using different methods. Following the recommendations of the PDF4LHC Working Group [62], the PDF sets

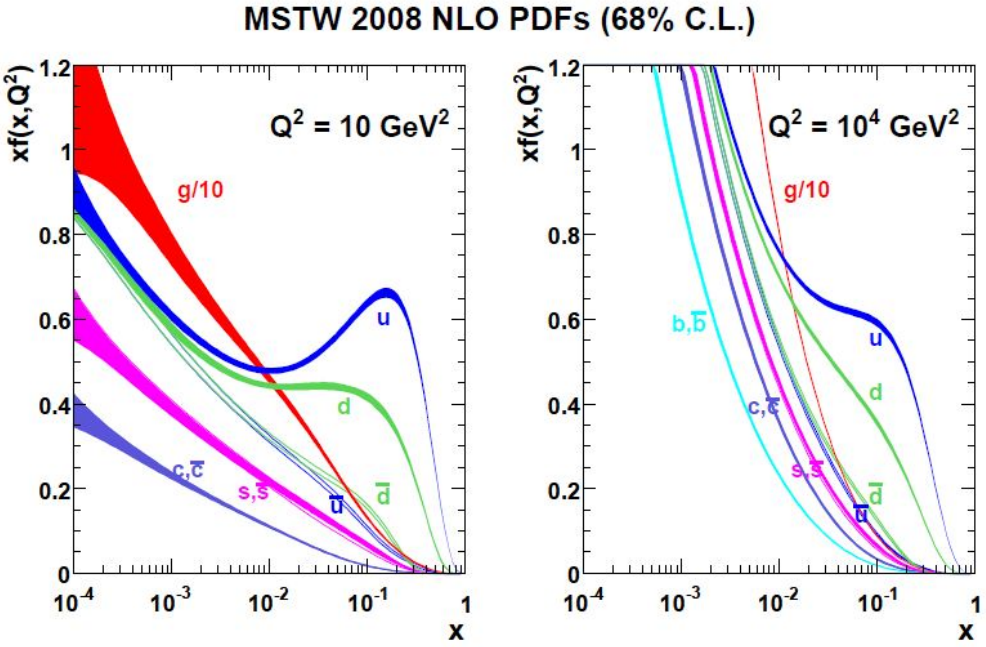

Figure 5.27: PDFs for several partons obtained from data by the MSTW group. The bands represent the 1σ confidence intervals of the performed fit. Taken from [61].

CTEQ10 [63], MSTW2008 [61] and NNPDF2.1 [64] are used to calculate uncertainties for the Monte Carlo samples. The latter ones are generated using the 'Pythia Z2 Tune', which includes the CTEQ6L PDFs [65]. All of the mentioned sets use both electro- and hadroproduction from fixed target- and collider experiments, covering data from deep inelastic scattering (DIS), W/Z and jet production. The PDFs are finally retrieved from a global fit to the data. Fig. 5.27 shows the result for the MSTW2008 PDF set.

The determination of uncertainties is performed by fitting the investigated datasets to new PDFs. This procedure varies according to the group [66]. CTEQ10 and MSTW2008 use a *Hessian* approach. This method is based on the minimisation of a a suitable log-likelihood function

$$\chi^2 = \frac{1}{N_{\text{dat}}} \sum_{i,j} \Delta d_i \, \text{cov}_{ij} \, \Delta d_j \tag{5.27}$$

with number of datapoints N_{dat}, the difference Δd_i between theoretical description and data and the covariance matrix cov_{ij}, whose exact definition differs from group to group. Finally, the uncertainties are derived from the Hessian matrix of 2nd derivatives of χ^2. Every free parameter of the fit is represented by an eigenvector of the Hessian matrix. Consider a variable X with value X_0 for the central PDF set. Applying the uncertainty related to eigenvector i yields a value X_i^+ for a PDF corresponding for correction parallel to i and a value X_i^- for the antiparallel case. Then, the total uncertainty for N data

points becomes

$$\begin{aligned}\Delta X^{+}_{\max} &= \sqrt{\sum_{i=1}^{N}\left[\max\left(X_i^{+}-X_0, X_i^{-}-X_0, 0\right)\right]^2} \\ \Delta X^{-}_{\max} &= \sqrt{\sum_{i=1}^{N}\left[\max\left(X_0-X_i^{+}, X_0-X_i^{-}, 0\right)\right]^2}\end{aligned} \tag{5.28}$$

For CTEQ10, an additional correction factor $1/C_{90}$ with $C_{90} = 1.64485$ has to be applied to recalibrate the uncertainty from 90% C.L. to the commonly used value of 68%.

The method used by NNPDF is based on the *Monte Carlo* technique. A set of N replicas is generated and PDF dependent observables are formulated as functional $\mathcal{F}[\{q\}]$ with a particular PDF replica q [66]. The expectation value for this quantity is

$$\langle \mathcal{F}[\{q\}]\rangle = \frac{1}{N}\sum_{i=1}^{N}\mathcal{F}[\{q^{(i)}\}] \tag{5.29}$$

and the uncertainty becomes

$$\sigma_{\mathcal{F}} = \sqrt{\frac{1}{N-1}\sum_{i=1}^{N}\left(\mathcal{F}[\{q^{(i)}\}] - \langle \mathcal{F}[\{q\}]\rangle\right)^2}. \tag{5.30}$$

In practical implementation, the effect of PDF uncertainties on the final event yield is determined. In preparation, the evaluated datasets have to be reconfigured to match a certain PDF. For this purpose a set of reweighting factors is available to scale the set from the original CTEQ6.6 to the desired one. The LHAPDF [67] group provides a wide variety of PDF sets, including reweighting factors, in common data formats. For CTEQ10, $N = 53$ and for MSTW2008 $N = 41$ subsets with varied parametrisations are available. The NNPDF2.1 set contains several subsets with 100 replicas each.

An additional source of uncertainty is the value of the strong coupling α_s. The PDF sets use fixed reference values which are $\alpha_s(m_Z) = 0.118$ (CTEQ), 0.120 (MSTW) and 0.119 (NNPDF) with a 1σ uncertainty $\Delta\alpha_s = 0.0012$. To calculate the impact of different values of α_s on the event yield, errors with constant PDF and varying α_s and vice versa are estimated. For the Hessian methods the combined uncertainty for an observable X can be approximated by adding the single ones in quadrature:

$$\Delta X = \sqrt{\Delta X^2_{\mathrm{PDF}} + \Delta X^2_{\alpha_s}} \tag{5.31}$$

The NNPDF2.1 set is based on replicas, whose numbers have to be chosen sufficiently to grant the desired accuracy [66]. Considering a α_s gaussianly distributed around a central value $\alpha_s^0 = 0.119$, the number of replicas is

$$N_{\mathrm{rep}}^{\alpha_s^{(j)}} \sim \exp\left(-\frac{\left(\alpha_s^{(j)}-\alpha_s^0\right)^2}{2\left(\Delta\alpha_s\right)^2}\right). \tag{5.32}$$

	CTEQ10			MSTW2008			NNPDF2.1	
	PDF	α_s	combined	PDF	α_s	combined	full	random
DY	+(1.124)	+(0.070)	+(1.126)	+(0.791)	+(0.140)	+(0.803)	0.994	0.965
	−(1.350)	−(−0.074)	−(1.352)	−(0.649)	−(−0.125)	−(0.661)		
TT	+(5.093)	+(−0.078)	+(5.093)	+(2.950)	+(0.064)	+(2.951)	4.046	4.035
	−(4.676)	−(0.184)	−(4.679)	−(3.463)	−(−0.067)	−(3.463)		
W	+(0.841)	+(−0.145)	+(0.853)	+(0.818)	+(−0.101)	+(0.825)	0.732	0.735
	−(0.778)	−(0.128)	−(0.788)	−(0.636)	−(0.111)	−(0.646)		

Table 5.11: Result of the estimation of PDF and α_s uncertainties in % of the final event yield for the main background samples DY, TT and W. NNPDF is fitted both with a full set of 700 replicas and a random selection of 300 ones.

Now, with

$$\langle \mathcal{F} \rangle_{\text{rep}} = \frac{1}{N_{\text{rep}}} \sum_{j=1}^{N_\alpha} \sum_{k_j=1}^{N_{\text{rep}}^{\alpha_s^{(j)}}} \mathcal{F}\left(PDF(k_j, j), a_s^{(j)}\right) \tag{5.33}$$

with replica k_j obtained using $\alpha_s^{(j)}$, equation (5.30) transforms to

$$\sigma_{\text{combined}}^{\text{NNPDF}} = \sqrt{\frac{1}{N_{\text{rep}} - 1} \sum_{j=1}^{N_\alpha} \sum_{k_j=1}^{N_{\text{rep}}^{\alpha_s^{(j)}}} \left(\mathcal{F}\left(PDF(k_j, j), a_s^{(j)}\right) - \mathcal{F}_0\right)}. \tag{5.34}$$

This is the description of a gaussian standard deviation, averaged over all replica fits.

For the dominating background samples DY, TT and W, a calculation for PDF uncertainties is performed. The results are summarised in Table 5.11. The value used for limit calculation is the combined one with the highest magnitude.

5.8.2 Jet Energy Correction

The measurement of the correct jet energy is an essential requirement to allow reliable event- and particle reconstruction. As the calorimeter response is not linear to a particle's energy and the measurement underlies technical limitations like sensitivity of electronic devices to several influences, a non-linear correction of the jet energy is necessary.

A first, systematic effect is given by a mismatch between data and simulation. This one can be reduced by Jet Energy Scaling (see section 5.3.2). Further corrections are provided by the JEC group [68]. These include algorithms to remove energy coming from pile-up events (termed 'L1'), *relative* (L2) corrections to flatten the response against η and *absolute* (L3) corrections to minimise the p_T dependence.

Nevertheless, an irreducible uncertainty on the jet energy reconstruction remains. This is measured by the JEC group and provided as data file. The uncertainties are applied to the jet p_T both increasing and decreasing the central value with respect to the jet's η and p_T. Afterwards, the new $\not{E}_T$ is reconstructed and the final effect on the event yield is observed.

5.8.3 Other Uncertainties

Several additional uncertainties affect the total background event yield as they influence the MC scaling (5.18). In detail these are

- Cross section
  The cross section errors for many standard model processes have been calculated by the generator group [69]. The error is applied on the cross section used for MC generation.

- Pileup reweighting
  The in-time pileup distribution, *i.e.* the number of vertices per bunch crossing, is calculated from measured pileup luminosities under the assumption that the total inelastic cross section is 69.3 mb [70]. This value is varied by $\pm 5\%$ and the resulting distributions are used for reweighting.

To quantise the effect on the event yield, these gross errors are applied at the scaling of every single background data set. The events in M_T and S_T distributions are counted and averaged. Table 5.12 shows the results.

Beyond that, there are further uncertainties to be taken into account, which enter the event yield in a one-to-one scale. These are given by the appropriate POGs [71].

- Luminosity: 4.4%
- τ ID efficiency: 6%
- τ energy scale: 3%
- e energy scale: 1%

The impact of e ID efficiency for HEEP electrons is considered as negligible.

Type	Dataset	Yield	AVG (±)	AVG (tot)
XSEC	DY	M_T : +5.4%; −5.4% S_T : +5.4%; −5.4%	5.4% 5.4%	5.4%
	TT	M_T : +6.1%; −6.1% S_T : +6.1%; −6.1%	6.1% 6.1%	6.1%
	W	M_T : +5.0%; −5.0% S_T : +5.0%; −5.0%	5.0% 5.0%	5.0%
	WW	M_T : +3.4%; −3.4% S_T : +3.4%; −3.4%	3.4% 3.4%	3.4%
	WZ	M_T : +3.8%; −3.8% S_T : +3.8%; −3.8%	3.8% 3.8%	3.8%
	ZZ	M_T : +2.5%; −2.5% S_T : +2.5%; −2.5%	2.5% 2.5%	2.5%
JEC	DY	M_T : +13.7%; −23.7% S_T : +12.6%; −22.1%	18.7% 17.3%	18.0%
	TT	M_T : +1.7%; −3.7% S_T : +2.4%; −3.4%	2.7% 2.9%	2.8%
	W	M_T : +10.9%; −9.8% S_T : +10.3%; −9.1%	10.4% 9.7%	10.0%
	WW	M_T : +2.3%; −0.2% S_T : +1.9%; −0.2%	1.2% 1.1%	1.1%
	WZ	M_T : +3.4%; −4.4% S_T : +2.3%; −4.0%	3.9% 3.2%	3.5%
	ZZ	M_T : +3.8%; −3.0% S_T : +3.6%; −2.7%	3.4% 3.1%	3.3%
PU	DY	M_T : +6.3%; −4.7% S_T : +5.6%; −4.1%	5.5% 4.8%	5.2%
	TT	M_T : +1.1%; −1.3% S_T : +1.1%; −1.3%	1.2% 1.2%	1.2%
	W	M_T : +4.7%; −5.0% S_T : +4.7%; −5.0%	4.8% 4.8%	4.8%
	WW	M_T : +1.8%; −2.2% S_T : +1.8%; −2.1%	2.0% 2.0%	2.0%
	WZ	M_T : +1.5%; −2.0% S_T : +1.5%; −2.0%	1.8% 1.8%	1.8%
	ZZ	M_T : +1.3%; −1.4% S_T : +1.3%; −1.4%	1.3% 1.4%	1.4%

Table 5.12: Effects of cross section (XSEC)-, Jet Energy Correction (JEC)- and pileup reweighting (PU) uncertainties on the event yield. AVG (±) denotes the average of up- and downscale effects. AVG (tot) is the average of M_T and S_T and used for limit calculation.

6 Statistical Evaluation

No significant excesses above the standard model expectation have been found within this analysis. The background expectation and the event yield are used to determine an exclusion limit for the resonant $\tilde{\nu}_\tau$ production. First, an upper limit on the cross section as a function of the $\tilde{\nu}_\tau$-mass is calculated. After comparison with theoretical predictions, this can be interpreted as lower mass limit. Within the applied simplified model, the cross section is related to the coupling λ' via $\sigma \sim |\lambda'|^2$ [57]. So, a result for a certain coupling λ' can be scaled to any other arbitrary coupling numerically. Hence, this evaluation is confined to a single value of $\lambda' = \lambda = 0.1$. The statistical analysis is performed using a *bayesian* approach.

6.1 Bayesian Statistics

The Bayesian approach is based on the *Bayes' Theorem* describing conditional probability [72]:

$$P(B|C) = \frac{P(C|B) \cdot P(B)}{P(C)} \tag{6.1}$$

In case of a counting experiment that yields n Poisson distributed data-, s signal- and b background events, (6.1) gives the normalised *posterior probability density function*

$$p(s|n) = \frac{P(n|s)\pi(s)}{\int P(n|s')\pi(s')ds'} \tag{6.2}$$

where $\pi(s)$ is the prior density for s, and $P(n|s)$ denotes the probability of observing n at given s. Assuming a Poisson shape

$$p(s|n) = \frac{(s\epsilon)^n}{n!} \cdot \epsilon e^{-s\epsilon}, \tag{6.3}$$

with an uncertainty parameter ϵ, an upper observed limit u is given by

$$\int_0^u p(s'|n)ds' = CL, \quad 0 \leq CL \leq 1 \tag{6.4}$$

where CL is termed the Bayesian *confidence level* for the limit u.

In practical implementation, (6.3) is regarded as Poisson-Likelihood function

$$L(s|n) = \frac{(s+b)^n}{n!} \cdot e^{-(s+b)}. \tag{6.5}$$

A special characteristic of Bayesian statistics is the ability to take additional information into account, that is known *a priori*. This virtue is exploited to include systematic uncertainties of parameters into the calculation. The parameters themselves influence the s, b and n yield and need not to be treated explicitly. Every uncertainty is formulated

as a *nuisance parameter* ν, that smears the Likelihood function with an additional prior density $\pi(\nu)$. As $\pi(\nu)$ should describe the behaviour of the error of a parameter and therefore a random variable, it is modelled as a log-normal function [73]. All nuisance parameters can be taken together to a vector:

$$\pi(\vec{\nu}) = \prod_i \pi(\nu_i). \tag{6.6}$$

Now, the posterior probability has to be extended to

$$p(s|n) = \frac{\int L(s|n) \cdot \pi(s) \cdot \pi(\vec{\nu})\, d\vec{\nu}}{\iint L(s'|n) \cdot \pi(s') \cdot \pi(\vec{\nu})\, ds'\, d\vec{\nu}}. \tag{6.7}$$

An expected limit can be calculated similarly. In this case, any data is absent. Thus, the calculation has to be performed on the basis of toy samples which are diced following the posterior distribution (6.2). Also the nuisance parameters are simulated with respect to their prior functions to take an estimate of uncertainties into account. The final expected limit is provided by the median of the single limits of all toy experiments.

6.2 Limit Calculation

The limit calculation is performed with the 'Combined Limit' tool provided by the Higgs Working Group [74]. This is a front-end for the 'RooStats' package [75], which provides a huge functionality for statistical analyses.

For a confidence level (CL) of 95%, this tool computes the ratio of excluded and signal cross section

$$r = \frac{\sigma_{\text{excl}}}{\sigma_{\text{sig}}} \tag{6.8}$$

for selected mass points including statistical 68% and 95% bands.

The analysed data has been retrieved in a single bin counting experiment, where the bin is the search region defined in section 5.7. Treated mass points are 0.5, 1.0, 1.5, 2.0, 2.2, 2.4 and 2.6 TeV. The integration (6.4) to calculate the limit is done by the Markov Chain Monte Carlo method [76]. A starting point for this iterative algorithm is estimated by an initial ProfileLikelihood approximation. For the expected limit, the calculation is based on 450 simulated experiments per mass point.

All background uncertainties described in section 5.8 are taken into account. The theoretical $d\bar{d} \to \tilde{\nu}_\tau \to e\tau$ total NLO cross section has 5% uncertainty coming from QCD cross section, 5% from PDF uncertainty and 4.6% from model dependency [57]. This yields a combined uncertainty of 8.44%. Figure 6.1 shows the result of the fit. Thus, the lower $\tilde{\nu}_\tau$ mass limit is

$$(1.20 \pm 0.15)\ \text{TeV}, \quad (95\%\ \text{C.L.}) \tag{6.9}$$

Contemporary limits for $\tilde{\nu}_\tau$-masses have been set by the ATLAS Collaboration [77] recently. Figure 6.2 shows their result for a resonant $\tilde{\nu}_\tau$ with $\lambda' = 0.11, \lambda = 0.07$ and $\lambda' = 0.10, \lambda = 0.05$. The mass limits are between 1.0 TeV and 1.3 TeV. ATLAS also determined the dependence of $m(\tilde{\nu}_\tau)$ as a function of λ and λ'. As the value of λ only

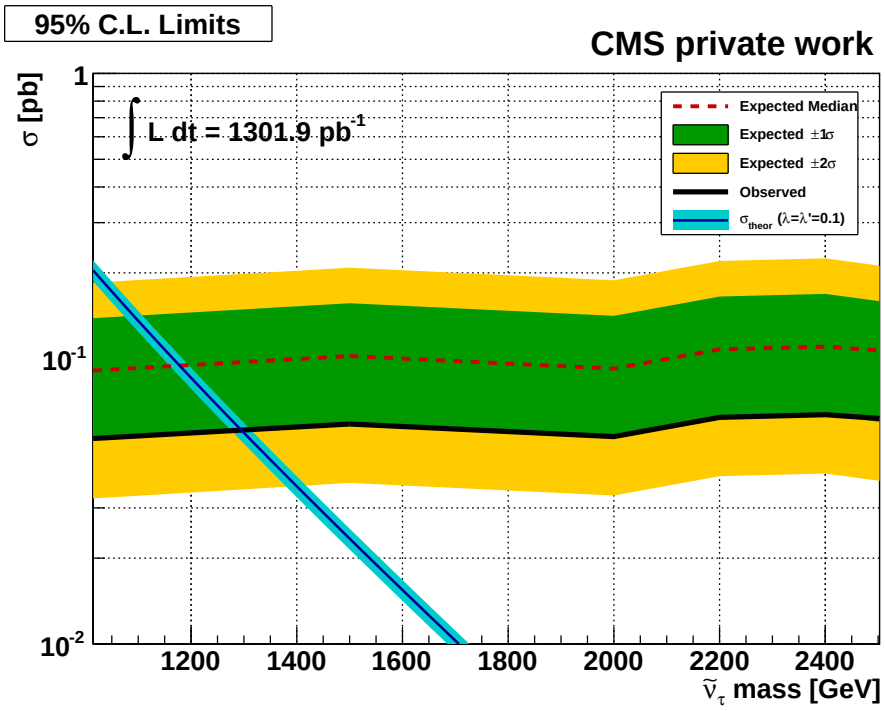

Figure 6.1: Bayesian Fit of the upper cross section limit for the process $d\bar{d} \to \tilde{\nu}_\tau \to e\tau$. Comparison with the theoretical cross section yields the lower $\tilde{\nu}_\tau$ mass limit.

affects the $\tilde{\nu}_\tau$-lifetime, the λ' value is the crucial one. For the case $\lambda = 0.07$ and $\lambda' = 0.1$, $m(\tilde{\nu}_\tau)$ is about 1.2 TeV. Finally, the results of this analysis are according with recently published results.

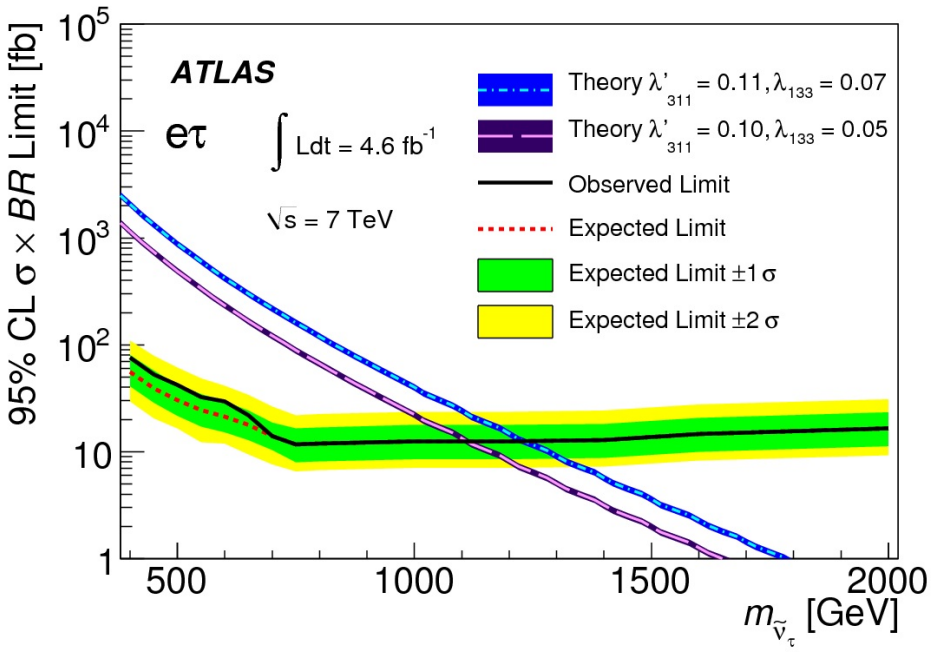

Figure 6.2: ATLAS m($\tilde{\nu}_\tau$) limits for $\lambda' = 0.11, \lambda = 0.07$ and $\lambda' = 0.10, \lambda = 0.05$. Taken from [77].

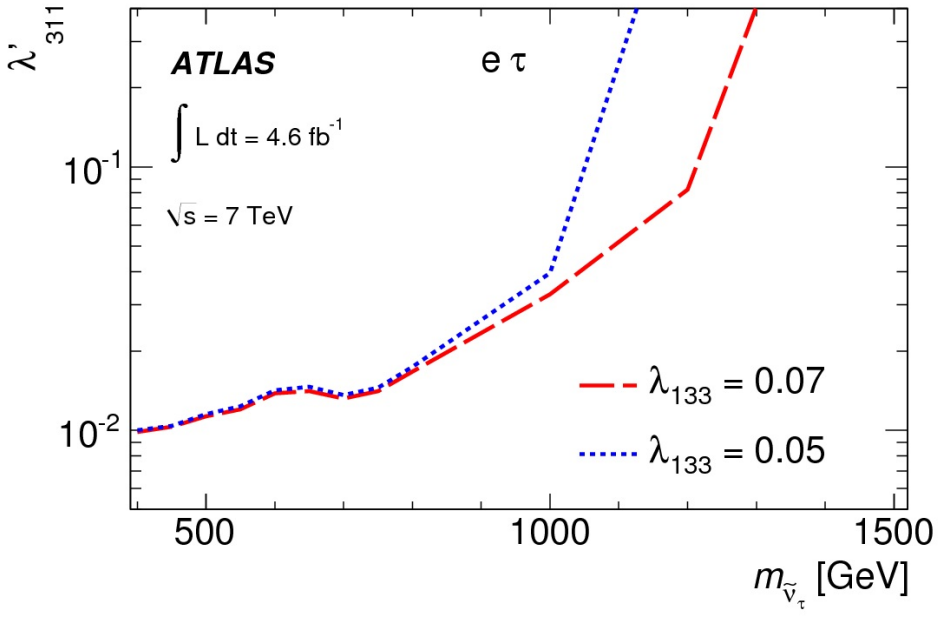

Figure 6.3: ATLAS $m_{\tilde{\nu}}(\lambda, \lambda')$ limits. Taken from [77].

7 Conclusion

A search for a τ-sneutrino in the process $d\bar{d} \to \tilde{\nu}_\tau \to e\tau$ within an RPV SUSY model has been performed. The search was based on a total amount of $15.55\,\mathrm{fb}^{-1}$ collected with the CMS experiment during the 2012 data taking period with $\sqrt{s} = 8\,\mathrm{TeV}$. Due to an unresolvable mismatch between data and MC background, only $1.302\,\mathrm{fb}^{-1}$ were taken into account for analysis.

To grant a best possible match between background and data, the k factors for scaling the cross sections from leading order (LO) to a higher one have been determined numerically. The total event yield has been determined by a data driven method and finally a lower Bayesian mass limit for the $\tilde{\nu}_\tau$ has been calculated.

Despite a rather rough match between data and Monte Carlo backgrounds based on unprecise τ reconstruction and a relatively low luminosity, the obtained results yield, together with similar results from ATLAS, the current world best limits.

Due to the large number of inaccuracies that have been faced in this analysis, doubts on the unconfined reliability of the result can't be rejected entirely.

There are many opportunities for future improvements. The biggest problem is to solve the improper background scaling issue to make the full dataset available for analysis. In addition, the progress in improvements of τ reconstruction algorithms is fast, so that high expectations in future analyses treating similar topics are justified.

Appendix

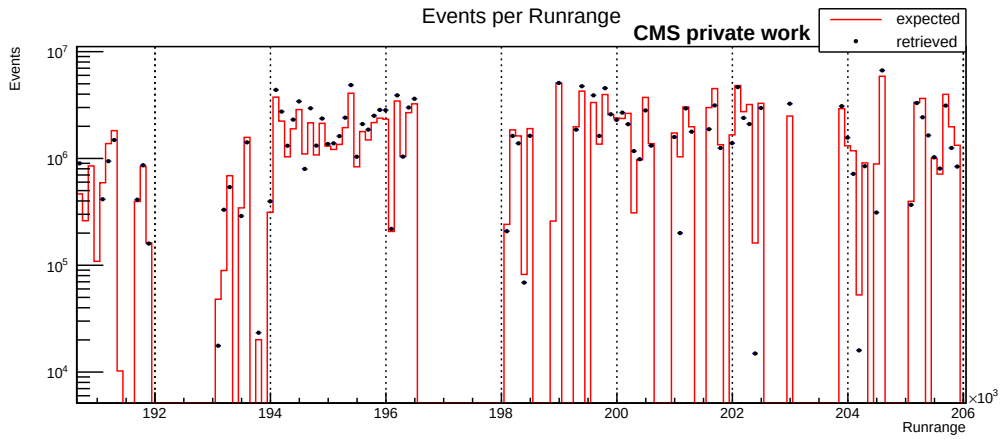

Figure A.1: Event numbers actually present in data (*retrieved*) and expected to be contained in certified runs of the SingleElectron dataset (*expected*), plotted as a function of the run. Comparison of the numbers show a surplus in retrieved events of about 8.4%. Thus, this mismatch can not confirm a suspicion, that a lack in retrieved events is responsible for the scaling issue described in section (5.2.3).

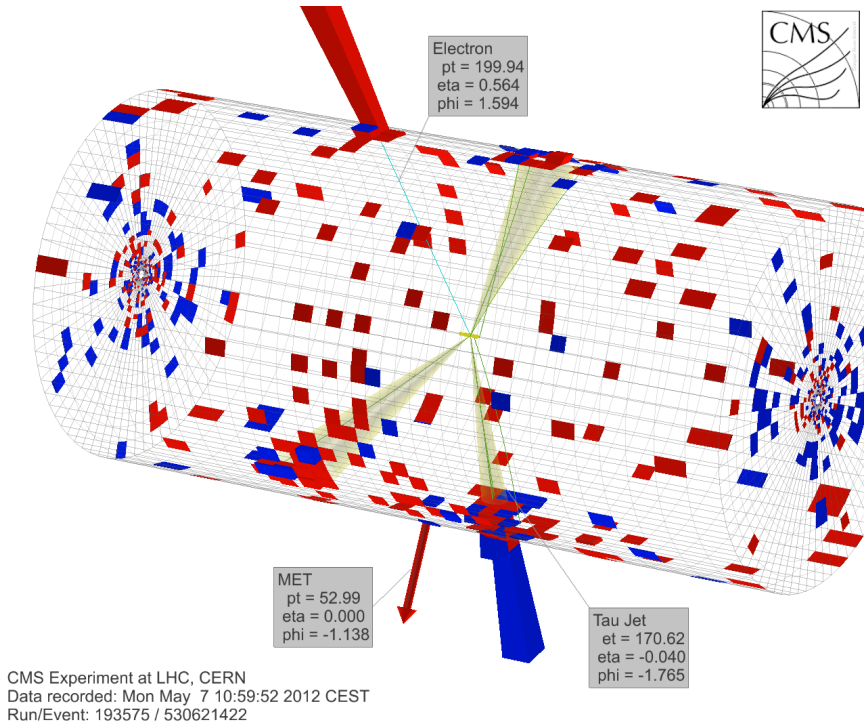

(a) 3D view

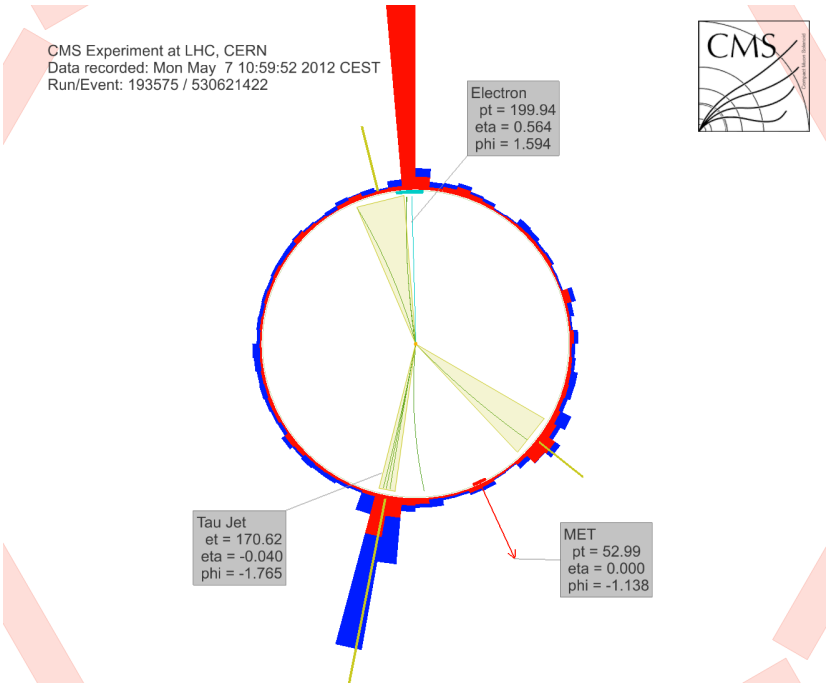

(b) ρ-ϕ plane

Figure A.2: Display of one of the two data events present in the search region (see section 5.7.2) after appliance of all event selection stages. The τ-jet can be clearly identified as 3-prong.

Bibliography

[1] Sylvia Berryman. Democritus. In *The Stanford Encyclopedia of Philosophy*. 2010.

[2] John Dalton. *A New System of Chemical Philosophy*. Dawson, 1808.

[3] Károly Simonyi. *Kulturgeschichte der Physik: Von den Anfängen bis heute*. Harri Deutsch Verlag, third edition, 2001.

[4] Donald H. Perkins. *Introduction to Particle Physics*. Addison-Wesley, third edition, 1987.

[5] D. Griffiths. *Introduction to Elementary Particles*. Wiley, 2008.

[6] J. Beringer et al. Review of Particle Physics. *Phys. Rev. D*, 86:010001, Jul 2012.

[7] CMS Collaboration. Observation of a new boson at a mass of 125 GeV with the CMS experiment at the LHC. *Phys. Lett. B*, 716:30–61, 2012. arXiv:hep-ex/1207.7235.

[8] ATLAS Collaboration. Observation of a new particle in the search for the Standard Model Higgs boson with the ATLAS detector at the LHC. *Phys. Lett. B*, 716:1–29, 2012. arXiv:hep-ex/1207.7214.

[9] A. N. Schellekens. Quantum Field Theory. In *Lectures of the Graduate School of Particle Physics*, 1997.

[10] W. Buchmüller and C. Lüdeling. Field Theory and Standard Model. In *Lectures given at the European School of High-Energy Physics*, 2005. arXiv:hep-ph/0609174v1.

[11] A. Pich. Quantum Chromodynamics. *Lectures at the 1994 European School of High-Energy Physics*, 1995. arXiv:hep-ph/9505231v1.

[12] Christoph Berger. *Elementarteilchenphysik*. Springer, 2002.

[13] A. Djouadi. The Anatomy of electro-weak symmetry breaking. I: The Higgs boson in the standard model. *Phys.Rept.*, 457:1–216, 2008. arXiv:hep-ph/0503172.

[14] Rupert Millard. `https://commons.wikimedia.org/wiki/File:Mexican_hat_potential_polar_with_details.svg`. Accessed Dec 2012.

[15] D.I. Kazakov. Beyond the Standard Model: In Search of Supersymmetry. *Lectures at the 2000 European School of High-Energy Physics*, 2001. arXiv:hep-ph/0012288.

[16] Stephen P. Martin. A Supersymmetry Primer, 1997. arXiv:hep-ph/9709356.

[17] Martin J. White. SUSY and Dark Matter Constraints from the LHC. *Int.J.Mod. Phys.*, A22:5771–5784, 2007. arXiv:hep-ph/0605065.

[18] Lars Bergström. Dark Matter Candidates. *New J. Phys.*, 11:105006, 2009. arXiv:hep-ph/0903.4849.

[19] B.C. Allanach, A. Dedes, and H.K. Dreiner. R parity violating minimal supergravity model. *Phys. Rev. D*, 69:115002, 2004. arXiv:hep-ph/0309196.

[20] V. D. Barger, W. Y. Keung, and R.J.N. Phillips. Possible sneutrino pair signatures with R-parity breaking. *Phys. Lett. B.*, 364:27–32, 1995. arXiv:hep-ph/9507426.

[21] Herbi K. Dreiner, Marja Hanussek, and Jong-Soo Kim. Neutrino masses and mixings in the baryon triality constrained minimal supersymmetric standard model. *Phys. Rev. D*, 84:113005, 2011. arXiv:hep-ph/1106.4338.

[22] Lyndon Evans (ed.) and Philip Bryant (ed.). LHC Machine. *JINST*, 3:S08001, 2008.

[23] ATLAS Collaboration. The ATLAS Experiment at the CERN Large Hadron Collider. *JINST*, 3(08):S08003, 2008.

[24] CMS Collaboration. The CMS experiment at the CERN LHC. *JINST*, 3(08): S08004, 2008.

[25] ALICE Collaboration. The ALICE experiment at the CERN LHC. *JINST*, 3(08): S08002, 2008.

[26] LHCb Collaboration. The LHCb Detector at the LHC. *JINST*, 3(08):S08005, 2008.

[27] Christiane Lefèvre. `http://cds.cern.ch/record/1260465`. Accessed Jan 2013.

[28] CMS Collaboration. CMS Luminosity - Public Results, Accessed Jan 2013. `https://twiki.cern.ch/twiki/bin/view/CMSPublic/LumiPublicResults#2012_Proton_Proton_Collisions`.

[29] Stéphanie Moreau. `http://ireswww.in2p3.fr/ires/recherche/cms/stephanie/CMSdetectE.html`. Accessed Jan 2013.

[30] G. Baiatian et al. Design, Performance, and Calibration of CMS Hadron-Barrel Calorimeter Wedges. Technical Report CMS-NOTE-2006-138, CERN, 2007.

[31] J. Knobloch, L. Robertson, et al. *LHC computing Grid: Technical Design Report. Version 1.06*. Technical Design Report LCG. CERN, Jun 2005.

[32] CMS Collaboration. Technical proposal for CMS computing. Technical Report CERN-LHCC-96-045, CERN, 1996.

[33] R. Brun and F. Rademakers. ROOT: An object oriented data analysis framework. *Nucl. Instrum. Meth.*, A389:81–86, 1997.

[34] Herbi K. Dreiner and Sebastian Grab. All Possible Lightest Supersymmetric Particles in R-Parity Violating mSUGRA. *Phys. Lett. B*, 679:45–50, 2009. arXiv:hep-ph/0811.0200.

[35] W. Adam, R Frühwirth, A. Strandlie, and T. Todorov. Reconstruction of Electrons with the Gaussian-Sum Filter in the CMS Tracker at the LHC. Technical Report CMS-NOTE-2005-001, CERN, 2005.

[36] CMS Collaboration. Particle-Flow Event Reconstruction in CMS and Performance for Jets, Taus, and MET, 2009. CMS-PAS-PFT-09-001.

[37] M. Cacciari, G. P. Salam, and G. Soyez. The Anti-k_t jet clustering algorithm. *JHEP*, 0804:063, 2008. arXiv:hep-ph/0802.1189.

[38] CMS Collaboration. Performance of tau-lepton reconstruction and identification in CMS. *JINST*, 7:1001, 2012. arXiv:physics.ins-det/1109.6034.

[39] Michael Brodski. MUSiC - Model Unspecific Search in CMS with τ Leptons. Master's thesis, RWTH Aachen, 2012.

[40] G. Corcella, I.G. Knowles, et al. HERWIG 6: An Event generator for hadron emission reactions with interfering gluons (including supersymmetric processes). *JHEP*, 0101:010, 2001. arXiv:hep-ph/0011363.

[41] T. Sjostrand, S. Mrenna, and P. Z. Skands. PYTHIA 6.4 Physics and Manual. *JHEP*, 0605:026, 2006. arXiv:hep-ph/0603175.

[42] S. Agostinelli et al. Geant4 – a simulation toolkit. *NIMPR*, A(506):250–303, 2003.

[43] J. Alwall, M. Herquet, F. Maltoni, O. Mattelaer, and T. Stelzer. MadGraph 5 : Going Beyond. *JHEP*, 1106:128, 2011. arXiv:hep-ph/1106.0522.

[44] CMS Collaboration. The official CMS Luminosity Calculation, Jan 2013. `https://twiki.cern.ch/twiki/bin/view/CMS/LumiCalc`.

[45] CMS Collaboration. Inclusive W/Z cross section at 8 TeV, 2012. CMS-PAS-SMP-12-011.

[46] CMS Collaboration. Jet Energy Corrections determination at 7 TeV, 2010. CMS-PAS-JME-10-010.

[47] CMS Collaboration. Characterization and treatment of anomalous signals in the CMS Electromagnetic Calorimeter, 2011. CMS-AN-10-357.

[48] T. Boccali, R. Frühwirth, W. Waltenberger, et al. Vertex reconstruction framework and its implementation for CMS, 2003. arXiv:physics.data-an/0306014.

[49] CMS Collaboration. HEEP Electron ID and isolation, Feb 2013. `https://twiki.cern.ch/twiki/bin/view/CMS/HEEPElectronID`.

[50] CMS Collaboration. TauID: recommendation from the Tau POG, Sep 2012. `https://twiki.cern.ch/twiki/bin/view/CMS/TauIDRecommendation`.

[51] CMS Collaboration. Jet Identification, Sep 2012. `https://twiki.cern.ch/twiki/bin/viewauth/CMS/JetID`.

[52] M. Bondarenko et al. High Energy Physics Model Database – HEPMDB: Towards decoding of the underlying theory at the LHC. In *Les Houches 2011: Physics at TeV Colliders New Physics Working Group Report*, 2012. arXiv:hep-ph/1203.1488.

[53] B.C. Allanach. SOFTSUSY: a program for calculating supersymmetric spectra. *Comput. Phys. Commun.*, 143:305–331, 2002. arXiv:hep-ph/0104145.

[54] A. Pukhov et al. CompHEP: A Package for evaluation of Feynman diagrams and integration over multiparticle phase space, 1999. arXiv:hep-ph/9908288.

[55] J. Alwall et al. A Standard format for Les Houches event files. *Comput. Phys. Commun.*, 176:300–304, 2007. arXiv:hep-ph/0609017.

[56] Jan Kalinowski. R-parity violating signals at existing colliders, 1998. arXiv:hep-ph/9807312.

[57] H.K. Dreiner, S. Grab, M. Krämer, and M.K. Trenkel. Supersymmetric NLO QCD corrections to resonant slepton production and signals at the Tevatron and the CERN LHC. *Phys. Rev. D*, 75:035003, 2007. arXiv:hep-ph/0611195.

[58] CMS Collaboration. Standard Model Cross Sections for CMS at 8 TeV, Oct 2012. `https://twiki.cern.ch/twiki/bin/view/CMS/StandardModelCrossSectionsat8TeV`.

[59] ATLAS Collaboration. Background Estimation for Inclusive SUSY Searches - The Tiles Method, May 2009. ATL-PHYS-PUB-2009-077.

[60] Alan D. Martin. Proton structure, Partons, QCD, DGLAP and beyond. *Acta Phys. Polon.*, B39:2025–2062, 2008. arXiv:hep-ph/0802.0161.

[61] A.D. Martin, W.J. Stirling, R.S. Thorne, and G. Watt. Parton distributions for the LHC. *Eur. Phys. J. C*, 63:189–285, 2009. arXiv:hep-ph/0901.0002.

[62] M. Botje, J. Butterworth, A. Cooper-Sarkar, A. de Roeck, J. Feltesse, et al. The PDF4LHC Working Group Interim Recommendations, 2011. arXiv:hep-ph/1101.0538.

[63] H. L. Lai, M. Guzzi, J. Huston, Z. Li, P. Nadolsky, et al. New parton distributions for collider physics. *Phys. Rev. D*, 82:074024, 2010. arXiv:hep-ph/1007.2241.

[64] Francesco Cerutti. The NNPDF2.1 Parton Set, 2011. arXiv:hep-ph/1107.1095.

[65] Rick Field. Min-Bias and the Underlying Event at the LHC. *Acta Phys. Polon. B*, 42:2631–2656, 2011. arXiv:hep-ph/1110.5530.

[66] S. Alekhin, . Alioli, R. Ball, V. Bertone, J. Blumlein, et al. The PDF4LHC Working Group Interim Report, 2011. arXiv:hep-ph/1101.0536.

[67] LHAPDF: The Les Houches Accord PDF Interface, Jan 2013. `https://lhapdf.hepforge.org`.

[68] CMS Collaboration. Introduction to Jet Energy Corrections at CMS, Jan 2013. `https://twiki.cern.ch/twiki/bin/viewauth/CMS/IntroToJEC`.

[69] CMS Collaboration. Standard Model Cross Sections for CMS at 7 TeV, Feb 2013. `https://twiki.cern.ch/twiki/bin/view/CMS/StandardModelCrossSections`.

[70] CMS Collaboration. Utilities for Accessing Pileup Information for Data, Feb 2013. `https://twiki.cern.ch/twiki/bin/view/CMS/PileupJSONFileforData`.

[71] CMS Collaboration. CMS 2011 Approved Object Criteria & Properties, Feb 2013. https://twiki.cern.ch/twiki/bin/view/CMS/Internal/ApprovedObjects.

[72] J. Heinrich et al. Interval estimation in the presence of nuisance parameters. 1. Bayesian approach, 2004. arXiv:physics/0409129.

[73] Bob Cousins. Probability Density Functions for Positive Nuisance Parameters, 2010.

[74] CMS Collaboration. Documentation of the RooStats-based statistics tools for Higgs PAG, Feb 2013. https://twiki.cern.ch/twiki/bin/view/CMS/SWGuideHiggsAnalysisCombinedLimit.

[75] Grégory Schott, for the RooStats Team. RooStats for Searches, 2012. arXiv: physics.data-an/1203.1547.

[76] M. Jerrum and A. Sinclair. The Markov Chain Monte Carlo Method: An Approach To Approximate Counting And Integration. In PWS, editor, *Approximation Algorithms for NP-Hard Problems*, pages 482–520, 1996.

[77] Georges Aad et al. Search for a heavy narrow resonance decaying to $e\mu$, $e\tau$, or $\mu\tau$ with the ATLAS detector in $\sqrt{s} = 7$ TeV pp collisions at the LHC, 2012. arXiv:hep-ex/1212.1272.

Danksagung

Abschließend möchte ich mich bei allen bedanken, die mir die Erstellung dieser Arbeit ermöglichten.

Mein erster Dank gilt Prof. Thomas Hebbeker, der mir ermöglichte, diese Arbeit in seinem Institut anzufertigen. Das vergangene Jahr war eine spannende und erkenntnisreiche Zeit, in der ich an einem interessanten Thema arbeiten und Zeuge einer bedeutenden Epoche der Teilchenphysik werden durfte.

Ich danke Prof. Lutz Feld, dass er sich bereit erklärt hat, die Aufgabe des Zweitgutachters zu übernehmen.

Ein weiterer Dank gilt allen Institutsangehörigen, die zu einer angenehmen und anregenden Arbeitsatmosphäre beigetragen haben. Erwähnen möchte ich vor allem Metin Ata, der entscheidend an der Findung des Themas beteiligt war, Martin Weber, der mir als Betreuer beistand und Andreas Güth, der die Signalproduktion übernahm. Meinen Büronachbarn Matthias Endres, Klaas Padeken und Sebastian Thüer verdanke ich viele wertvolle Hinweise für die praktische Arbeit und die kompetente Antwort auf eine Vielzahl „dummer“ Fragen.

Ein spezieller Dank gilt den guten Geistern, die mich während meines Studiums immer wieder ermutigt haben und vor allem meiner Familie, die unerschütterlich zu mir stand. Besonders gedenke ich all derer, die die Fertigstellung dieser Arbeit nicht mehr miterleben durften.

Selbständigkeitserklärung

Hiermit erkläre ich, dass ich diese Arbeit selbständig verfasst und keine anderen als die angegebenen Quellen und Hilfsmittel verwendet, sowie Zitate kenntlich gemacht habe.

Aachen, den 1. März 2013

(Stefan Bruch)